國 立 交 通 大 學
機械工程學系
碩士論文

並聯矩陣型風力發電風車效率之實驗

The Experimental Study of Power Efficiency of Two-bladed Savonius Wind Rotors in Parallel Matrix System

研究生： 黃天洋

指導教授： 陳俊勳 教授

中 華 民 國 一 〇 一 年 六 月

並聯矩陣整合型風力發電風車效率之實驗

The Experimental Study of Power Efficiency of Two-bladed Wind Rotors in Parallel Matrix System

研究生　：黃天洋　　Student ：Tien-Yang Huang

指導教授：陳俊勳　　Advisor ：Chiun-Hsun Chen

國立交通大學

機械工程學系

碩士論文

A Thesis

Submitted to Department of Mechanical Engineering

College of Engineering

National Chiao Tung University

In Partial Fulfillment of the Requirements

For the Degree of

Master of Science

In Mechanical Engineering

June 2012

Hsinchu, Taiwan, Republic of China

中華民國一〇一年六月

The Experimental Study of Power Efficiency of Two-bladed Savonius Wind Rotors in Parallel Matrix System

並聯矩陣型風力發電風車效率之實驗

學 生：黃 天 洋　　指 導 教 授：陳 俊 勳

國立交通大學機械工程學系

摘要

本研究建立一個四顆風車矩陣並聯之二葉式沙柏扭式風車系統，將其安裝在一個開放環境中用以發電，並使用流體力學套裝軟體 Fluent 進行分析。本研究內容可分為兩大部分：其一為擋板對該系統之影響，而另一主題為電路二次測電池之加入對系統之研究。實驗中，在不同風速、風向與風車轉速的情況下，觀測周速比與其功率係數（C_p）和發電量的關係。最後，將所獲得之實驗結果與數值模擬進行比較分析。

由數值模擬結果顯示，擋板的加入有助於效率的提升。其中，無擋板之系統最大 C_p 值為 0.262，發生在周速比 0.8 的情況下；而有擋板之系統最大 C_p 值則為 0.270，亦發生在周速比 0.8 時，相差 1.03 倍。然而，兩系統最大差異發生周速比 0.6 時，相差 1.16 倍。由 C_p 值對周速比圖可知，擋板在低周速比時較能發揮其效果；當在高周速比情況下其效果不顯著。

另一方面，由實驗結果顯示，在開放環境的風速、風向與風車轉速變化極大，故藉由反覆量測以得到 C_p 與周速比之關係。實驗結果與模擬相同，擋板確實有助於效率的提升。此外，實驗顯示，電池於電路二次測的脫離，

並無助於效率提升，卻造成電壓之不穩定。在未來展望中將提升風車發電效率，並連接予市電作更有效的利用。

關鍵字：Savonius 風車、並聯矩陣系統、功率係數

The Experimental Study of Power Efficiency of Two-bladed Savonius Wind Rotors in Parallel Matrix System

並聯矩陣型風力發電風車效率之實驗

Student: Tien-Yang Huang Advisor: Prof. Chiun-Hsun Chen

Institute of Mechanical Engineering

National Chiao Tung University

ABSTRACT

This study establishes a four two-bladed Savonius wind rotors system in parallel matrix which is installed at an open field, to generate electric power. Moreover, It employs a computational fluid dynamics (CFD) software, Fluent, to analyze the flow fields and system performance. It can be separated into two sections: effect of curtain and effect of battery. The experiments detect various wind velocity, wind direction and rotational speed of wind rotors to observe the relationship between tip-speed ratio (TSR) and power coefficient (C_p). Finally, compare and analyze the results between experiment and numerical simulation.

For the numerical simulate results, the maximum C_p value of system without curtain is 0.262 at TSR 0.8; the system with curtain is 0.270 at TSR 0.8 which is 1.03 times higher than system without curtain. However, the maximal difference is happened at TSR 0.6 which is 1.16 times higher than system without curtain. From C_p to TSR diagram know that the effect of curtain especially enhance performance at low TSR.

On the other hand, the experimental results show that the wind velocity, wind direction and rotational speed of wind rotors have large fluctuation in open field. Therefore, we receive the relationship between C_p and TSR by repeating measuring. Same as the simulation results, curtain indeed improve the

performance of system. Otherwise, the experiment of withdrawing battery at second side of circuit shows that battery is no help for progress system performance (C_p) but cause voltage oscillation. Look into the future; improve the power generated efficiency of wind rotor system and connect system to local grid to have more benefit utilize.

Keywords: Savonius wind rotor; parallel matrix system; C_p (power coefficient)

ACKNOWLEDGEMENTS

這篇論文的完成第一要感謝我的指導教授　陳俊勳老師，在老師嚴嚴的教誨下，在對於敘述一件事物的邏輯上，有許多的開導；使得今天能完成這樣的作品。此外，特別要感謝曾錦鍊學長，在每一次的實驗中，有諸多的討論；實驗如何進行與現象如何解釋。有時也會告誡我一些在工作中應有的態度，真可說是亦師亦友。

當然不可忘的是師門中的諸位，我的戰友們，凌宇、詠翔、鈺鈞；不論是一同修課或是一同吃飯，寶貝這兩年我們一同走過的經歷，這些都歷歷在目。還有學長們，家維、宗翰、昶安以及已畢業的嘉軒、瑭原，在研究中所遇到的問題你們總是不吝指教,也不會在我們面前擺出學長的架子，讓人覺得十分親近。也記得在實驗室中的學弟妹，子博、秉楷、羿彣，我們還一起修課呢！你們讀書要加油，做實驗要認真，明年換你們享受豐收的結果。還有雖然與這實驗無關，卻常被我抓去當苦力的弟兄們，沒辦法將你們的名字一一列上，但實驗的順利進行，你們真是幕後推手。

最後，鄭重地感謝我的家人，雖然不常在家，但你們總是最默默支持我的一群，我愛你們。未來還有許多的路要走，大學一路上來，並在研究所這兩年的經歷與學習，實在立定了我人生未來道路的基礎。

CONTENTS

LIST OF TABLES

LIST OF FIGURES

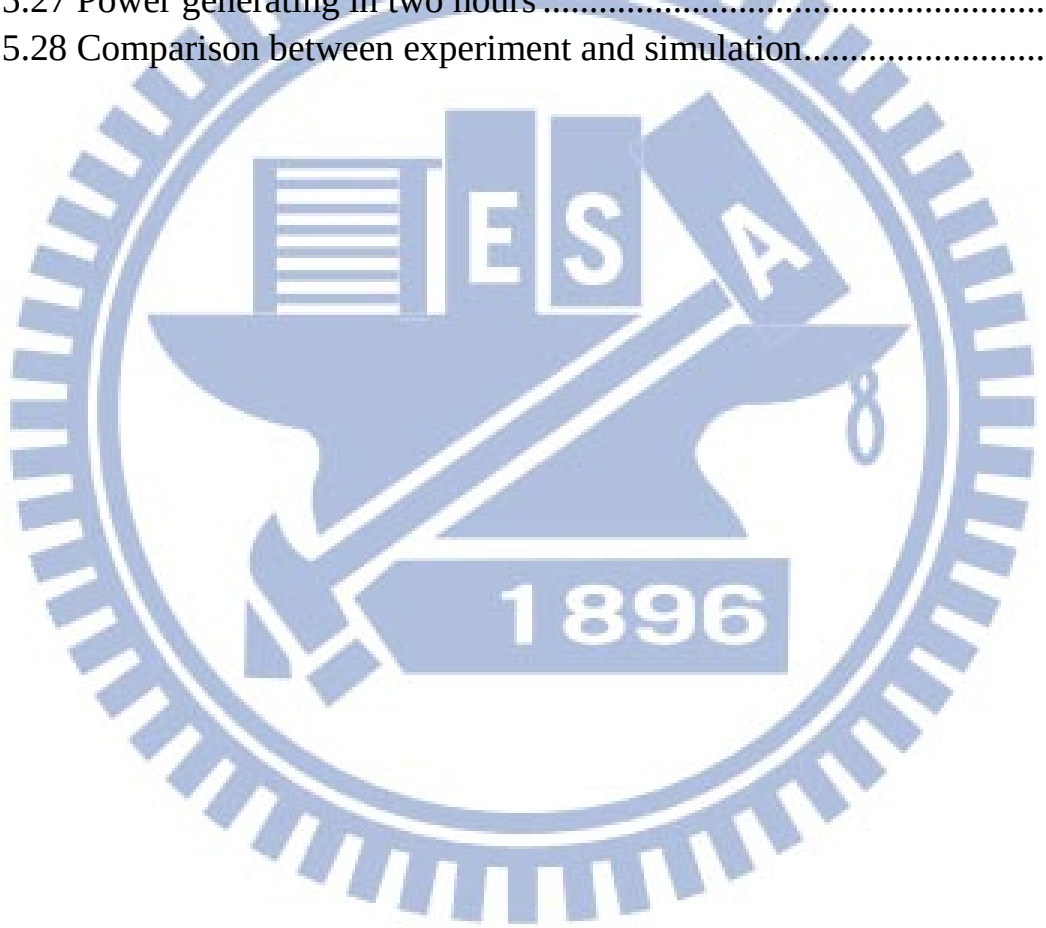

CHAPTER 1

INTRODUCTION

1.1 Motivation

The global warming, majorly caused by the emission of green house gas (GHG) (see **Fig. 1.1**), makes climate change no longer an issue appeared in literature but truly happening in our real life. Therefore, various countries are devoted their efforts on using the renewable energy resources to mitigate the climate changing problem.

Intergovernmental Panel on Climate Change (IPCC) released The Special Report on Renewable Energy Sources and Climate Change [1], in 2011. It mentioned that consumption of fossil fuels accounts for the majority of global anthropogenic GHG emission, and recommended the six most important renewable energy technologies, such as bioenergy, direct solar energy, geothermal energy, hydropower, ocean energy, wind energy, to conquer the problem of global warming. As Hondo [2] presents in his study (see **Fig. 1.2**), the GHG emission from fossil fuels is significantly greater than GHG emission from nuclear or renewable energies. Although nuclear energy has very low carbon dioxide emission, its waste impact leads to the more severe environmental problem than that of GHG emission. On the other hand, wind power is one of these six most important renewable energy technologies and it has low carbon dioxide emission during services.

Wind turbines converts the kinetic energy of the air flow into power that can be classified into horizontal axis wind turbines (HAWTs) and vertical axis wind turbines (VAWTs) as shown in **Fig. 1.3**. If the rotation axis is parallel to the horizon, then it is called HAWT. On the other hand, if the axis is perpendicular to

the horizon, then it is called VAWT. It is commonly known that the wind power generation of HAWT is higher than that of VAWT, indicated by the power coefficient (C_p). However, the former cannot be applicable to many situations. First, the high tip-speed ratio (TSR) generates the low-frequency sound to make noise pollution. Second, because of wake effect (see **Fig. 1.4**), long enough distance between wind rotors is necessary in order to avoid getting interference, leading to lower energy. Third, wind rotor has to be aligned with the wind direction to obtain a better efficiency, but it usually takes a long duration adjust its direction. Last, the cost to install and maintain a HAWT is considerable. Consequently, HAWTs is not proper to install in suburbs due to no economical benefits. On the other hand, VAWT is more appropriate to install in the suburbs with low wind speed area. It can be further classified into two categories according to their blades, namely, the lift-type such as Darrieus wind rotor, and the drag-type, like Savonius wind rotor. Although the lift-type wind rotor has higher C_p than drag-type, but the low starting torque is its disadvantage. For power generating in suburbs, the wind rotor needs to have ability to withstand the fluctuation of wind and operate quietly. The Savonius wind rotor can fulfill with all these requests, yet the power efficiency still leaves a large room for improvement.

In order to enhance the performance of Savonius wind rotor, an idea is brought up to put a series of Savonius wind rotors in a line with a fixed distance between each other and they rotate with a specific phase angle. In Feng's preliminary study [3], it shows 3-D simulation by parallel matrix system, consisting three two-bladed Savonius wind rotors (see **Fig. 1.5**) rotating with phase angle at 90° deference, has a higher performance. The maximal C_p is about 1.45 times of that by a single Savonius wind rotor. The performance is resulted

from positive interaction between Savonius wind rotors, and the flow fluctuation plays the major role in this effect (see **Fig. 1.6**). To verify this simulation, the present work carries out an experimental study on power efficiency of four two-bladed Savonius wind rotor system in parallel matrix.

1.2 Literature Review

In the book, SUICHOKUJIKU FUSHA (Vertical-axis windmill) by Seki et al. [4], the C_p of lift-type wind rotor is higher than that drag-type wind rotor. However the advantage of drag-type wind rotor has a large starting torque, making it able to generate electric power in low speed wind with big oscillation.

The Savonius rotor is a drag-type vertical axis wind rotor, developed by S. J. Savonius [5]. Its shape is like the character “S”, so it also called S-rotor. This kind of rotor is operated by drag force. The drag force difference between concave and convex surfaces drives the rotor, leading to a large starting torque, but the rotational speed is relatively low. Since the Savonius’ development, many improving researches are bringing up.

The work to improve C_p can go back to Blackwell et al. [6], which investigated the performances between fifteen configurations of Savonius wind rotor by testing in a low speed wind tunnel. The parameters investigated included the number of blades, wind velocity, height of wind rotor and blade overlap ratio. The results showed that the two-bladed configurations have better performance than the three-bladed ones, except the starting torque. Besides, the performance increases with aspect ratio slightly, and the optimum overlap ratio is between 0.1 and 0.15. Fujisawa [7] experimentally studied the performances of two-bladed Savonius wind rotors with different overlap ratios from 0 to 0.5. The results reveal

that the performance of Savonius wind rotor reaches a maximum value at an overlap ratio of 0.15. It is due to the fact that the flow through the overlap strengthens the forward movement. However, when the overlap ratio becomes larger, the recirculation zone grows accordingly, causing the performance deterioration.

Some other methods without changing geometry have also notable effect. Irabu and Roy [8] introduced a guide-box tunnel, which also can prevent the damage from strong wind disaster. The guide-box tunnel is a rectangular box with wind passage and the wind rotor is inside the box. It can adjust the inlet mass flow rate by its variable area ratio between the inlet and the outlet passage. The experimental results showed that the maximum C_p of the two-bladed wind rotor using the guide-box tunnel is about 1.23 times of that the wind rotor without the guide-box tunnel and 1.5 times of that using a three-bladed wind rotor. Apparently, it verified that the two-bladed wind rotor is better than the three-bladed one for converting wind power. Similar to the idea of guide-box tunnel, Altan et al. [9], arranged the two curtains to improve the performance of tow-bladed Savonius wind rotor. They placed two wind-deflecting plates in front of the wind rotor to prevent the opposite torque to the wind rotor rotation. The experimental results showed that C_p increase about 38% with an optimum curtain arrangement and it is 16% much higher than that without curtaining.

Shigetomi et al. [10] explored the interactive flow field around two Savonius wind rotors by experimental investigation using particle image velocimeter. They found that there exist the power improvement interactions between two rotating Savonius rotors in the appropriate arrangements. The interactions are caused by the Magnus effect to provide the additional rotation of the downstream rotor and the periodic coupling of local flow between two wind rotors. However, they are

quite sensitive between two wind rotors to the wind direction so that wind rotors arranged together will lose one of the VAWTs inherent advantages, such as no influence of wind direction.

In recent years, the prosperity of the computer makes the simulation studies becoming popular. Zhao et al. [11] applied the computational fluid dynamics (CFD) software to investigate the performance of new helical Savonius wind rotors. They analyzed the behaviors of the wind rotors with different aspects ratio, number of blades, overlap distance and helical angle. The results showed that three-blade helical wind rotor has lower C_p than two-bladed one, and the best overlap ratio, aspect ratio, and helical angle are 0.3, 6.0 and 180°, respectively. Antheaume et al. [12] applied the CFD software, Fluent, to investigate the performance of vertical axis Darrieus wind rotor in different working fluids by using k-ε turbulent model under steady-state conditions. They also discussed the average efficiency of several wind rotors connected in parallel pattern. The results showed that increasing the wind rotors' number or decreasing the distance between wind rotors can make the efficiency higher, due to the velocity streamlines straightening effect by the configuration. Pope et al. [13] applied Fluent to investigate the performances of zephyr VAWT and compared the predictions with experimental data. By the reason that a free spinning turbine cannot be fully simulated, they used constant rotational speeds of the VAWT in simulations and changed the specification of parameters to reveal freely moving turbine blades in experiments. They indicated that measuring the performance at constant rotational speed is valuable since any power generation connected to the electricity grid needs to operate at constant speed. Howell et al. [14] applied Fluent to investigate the performances of one VAWT in 2-D and 3-D simulations and compared the predicted results with measurements. The turbulence model

used RNG k-ε model, by which the applicability in flow field involves large flow separations. The error bars on experimental data were within ±20% of measured values. The results showed that the performances predicted by 2-D simulations are apparently higher than those by 3-D simulations and experimental measurements due to the effect of the generation of over tip vortices. Hu and Tong [15] used Fluent to analyze the performances of VAWT with windshield for decreasing the counter torque. They used k-ε RNG turbulent model and SIMPLE algorithm in 2-D simulations. The results showed that about 15° of inclination angle between the bottom of windshield and x-axis gives the highest value of torque.

Base on the aforementioned studies on power improvement interaction, Feng [3] applied the CFD software, Fluent, to investigate the flow field around two-bladed Savonius wind rotors and their corresponding performances. The study mentioned that the parallel matrix system has the maximum C_p value, which is 1.45 times of that by using the single Savonius wind rotor in 3-D simulation. It indicates that the parallel matrix arrangement of wind rotors can improve the power efficiency.

In wind power generating system, electric circuit also play an important role. In the book, Wind Energy Systems for Electric Power Generation by Stiebler [16], gives the theories for the conversion of wind energy to electric power and the classification of power generation methods.

1.3 Scope of Present Study

The purpose of this study is to establish a stand-along wind power generating system in parallel matrix of four two-bladed Savonius wind rotors, and then to generate the electricity that can be connected to grid. The scope of present study is illustrated in **Fig. 1.7**. A parallel matrix system is established to extract wind energy to transformation as mechanical energy. The generator converting mechanical energy is set up to generate electrical energy. The automatic control and monitor system is used to deal with the electric power generated. Since the setup of curtains will enhance the wind power passing through the rotors, the experimental study can be separated in two parts: one is without curtaining and the other with curtaining. In each experiment, the TSR is adjusted to get the optimum generating power by measuring the wind velocity and wind direction under different loadings. After that, the data are collected from power generation to calculate the power efficiency of parallel matrix system. A series of the corresponding numerical simulations are carried out as well. The predicted results are compared with the related measurements.

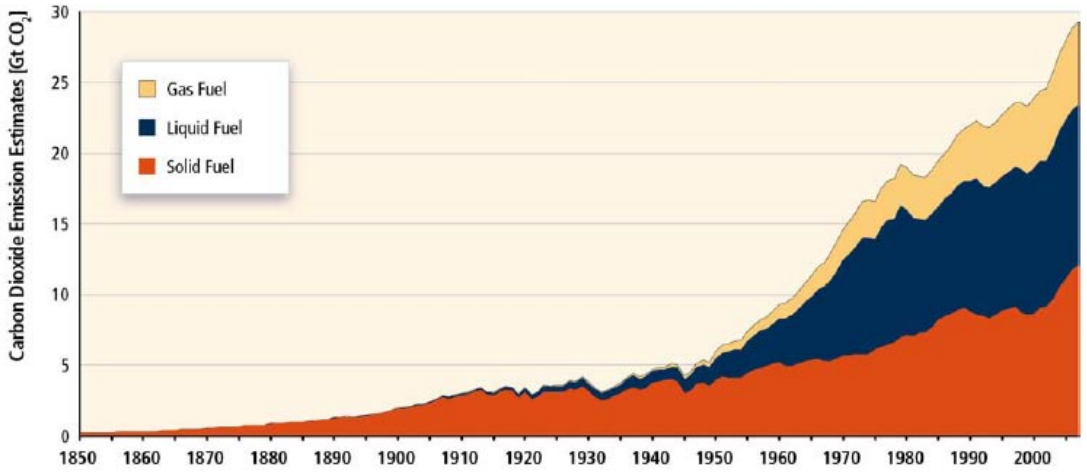

Fig. 1.1 Global CO_2 emissions from fossil fuel burning, 1850 to 2007. Gas fuel includes flaring of natural gas. All emission estimates are expressed in Gt CO_2 (Boden and Marland, 2010) [18]

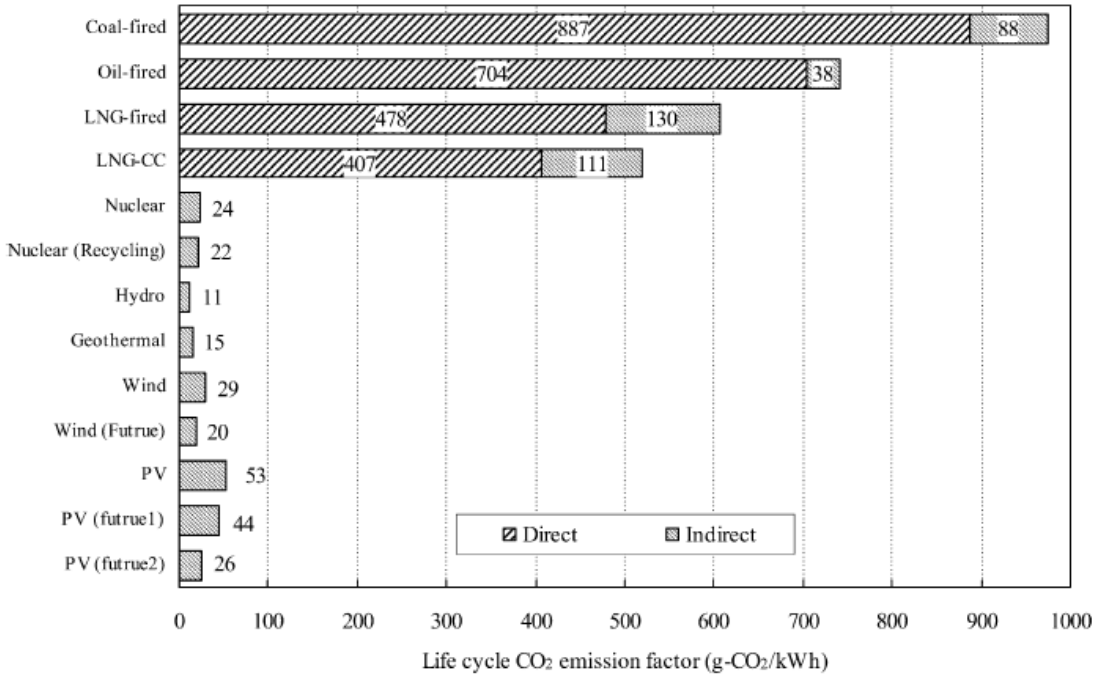

Fig. 1.2 Life cycle CO_2 emission factors for different types of power generation systems [2]

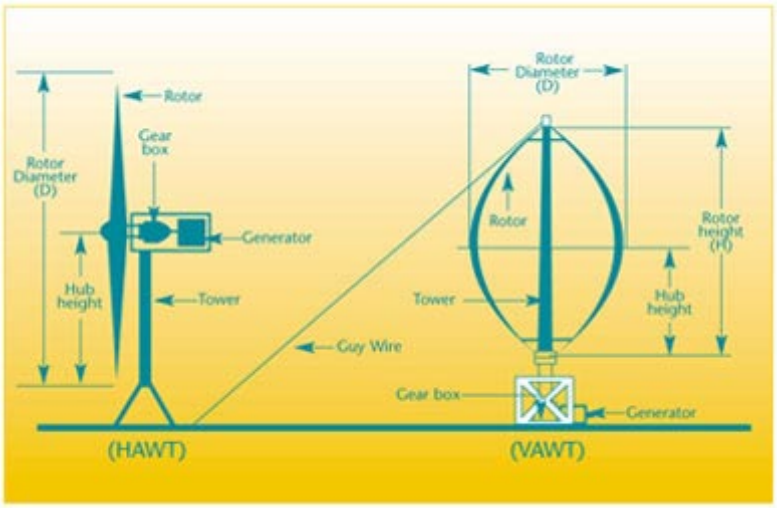

Fig. 1.3 Structures of wind turbine [19]

Fig. 1.4 Wake effect from wind turbine picture (Riso National Laboratory, Denmark) [20]

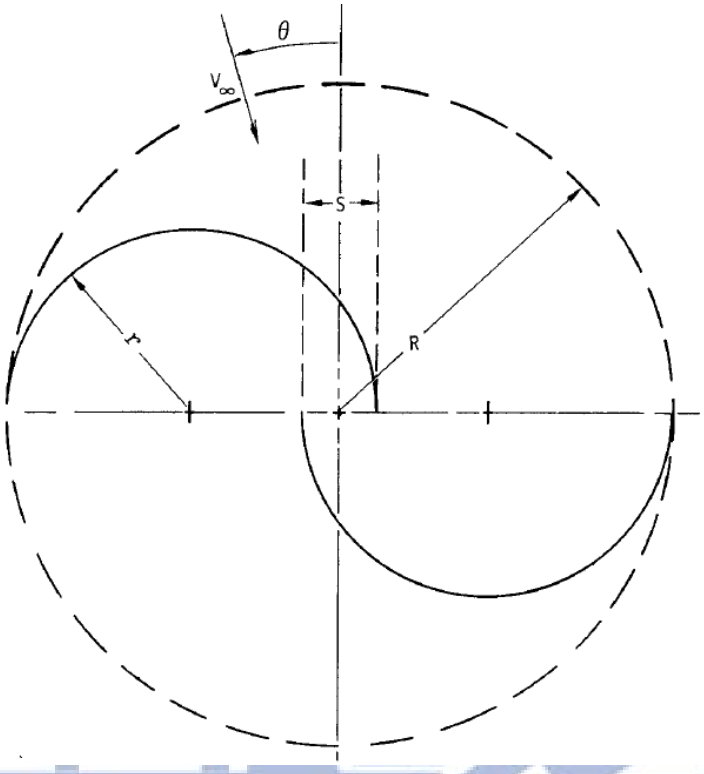

Fig. 1.5 Schematic of a two-bladed Savonius wind rotor [6]

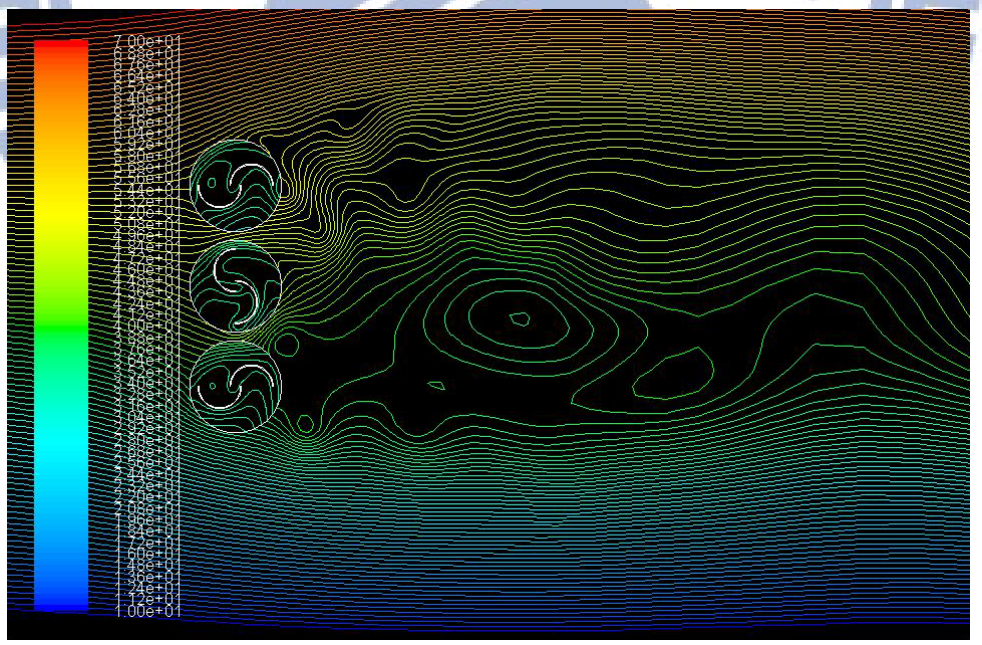

Fig. 1.6 Streamlines around three Savonius wind rotors with phase angle 90° difference. [3]

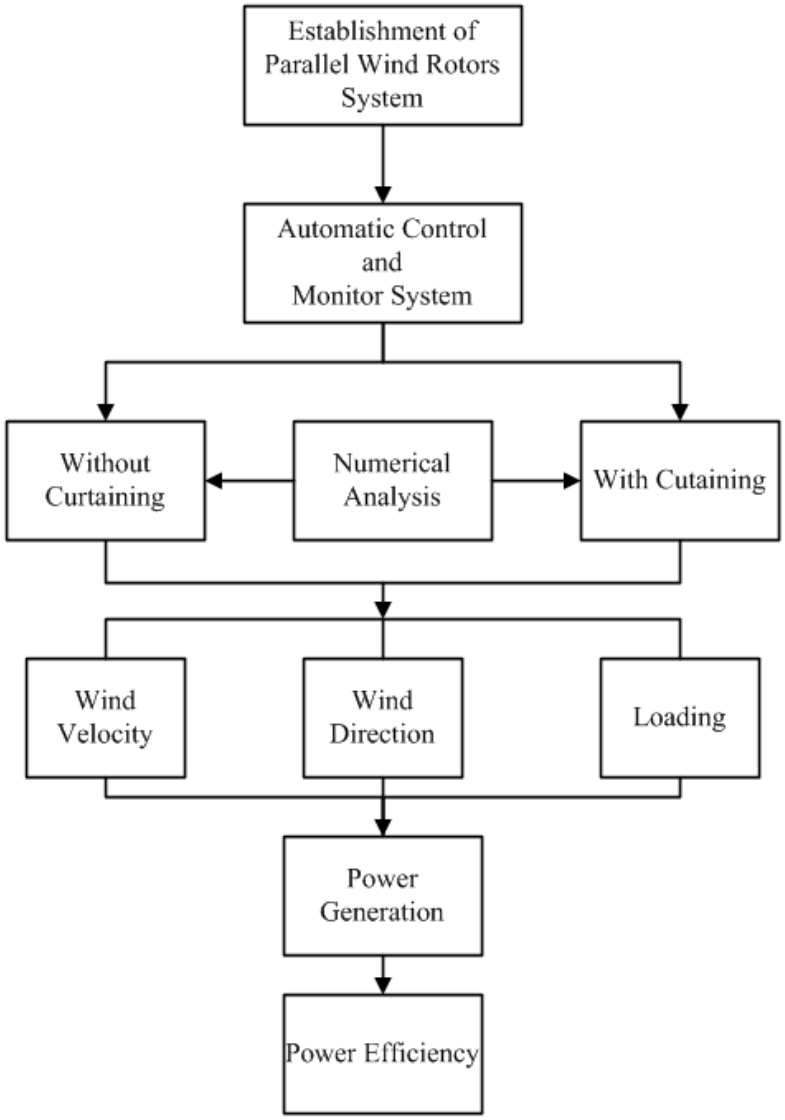

Fig. 1.7 The scope of this study

CHAPTER 2

FUNDAMENTALS OF WIND ENERGY

2.1 Brief History of Wind Energy

The wind energy has been used for thousands of years such as sailing, grinding grains, irrigation and drawing water. The first windmill appeared in Europe can be traced back to the twelfth century. After many years developing, the Netherlands used windmill to drain wetlands from the fourteenth century onwards and become an economy developed country gradually. Professor James Blyth built an experiment of windmill to produce electricity in Scotland in July 1887. The windmill, built and used by Charles Brush in Ohio, U.S.A. in 1888, was the first one used for producing electricity.

Because the first wind power station was established in Denmark in 1891, wind power became an important part of a decentralized electrification in the first quarter of the twentieth century. In Australia, small wind generators were used to provide power at isolated post offices and farms. By 1930, windmill had been widely manufactured and used to generate electricity for the distribution system having not yet been installed in America. Following these experience, American manufacturers started build and sell small wind turbines not only for battery-charging but also for interconnection to electricity networks. The first megawatt wind turbine was built in USA in 1941. In the 1970s and 1980s, the U.S. government promoted the technologies for the large-scale commercial wind turbines. NASA researched many of the turbine designs under this project that still is used today.

In the end of 2002, there was roughly 32 GW of power supplied from wind energy in the world. Europe has been the leader in wind power utilization,

contributing 76% of the total. In 2006, roughly 65 GW of power were installed in wind farms worldwide, in which more than 47 GW located in Europe, and more than 11 GW in the United States.

2.2 Basic of Wind Energy Conversion

2.2.1 Power Conversion and Power Coefficient

The wind energy of the flowing air passing through an area A with velocity v_1 is:

$$P_W = \frac{\rho}{2} A v_1^3 \tag{2-1}$$

where ρ is air density, depending on air pressure and moisture. It may be assumed $\rho \approx 1.225$ kg/m^3 for practical calculations.

If the airflow pass through the wind turbine in axial direction that the swept area is A, The useful mechanical power obtainment is expressed by means of the power coefficient C_p:

$$P = C_p \frac{\rho}{2} A v_1^3 \tag{2-2}$$

Supposing the wind velocity of airflow is homogeneous, the value before the wind turbine is v_1. After passing through the retardation of wind turbine, the speed value which is well behind the wind turbine, reduce to v_3. Due to the power conversion, wind velocity v_1 reduce to a velocity v_3, as shown in **Fig. 2.1**, a simplified theory could be claimed that the velocity can be represented in an average value v_2, where $v_2 = (v_1+v_3)/2$, in the retardation where the moving blades located. On this basis, Betz in 1920 has shown by a simple calculation that the maximum useful power can be obtained for $v_3/v_1 = 1/3$; where the power coefficient $C_p = 16/27 \approx 0.593$. On account of profile loss, tip loss and wake rotation loss, wind turbine displays the maximum values $C_{p,\,max}$ within 0.4 ~ 0.5

in reality. In order to determine the mechanical power available for the load machine, such as electrical generator or pump, Eq. (2-2) has to take an efficiency of the drive train, taking losses in bearings, couplings and gear boxes into account.

An important parameter of wind rotor is the tip-speed ratio (TSR), λ. It is defined as a ratio of the circumferential velocity of blade tips to the wind speed:

$$\lambda = {u}/{v_1} = \frac{D}{2} \cdot \frac{\omega}{v_1} \tag{2-3}$$

where D is the outer turbine diameter and ω is the angular wind rotor speed.

Considering that in the rotating mechanical system, the power is the product of torque T and angular speed ω ($P = T \cdot \omega$), then C_p becomes

$$C_p = \frac{P}{P_W} = \frac{T \cdot \omega}{\frac{1}{2}\rho A v_1^3} \tag{2-4}$$

Fig. 2.2 shows typical characteristics C_p (λ) for different types of wind rotor, includes the constant maximum value according to Betz, as well as the figure indicates a revised curve C_p by Schmitz, who takes the downstream deviation from axial air flow direction into account. The difference is notable in the region of lower TSRs.

2.2.2 Wind Rotor Blades Using Aerodynamic Drag or Lift

Extract the airflow power to mechanical power without considering design of wind rotor blades, Betz [17] showed the momentum theory with the corresponding physical based ideal limit value. However, the wind power generation unit cannot be without wind rotor blades in real conditions. The fundamental difference for various rotor blade designs depends on what kind aerodynamic force is utilized to produce the mechanical power. As the wind rotor blades are subjected to airflow, the generated aerodynamic drag is parallel

to the flow direction, whereas the lift is perpendicular to flow direction. The real power coefficients obtained are greatly dependent on whether aerodynamic drag or aerodynamic lift is used.

2.2.2.1 Drag Devices

The simplest type of wind energy conversion can be achieved by means of pure drag surfaces as shown in **Fig. 2.3**. The air impinges on the surface *A* with wind velocity *v*, and then the drag *D* can be calculated from the air density ρ, the surface area *A*, the wind velocity *u* and the aerodynamic drag coefficient C_D as

$$D = C_D \frac{1}{2} \rho A w^2 = C_D \frac{1}{2} \rho A (v-u)^2 \quad (2\text{-}5)$$

The relative velocity, $w = v–u$, which effectively impinges on the drag area, is determined by wind velocity *v*. The resultant power is

$$P = D \cdot u = \frac{1}{2} \rho A v^3 \left[C_D \left(1 - \frac{u}{v}\right)^2 \frac{u}{v} \right] = \frac{1}{2} \rho A v^3 C_p \quad (2\text{-}6)$$

Resemblance to which is described in **Chapter 2.2.1**, it can be shown that C_p reaches a maximum value with a velocity ratio of $u/v = 1/3$. The maximum value of C_p is then

$$C_{p,max} = \frac{4}{27} C_D \quad (2\text{-}8)$$

If considerate that the aerodynamic drag coefficient of a concave surface curved against the wind direction can hardly exceed a value of 1.3. Thus, the maximum power coefficient of a general drag-type wind rotor becomes about 0.2, only one third of Betz's ideal C_p value of 0.593.

2.2.2.2 Lift Devices

Utilization of aerodynamic lift on wind rotor blade can achieve power coefficients much higher. The lift blade design employs the same principle that enables airplanes to fly. As shown in **Fig. 2.4**, when air flows over the blade, a pressure gradient creates between the upper and the lower blade surfaces. The pressure at the lower surface is greater than upper surface. Thus, the difference of pressure produces a lift force to uplift the blade. The lift force occurred on a body by wind can be calculated from the air density ρ, acting area A, wind velocity v and aerodynamic lift coefficient C_L as

$$L = C_L \frac{1}{2} \rho A v^2 \tag{2-9}$$

When blades are attached to the central axis of a wind rotor, the lift force is translated into rotational motion. All of the modern wind rotor types are designed for utilizing this effect, and the best type of these kinds of wind rotor is suited with a horizontal rotational axis. The creation of aerodynamic force can be divided into a component in the direction of free-stream velocity, the drag force D, and a component perpendicular to the free-stream velocity, the lift force L. The lift force L can be further divided into a component L_{torque} in the plane of rotation of the wind rotor, and a component L_{thrust} perpendicular to the plane of rotation. L_{torque} constitutes the driving torque of the wind rotor.

Modern airfoils, developed for aircraft wings and which are also applied in wind rotors, have an extremely favorable lift-drag ratio. It could show a qualitative utilization of how much an aerodynamic lift force uses as a driving force would have more efficiency. However, to calculate qualitatively of the power coefficients of lift-type wind rotor is no longer possible with just an aid of elementary physical relationships.

2.3 Vertical and Horizontal Axis Wind Rotors

Wind rotors are roughly classified into two types according to their orientations: horizontal axis type and vertical axis type. A horizontal axis wind rotor has its blades rotating on an axis parallel to the ground and a vertical axis one has its blades rotating on an axis perpendicular to the ground. There are numerous designs for both type rotors with different concerns, which are related to diverse situations. Generally, the number of vertical axis wind rotor for commercial uses is much less than that of horizontal axis wind rotor.

2.3.1 Wind Rotors with a Vertical Axis of Rotation

The oldest design of wind rotors is fabricated in vertical axis of rotation. At that time, people only knew using aerodynamic drag force to built vertical axis wind rotors. Aerodynamic lift force would be utilized recently by engineers. Darrieus proposed such design, considered as a promising concept for modern wind turbines in 1925. The Darrieus wind rotor resembles a gigantic eggbeater and its geometric shape is complicated and difficult to manufacture. A wind rotor, called H-rotor, also utilizes aerodynamic lift force. Instead of curved wind rotor blades, the straight blades are connected to the wind rotor shaft by struts. Furthermore, Savonius wind rotor, which is investigated in this research, is one of vertical axis wind rotors. This wind rotor was invented by a Finnish engineer, Savonius [5], in 1922. The structure of Savonius wind rotor is simple with a shape of character “S”, so it is also called S-rotor. Because it is a drag-typed device, Savonius wind rotor extracts much less wind energy than the other similarly-sized lift-type wind rotor, but it has higher starting torque.

2.3.2 Horizontal Axis Wind Rotors

The earliest design of this type of wind turbine was the big Dutch-style windmill, primarily used for milling grain. Another early type of these turbines was the windmill that was built on almost all farms in the early twentieth century. This type of wind turbine is the dominant design in today's wind energy technology. The undisputed superiority of this design to date is primarily based on the reason that the wind rotor blade shape can reach aerodynamically optimized and the highest efficiency can be achieved when aerodynamic lift is utilized appropriately. However, this kind of turbines needs to adjust its direction to face wind direction. To reach this purpose, wind turbines need to use a yaw system, which can move the entire wind rotor left or right in a small increment. It can also control the wind rotor torque and output power by adjusting the wind rotor direction using the pitching mechanism. However, some different construction designs, which are absent with pitching mechanism, are also common. These designs can be found particularly in small wind turbines.

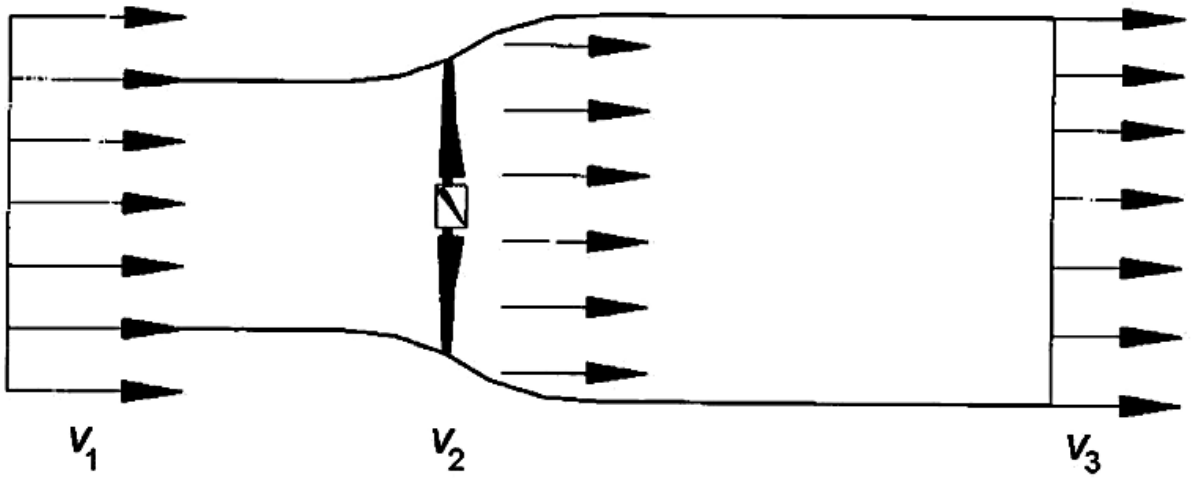

Fig. 2.1 Idealized fluid model for a wind rotor [16]

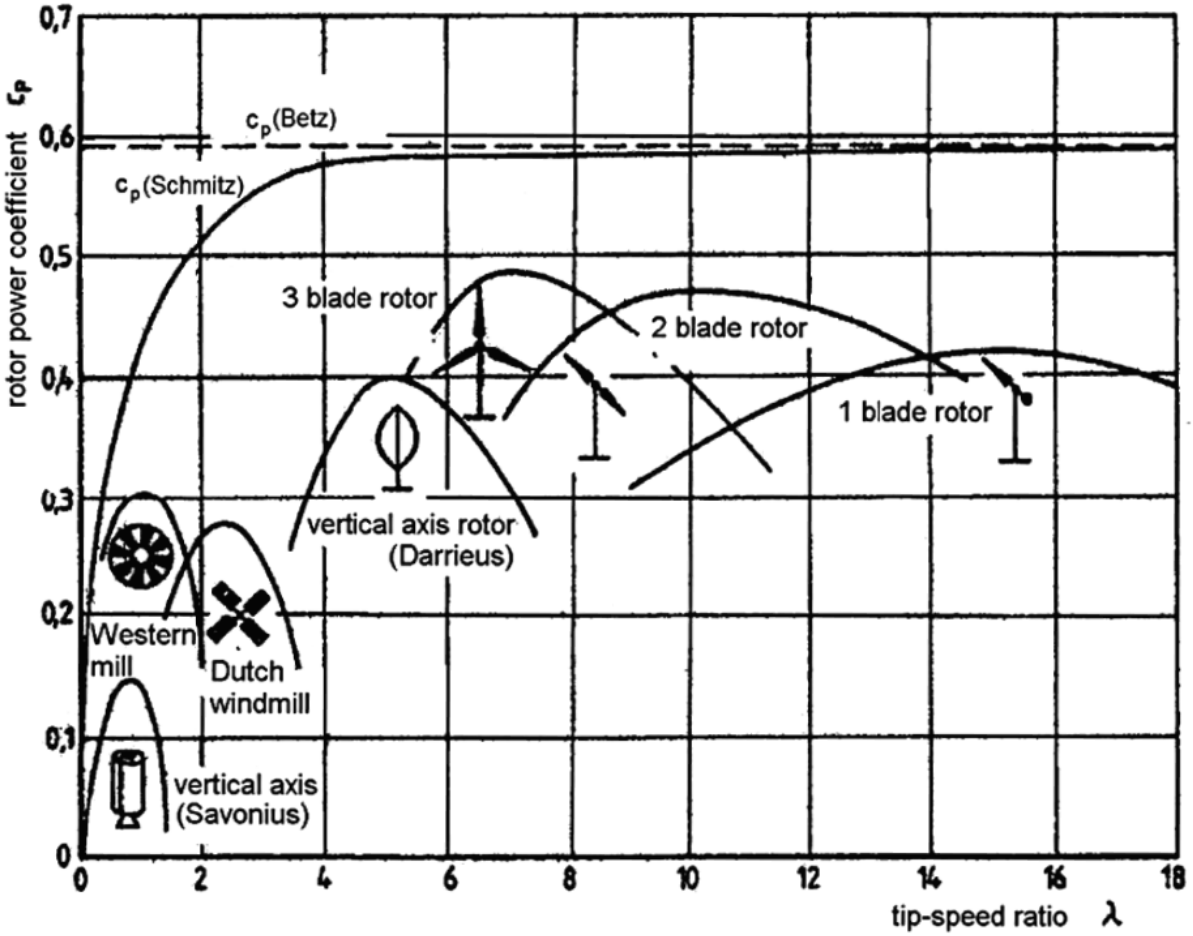

Fig. 2.2 Typical power coefficient of different wind rotor types over tip-speed ratio [16]

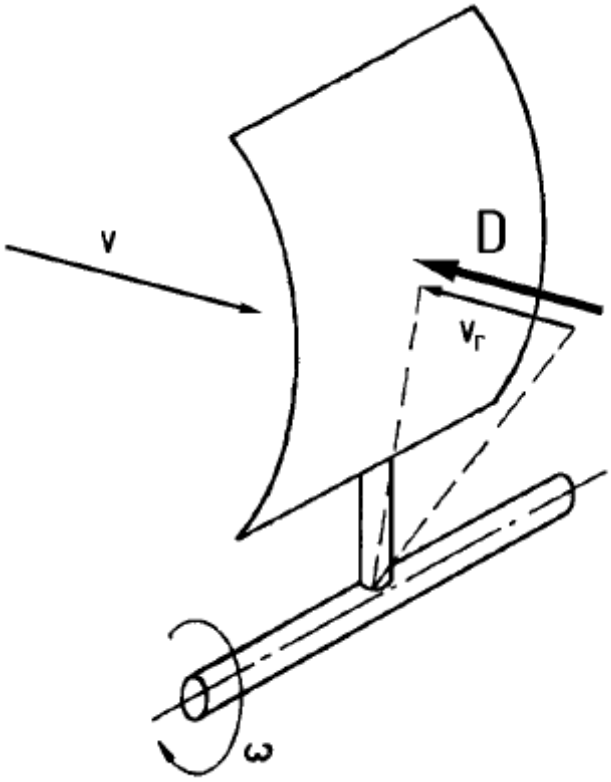

Fig. 2.3 Flow conditions and aerodynamic forces with a drag device [20]

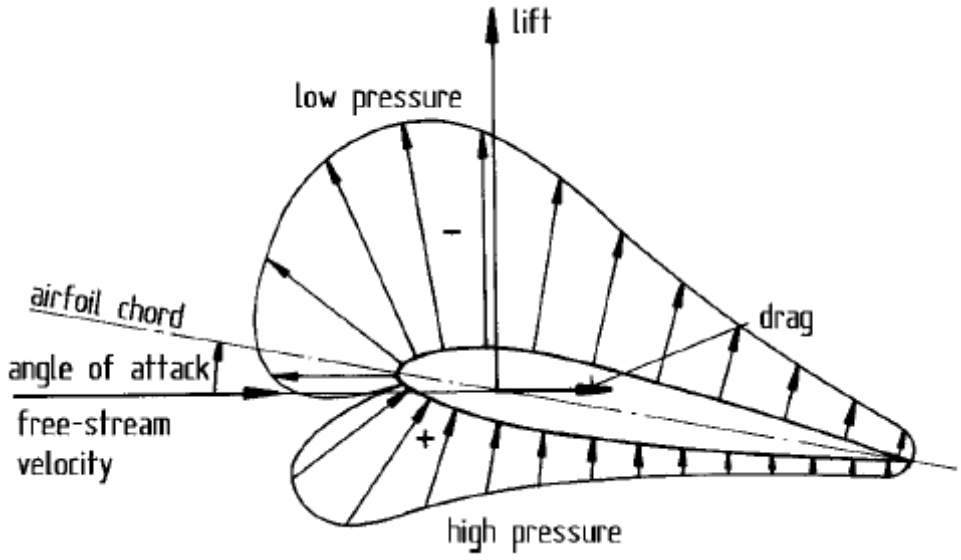

Fig. 2.4 Aerodynamic forces acting on an airfoil exposed to an air stream [20]

CHAPTER 3

METHEMATICAL MODEL AND NUMERICAL ALGORITHM

3.1 Domain Description

The air flow fields around a single rotating Savonius wind rotor and four Savonius wind rotors in parallel matrix system with or without curtain are analyzed numerically under different tip-speed ratios (TSRs) by employing a CFD software, Fluent. The geometry of real wind rotor is shown in **Fig. 3.1,** and the corresponding information is summarized in **Table 3.1**.

Table 3.1 Geometry parameters

Number of Blades	2
Height (mm)	2,340
Rotor Blade Diameter (mm)	1,080
Overlap Ratio of Blades	0.196

In order to compare the C_p between these cases, three types of rectangular domains are set up and are shown in **Fig. 3.2**, **Fig. 3.3** and **Fig. 3.4**, respectively. The dimensions of these domains are listed in **Table 3.2**. For the case of parallel matrix system, the distance between each wind rotors is set 1,400 mm.

Table 3.2 Dimensions of Computational Domains

	Length	Width	Height
One Single Rotor (mm)	26,000	12,000	6,340
Parallel Matrix System without Curtain (mm)	26,000	16,200	6,340
Parallel Matrix System with Curtain (mm)	26,900	21,400	6,340

3.2 Governing Equations

In order to make the model tractable, some assumptions are given as follow:

1. The flow is incompressible and turbulent.
2. The heat transfer and buoyancy effects are neglected.

The generalized governing equations are given below based on these assumptions.

3.2.1 The Continuity and Momentum Equation

Turbulent flows are characterized by fluctuating velocity field. In Reynolds averaging, the solution variables in the instantaneous (exact) Navier-Stokes equations are decomposed into the mean (ensemble-averaged or time-averaged) and fluctuating components. For the velocity components:

$$u_i = \overline{u_i} + u_i' \tag{3-1}$$

where $\overline{u_i}$ and u_i' are the mean and fluctuating velocity components (i = 1, 2, 3). Likewise, for pressure and other scalar quantities:

$$\phi = \overline{\phi} + \phi' \tag{3-2}$$

where ϕ denotes a scalar such as pressure, energy, or species concentration. Substituting expressions of this form for the flow variables into the instantaneous continuity and momentum equations and taking a time (or ensemble) average

(and dropping the over-bar on the mean velocity, $\overline{u}$) yields the ensemble-averaged momentum equations. They can be written in Cartesian tensor form as:

$$\frac{\partial \rho}{\partial t} + \frac{\partial}{\partial x_j}(\rho u_i) = 0 \tag{3-3}$$

$$\frac{\partial}{\partial t}(\rho u_i) + \frac{\partial}{\partial x_j}(\rho u_i u_j) = -\frac{\partial P}{\partial x_i} + \frac{\partial}{\partial x_j}\left[\mu\left(\frac{\partial u_i}{\partial x_j} + \frac{\partial u_j}{\partial x_i} - \frac{2}{3}\delta_{ij}\frac{\partial u_l}{\partial x_l}\right)\right] + \frac{\partial}{\partial x_j}(-\rho\overline{u_i' u_j'}) \tag{3-4}$$

Eqs. (3-3) and (3-4) are called Reynolds-averaged Navier-Stokes (RANS) equations. They have the same general form as the instantaneous Navier-Stokes equations with the velocities and other solution variables now representing ensemble-averaged (or time-averaged) values. Additional terms now appear that represent the effects of turbulence. The Reynolds stress term, $-\rho\overline{u_i' u_j'}$, must be modeled in order to close Eq. (3-4).

3.2.2 RNG *k*-*ε* Model

The RNG-based *k*-*ε* turbulence model is derived from the instantaneous Navier-Stokes equations, using a mathematical technique called "renormalization group" (RNG) methods. The analytical derivation results in a model with constants different from those in the standard *k*-*ε* model. The additional terms and functions in the transport equations for *k* and *ε* are also different.

Transport Equations for the RNG *k*-*ε* Model

The turbulence kinetic energy, *k*, and its rate of dissipation, *ε*, are obtained from the following transport equations:

$$\frac{\partial}{\partial t}(\rho k) + \frac{\partial}{\partial x_i}(\rho k u_i) = \frac{\partial}{\partial x_j}\left(\alpha_k \mu_{eff} \frac{\partial k}{\partial x_j}\right) + G_k - \rho\varepsilon + S_k \quad (3\text{-}5)$$

and

$$\frac{\partial}{\partial t}(\rho\varepsilon) + \frac{\partial}{\partial x_i}(\rho\varepsilon u_i) = \frac{\partial}{\partial x_j}\left(\alpha_\varepsilon \mu_{eff} \frac{\partial \varepsilon}{\partial x_j}\right) + C_{1\varepsilon}\frac{\varepsilon}{k}(G_k) - C_{2\varepsilon}\rho\frac{\varepsilon^2}{k} - R_\varepsilon + S_\varepsilon \quad (3\text{-}6)$$

The term of G_k represents the production of turbulence kinetic energy. Using the exact equation for the transport of k, this term may be defined as $G_k = -\rho\overline{u_i' u_j'}\frac{\partial u_j}{\partial x_i}$. The quantities α_k and α_ε are the inverse effective Prandtl numbers for k and ε, respectively. S_k and S_ε are user-defined source terms.

Modeling the Turbulent Viscosity

The scale elimination procedure in RNG theory produces a differential equation for turbulent viscosity:

$$d\left(\frac{\rho^2 k}{\sqrt{\varepsilon\mu}}\right) = 1.72\frac{\hat{\nu}}{\sqrt{\hat{\nu}^3 - 1 + C_\nu}}d\hat{\nu} \quad (3\text{-}7)$$

where

$$\hat{\nu} = \mu_{eff}/\mu,$$

$$C_\nu \approx 100$$

Eq. (3-7) is integrated to obtain an accurate description of how the effective turbulent transport varies with the effective Reynolds number (or eddy scale), allowing the model to be better handled in the low-Reynolds-number and near-wall flows.

In the high-Reynolds-number limit, Eq. (3-7) gives

$$\mu_t = \rho C_\mu \frac{k^2}{\varepsilon} \quad (3\text{-}8)$$

with $C_\mu = 0.0845$, derived using RNG theory.

RNG Swirl Modification

Turbulence, in general, is affected by rotation or swirl in the mean flow. The RNG model in Fluent provides an option to account for the effects of swirl or rotation by modifying the turbulent viscosity appropriately. The modification takes the following functional form:

$$\mu_t = \mu_{t0}\, f(\alpha_s, \Omega, \frac{k}{\varepsilon}) \tag{3-9}$$

where μ_{t0} is the value of turbulent viscosity calculated without the swirl modification using either Eq. (3-7) or Eq. (3-8). Ω is a characteristic swirl number evaluated within Fluent, and α_s is a swirl constant that assumes different values depending on whether the flow is swirl-dominated or only mildly swirling. This swirl modification always takes effect for axisymmetric, swirling flows and three-dimensional flows when the RNG model is selected. For mild swirling flows (the default in Fluent), α_s is set to 0.07. For strong swirling flows, however, a higher value of α_s can be used.

Calculating the Inverse Effective Prandtl Numbers

The inverse effective Prandtl numbers, k and ε, are computed using the following formula derived analytically by the RNG theory:

$$\left|\frac{\alpha-1.3929}{\alpha_0-1.3929}\right|^{0.6321}\left|\frac{\alpha+2.3929}{\alpha_0+2.3929}\right|^{0.3769} = \frac{\mu_{mol}}{\mu_{eff}} \tag{3-10}$$

where $\alpha_0 = 1.0$. In the high-Reynolds-number limit ($\frac{\mu_{mol}}{\mu_{eff}} \ll 1$), $\alpha_k = \alpha_\varepsilon \approx 1.393$.

The R_ε in the ε Equation

The main difference between the RNG and standard k-ε models lies in the additional term in the ε equation given by

$$R_{\varepsilon=}\frac{C_\mu\rho\eta^3(1-\eta/\eta_0)}{1+\beta\eta^3}\frac{\varepsilon^2}{k} \tag{3-11}$$

where $\eta \equiv S_k/\varepsilon$, $\eta_0 = 4.38$, $\beta = 0.012$.

The effects of this term in the RNG ε equation can be seen more clearly by rearranging Eq. (3-6). Using Eq. (3-11), the third and fourth terms on the right-hand side of Eq. (3-6) can be merged, and the resultant ε equation can be rewritten as

$$\frac{\partial}{\partial t}(\rho\varepsilon)+\frac{\partial}{\partial x_i}(\rho\varepsilon u_i)=\frac{\partial}{\partial x_j}\left(\alpha_\varepsilon\mu_{eff}\frac{\partial\varepsilon}{\partial x_j}\right)+C_{1\varepsilon}\frac{\varepsilon}{k}(G_k+C_{3\varepsilon}G_b)-C_{2\varepsilon}^*\rho\frac{\varepsilon^2}{k} \tag{3-12}$$

where $C_{2\varepsilon}^*$ is given by

$$C_{2\varepsilon}^*\equiv C_{2\varepsilon}+\frac{C_\mu\eta^3(1-\eta/\eta_0)}{1+\beta\eta^3} \tag{3-13}$$

In regions where $\eta < \eta_0$, the R term makes a positive contribution, and $C_{2\varepsilon}^*$ becomes larger than $C_{2\varepsilon}$. In the logarithmic layer, for instance, it can be shown that $\eta \approx 3.0$ gives $C_{2\varepsilon}^* \approx 2.0$, which is close in magnitude to the value of $C_{2\varepsilon}^*$ in the standard k-ε model (1.92). As a result, for weakly to moderately strained flows, the RNG model tends to give results largely comparable to the standard k-ε model.

In regions of large strain rate ($\eta > \eta_0$), however, the R term makes a negative contribution, making the value of $C_{2\varepsilon}^*$ less than $C_{2\varepsilon}$. In comparison with the standard k-ε model, the smaller destruction of ε augments ε, reducing k and, eventually, the effective viscosity. As a result, in rapidly strained flows, the RNG model yields a lower turbulent viscosity than the standard k-ε model.

Thus, the RNG model is more responsive to the effects of rapid strain and streamlining curvature than the standard k-ε model, which explains the superior performance of the RNG model for certain classes of flows.

Model Constant

The model constants $C_{1\varepsilon}$ and $C_{2\varepsilon}$ in Eq. (3-6) have values derived analytically by the RNG theory. These values, used by default in Fluent, are

$$C_{1\varepsilon} = 1.42;\ C_{2\varepsilon} = 1.68$$

3.2.3 Standard Wall Functions

The standard wall functions in Fluent are based on the proposal of Launder and Spalding (1974), and have been most widely used for industrial flows.

Momentum

The law-of-the-wall for mean velocity yields

$$U^* = \frac{1}{k} ln(Ey^*) \tag{3-14}$$

where

$$U^* \equiv \frac{U_P C_\mu^{1/4} k_P^{1/2}}{\tau_w/\rho} \tag{3-15}$$

$$y^* \equiv \frac{\rho C_\mu^{1/4} k_P^{1/2} y_P}{\mu} \tag{3-16}$$

In which

k = von Karman constant (= 0.487)

E = empirical constant (= 9.793)

U_P = mean velocity of the fluid at point P

K_P = turbulent kinetic energy at point P

y_P = distance from point P to the wall

μ = dynamic viscosity of the fluid

3.3 Boundary Conditions

In the domain of interest mentioned above, boundary conditions are described at the rotating wind rotor, inlet surfaces, outlet surfaces, side surfaces (atmosphere), and walls (curtain).

1. Rotation boundary condition

According to Eq. (2-3), the angular speed ω (rad/s) of the wind rotor is expressed as

$$\omega = \frac{2v_1\lambda}{D} \tag{3-23}$$

where D is the outer wind rotor diameter, ω the angular wind rotor speed, v_1 the wind velocity, and λ the tip-speed ratio (TSR).

2. The inlet boundary condition

The inlet boundary conditions are:

$$u = u_{in}$$

$$v = 0$$

$$w = 0$$

where u, v and w represent the velocity components in X, Y and Z directions, respectively.

3. The outflow boundary condition

Outflow boundary conditions are applied at downstream flow exit, where the details of the local velocity and pressure are not known in advance. It is set by Fluent (2010) internally that the mass conservation is definitely maintained.

4. The symmetrical boundary condition

In the atmospheric case, the free surface boundary conditions, where the local velocity gradient approximate zero, are applied for side surfaces, provided that the distances are far enough from the center line of the domain. Via a series of numerical tests, the distance between the free surface and center line is chosen five times of the rotor diameter as Akwa et al. [21] do.

5. Wall boundary condition

The wall boundary conditions satisfy the no-slip condition that are $u, v, w = 0$.

3.4 Introduction to Fluent Software

Fluent is a state-of-the-art computer program for modeling fluid flow and heat transfer in complex geometries. It provides complete mesh flexibility, including the ability to solve the flow problems using unstructured meshes that can be generated about complex geometries with relative ease. Supported mesh types include 2-D triangular/quadrilateral, 3-D tetrahedral/hexahedral/pyramid, and mixed (hybrid) meshes. Fluent also allows refining or coarsening grid based on the flow solution.

Fluent is written in the C computer language and makes full use of the flexibility and power offered by the language. Consequently, true dynamic memory allocation, efficient data structures, and flexible solver control are all possible. In addition, Fluent uses a client/server architecture, which allows it to run as separate simultaneous processes on client desktop workstations and powerful computational servers. This architecture allows for efficient execution, interactive control, and complete flexibility between different types of machines

or operating systems.

All functions required to compute a solution and display the results are accessible in Fluent through an interactive, menu-driven interface.

3.5 Numerical Method

This study employs the computational fluid dynamics software Fluent to analyze the flow fields around rotating Savonius wind rotors. The finite volume iteration and SIMPLE algorithm are put in use to solve the governing equations of a transient flow field. And the corresponding grid movement is also solved by using sliding mesh method.

Fluent uses Segregated Solver method to solve the governing integral equations for the conservation of mass and momentum, and (when appropriate) for energy and other scalars such as turbulence and chemical species. In case a control-volume-based technique is used that consists of:

1. Division of domain into discrete control volumes using a computational grid.
2. Integration of the governing equations on the individual control volumes to construct algebraic equations for the discrete dependent variables such as velocities, pressure, temperature, and conserved scalars.
3. Linearization of the discretized equations and solutions of the resultant linear equation system yield updated values of the dependent variables.

3.5.1 Segregated Solution Method

Using this approach, the governing equations are solved sequentially (i.e., segregated from one another). Because the governing equations are non-linear (and coupled), several iterations of the solution loop must be performed before a

converged solution is obtained. Each time of iteration consists of the steps illustrated in **Fig. 3.5** and outlined below:

1. Fluid properties are updated, based on the current solution. (If the calculation has just begun, the fluid properties will be updated based on the initialized solution.)
2. The *u*, *v*, and *w* momentum equations are each solved in turn using current values for pressure and face mass fluxes, in order to update the velocity field.
3. Since the velocities obtained in Step 2 may not satisfy the continuity equation locally, a Poisson-type equation for the pressure correction is derived from the continuity equation and the linearized momentum equations. This pressure correction equation is then solved to obtain the necessary corrections to the pressure and velocity fields and the face mass fluxes that continuity is satisfied.
4. Where appropriate equations for scalars such as turbulence, energy, species, and radiation are solved using the previously updated values of the other variables.
5. When inter-phase coupling is to be included, the source terms in the appropriate continuous phase equations may be updated with a discrete phase trajectory calculation.
6. A check for convergence of the equation set is made.

These steps are continued until the convergence criteria are met.

3.5.2 Linearization: Implicit

In the segregated solution method the discrete, non-linear governing equations are linearized to produce a system of equations for the dependent variables in every computational cell. The resultant linear system is then solved to

yield an updated flow-field solution.

The manner in which the governing equations are linearized may take an implicit form with respect to the dependent variable (or set of variables) of interest. The implicit form is described in the following:

Implicit

For a given variable, the unknown value in each cell is computed using a relation that includes both existing and unknown values from neighboring cells. Therefore each unknown will appear in more than one equation in the system, and these equations must be solved simultaneously to give the unknown quantities.

In the segregated solution method each discrete governing equation is linearized implicitly with respect to that equation's dependent variable. This will result in a system of linear equations with one equation for each cell in the domain. Because there is only one equation per cell, this is sometimes called a scalar system of equations. A point implicit (Gauss-Seidel) linear equation solver is used in conjunction with an algebraic multi-grid (AMG) method to solve the resultant scalar system of equations for the dependent variable in each cell. For example, the *x*-momentum equation is linearized to produce a system of equations in which *u*-velocity is the unknown. Simultaneous solution of this equation system (using the scalar AMG solver) yields an updated *u*-velocity field.

In summary, the segregated approach solves for a single variable field (e.g., p) by considering all cells at the same time. It then solves for the next variable field by again considering all cells at the same time, and so on. There is no explicit option for the segregated solver.

3.5.3 Discretization

Fluent uses a control-volume-based technique to convert the governing equations to algebraic equations that can be solved numerically. This control volume technique consists of integrating the governing equations about each control volume, yielding discrete equations that conserve each quantity on a control volume basis.

Discretization of the governing equations can be illustrated most easily by considering the steady-state conservation equation for transport of a scalar quantity ϕ. This is demonstrated by the following equation written in integral form for an arbitrary control volume V as follows:

$$\oint \rho\phi\vec{v} \cdot d\vec{A} = \oint \Gamma_\phi \nabla\phi \cdot d\vec{A} + \oint_V S_\phi dV \qquad (3\text{-}24)$$

where

ρ = density

$\vec{v}$ = velocity vector

$\vec{A}$ = surface area vector

Γ_ϕ = diffusion coefficient for ϕ

$\nabla\phi$ = gradient of ϕ

S_ϕ = source of ϕ per unit volume

Eq. (3-24) is applied to each control volume, or cell, in the computational domain. The two-dimension, triangular cell shown in **Fig. 3.6** is an example of such a control volume. Discretization of Eq. (3-24) on a given cell yields

$$\sum_f^{N_{faces}} \rho_f \overrightarrow{v_f} \phi_f \cdot \overrightarrow{A_f} = \sum_f^{N_{faces}} \Gamma_\phi (\nabla\phi)_n \cdot \overrightarrow{A_f} + S_\phi V \qquad (3\text{-}25)$$

where

N_{faces} = number of faces enclosing cell

ϕ_f = value of ϕ convected through face f

$\rho_f \overrightarrow{v_f} \cdot \overrightarrow{A_f}$ = mass flux through the face

$\overrightarrow{A_f}$ = area of face f

$(\nabla\phi)_n$ = magnitude of $\nabla\phi$ normal to face f

V = cell volume

The equations solved by Fluent take the same general form as the one given above and apply readily to multi-dimension, unstructured meshes composed of arbitrary polyhedral.

By default, Fluent stores discrete values of the scalar ϕ at the cell center (c0 and c1 in **Fig. 3.6**). However, face values ϕ_f are required for the convection terms in Eq. (3-25) and must be interpolated from the cell center values. This is accomplished using an upwind scheme.

First-Order Upwind Scheme

When first-order accuracy is desired, quantities at cell faces are determined by assuming that the cell-center values of any field variable represent a cell-average value and hold throughout the entire cell; the face quantities are identical to the cell quantities. Thus when first-order upwind is selected, the face value ϕ_f is set equal to the cell-center value of ϕ in the upstream cell.

3.5.4 Simple Algorithm

The SIMPLE algorithm uses a relationship between velocity and pressure corrections to enforce mass conservation and to obtain the pressure field.

If the momentum equation is solved with a guessed pressure field p^*, the

resulting face flux J_f^*, computed from $J_f = \hat{J}_f + d_f(p_{c0} - p_{c1})$ (where p_{c0} and p_{c1} are the pressures within the two cells on either side of the face, and $\hat{J}_f$ contains the influence of velocities in these cell. The term d_f is a function of $\overline{a}_p$, the average of the momentum equation $\overline{a}_p$ coefficients for the cells on either side of face *f*.)

$$J_f^* = \hat{J}^*_f + d_f(p^*_{c0} - p^*_{c1}) \tag{3-26}$$

does not satisfy the continuity equation. Consequently, a correction J_f' is added to the face flux J_f^* so that the corrected face flux, J_f

$$J_f = J_f^* + J_f' \tag{3-27}$$

satisfies the continuity equation. The SIMPLE algorithm postulates that J_f' be written as

$$J_f' = d_f(p'_{c0} + p'_{c1}) \tag{3-28}$$

where p' is the cell pressure correction.

The SIMPLE algorithm substitutes the flux correction equations, Eq. (3-27) and (3-28), into the discrete continuity equation ($\sum_f^{N_{faces}} J_f A_f = 0$) to obtain a discrete equation for the pressure correction p' in the cell:

$$a_p p' = \sum_{nb} a_{nb} p'_{nb} + b \tag{3-29}$$

where the source term *b* is the net flow rate into the cell:

$$b = \sum_f^{N_{faces}} J_f^* A_f \tag{3-30}$$

The pressure-correction equation, Eq. (3-29), may be solved using the algebraic multigrid (AMG) method. Once a solution is obtained, the cell pressure

and the face flux are used correctly.

$$p = p^* + \alpha_p p' \tag{3-31}$$

$$J_f = J_f^* + d_f(p'_{c0} - p'_{c1}) \tag{3-32}$$

Here α_p is the under-relaxation factor for pressure. The corrected face flux J_f satisfies the discrete continuity equation identically during each time of iteration.

3.5.5 Sliding Mesh

The sliding mesh model allows adjacent grids to slide relative to one another. In doing so, the grid faces do not need to be aligned on the grid interface. This setup requires a means of computing the flux across the two non-conformal interface zones of each grid interface.

To compute the interface flux, the intersection between the interface zones is determined at each new time step. The resulting intersection produces one interior zone (a zone with fluid cells on both sides) and one or more periodic zones. If the problem is not periodic, the intersection produces one interior zone and a pair of wall zones (which will be empty if the two interface zones completely intersect), as shown in **Fig. 3.7**. The resultant interior zone corresponds to where the two interface zones overlap; the resultant periodic zone corresponds to where they do not. The number of faces in these intersection zones will vary as the interface zones move relative to one another. Principally, fluxes across the grid interface are computed using the faces resulting from the intersection of the two interface zones (rather than from the interface zone faces themselves).

In the example shown in **Fig. 3.8**, the interface zones are composed of faces

A-B and B-C, and faces D-E and E-F. The intersection of these zones produces the faces a-d, d-b, b-e, etc. Faces produced in the region where the two cell zones overlap (d-b, b-e, and e-c) are grouped to form an interior zone, while the remaining faces (a-d and c-f) are paired up to form a periodic zone. To compute the flux across the interface into cell IV, for example, face D-E is ignored and faces d-b and b-e are used instead, bringing information into cell IV from cells I and III, respectively.

3.6 Computational Procedure of Simulation

The complete operating procedure by using Fluent package software is carried out through the following processes sequentially.

3.6.1 Model Geometry

Before Fluent calculations, it is necessary to build a model. This study used the pre-processor software Gambit to build the geometry of the model. Divide the geometry into finite volumes in order to generate grids conveniently. The details of geometry information can be referred to **Section 3.1**.

3.6.2 Grid Generation

After building the geometry, the model has to use the pre-processor Gambit to generate grids as shown in **Fig. 3.9**. This step defines the different grid sizes in different volumes. The smaller grid size for the small volume will increase the accuracy of the simulation, but it also produce larger grid number which cause calculation difficulty. To consider the appropriate grid size for grid generation is important. The grid generation usually reduced the calculation cost under

acceptable accuracy.

3.6.3 Fluent Calculation

To determine and solve the important features of the problem follow the basic procedural steps and get the results. Before starting Fluent, create the model geometry and grid as mentioned in **3.6.1** and **3.6.2**. Then starts Fluent with choose an appropriate solver for 2-D or 3-D modeling. In the beginning, import the mesh grid file and check the grid. After that, various settings and parameters need to be confirmed. Select the solver formulation and choose the basic equations (e.g., laminar, turbulent, inviscid, chemical species, or heat transfer models, etc.) to solve the problem. Identify additional models needed such as fans, heat exchangers, porous media, etc. Specify material properties and the boundary conditions. Adjust the solution control parameters. Give an initialized value for iterate the flow field model. Finish those foregoing steps, start to calculate a solution and examine the results. If necessary, refine the grid or consider revisions to the numerical or physical model.

3.6.4 Grid-independence Test

The grid-independence test should be taken in advance to have a trade-off between the guarantee of acceptable accuracy and an affordable calculation cost.

As described in **Section 3.1**, there are two types of rectangular calculation domains: a single Savonius wind rotor and the parallel matrix system with four Savonius wind rotors. The grid-independence tests in 3-D simulation of this study can be separated into z-axis direction and x-y plane direction in one single Savonius wind rotor with the boundary conditions of wind velocity 7 m/s and TSR 0.8.

In the case of one single Savonius wind rotor, grid-independence test of z-axis direction is carried out. Grid numbers of 60, 80, 100, 120 and 140 in z-axis are tested and the simulation results are shown in **Fig. 3.10(a)** and **Table 3.3**. Because the changing rate of C_p from grid number 100 to 120 is small enough and remains almost the same value while the grid number increases, the grid number of 100 is selected.

Table 3.3 Grid-independence Tests in z-axis

Grid Number (z-axis)	C_p	Changing Rate (%)
60	0.173	
80	0.178	0.025%
100	0.181	0.015%
120	0.180	-0.005%
140	0.181	0.005%

The grid numbers of 4,750, 4,840, 5,024, 5,232, 5,452, 5,898 and 6,492 in x-y plane are tested in the case of one single Savonius wind rotor. The results are shown in **Fig. 3.10 (b)** and **Table 3.4**. Similar to the reason as described in the case in z-axis, grid number of 5,452 is chosen.

Table 3.4 Grid-independence Tests in x-y Plane

Grid Number (x-y Plane)	C_p	Changing Rate (%)
4,750	0.175	
4,840	0.176	0.0011%
5,024	0.178	0.0011%
5,232	0.180	0.00096%
5,452	0.181	0.00045%
5,898	0.180	-0.00022%
6,492	0.181	0.00017%

Following the procedure for the grid-independence tests of one single Savonius wind rotor in z-axis and x-y plane, the grid number of the parallel matrix system with four Savonius wind rotors domain is set accordingly, and the set grid numbers of three domains are listed in **Table 3.5**.

Table 3.5 Grid Numbers of Two Domains

	Grid Number (3-D)
One Single Rotor	657,400
Parallel Matrix System without Curtain	1,827,520
Parallel Matrix System with Curtain	2,980,600

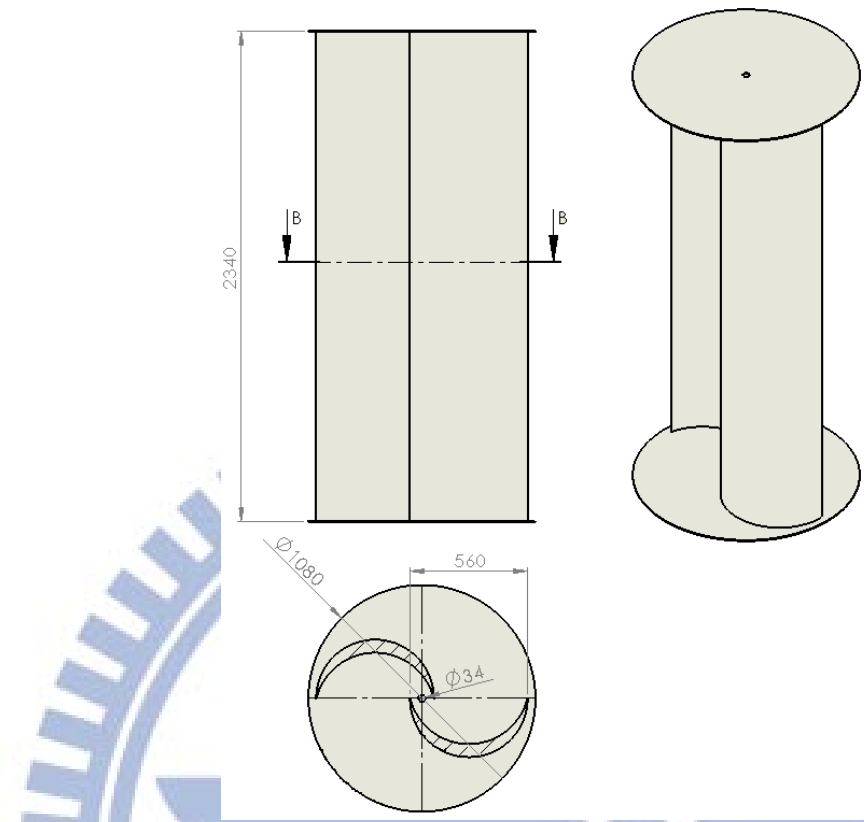

Fig. 3.1 Schematics of Savonius wind rotor geometry in experimental study

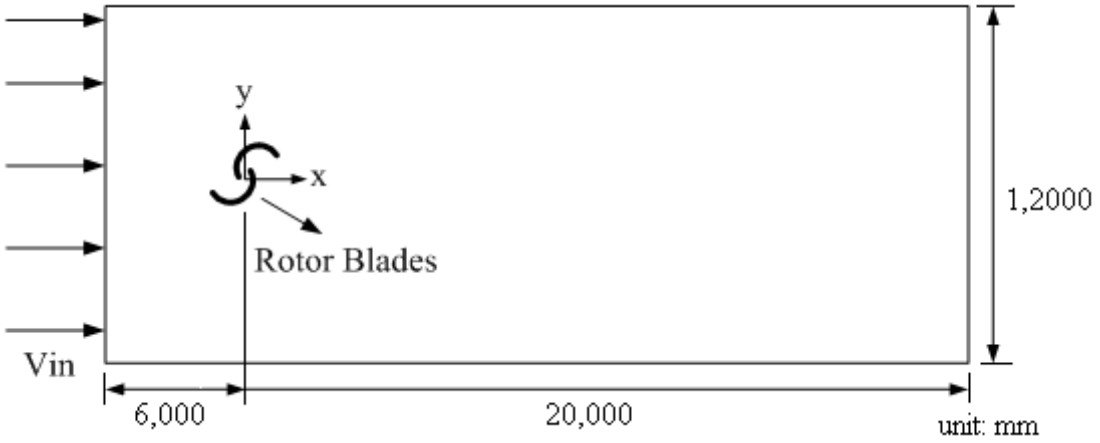

Fig. 3.2 The domain of a single Savonius wind rotor

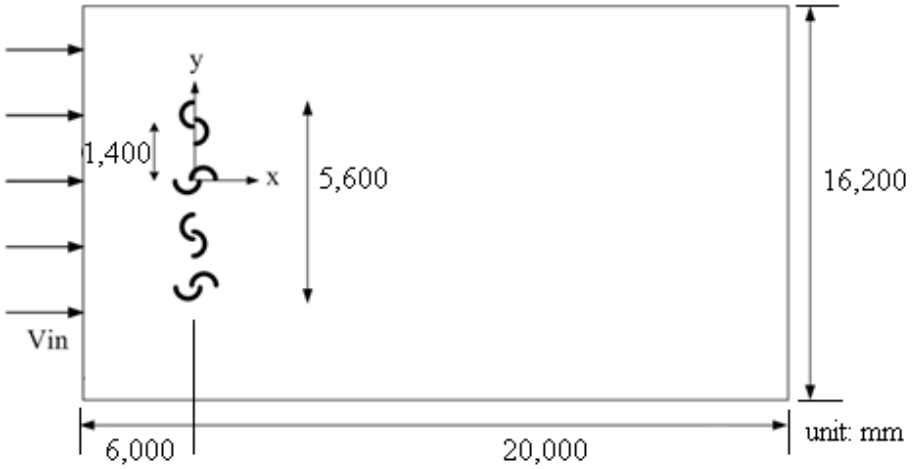

Fig. 3.3 The domain of four two-bladed Savonius wind rotors without curtain in parallel matrix system

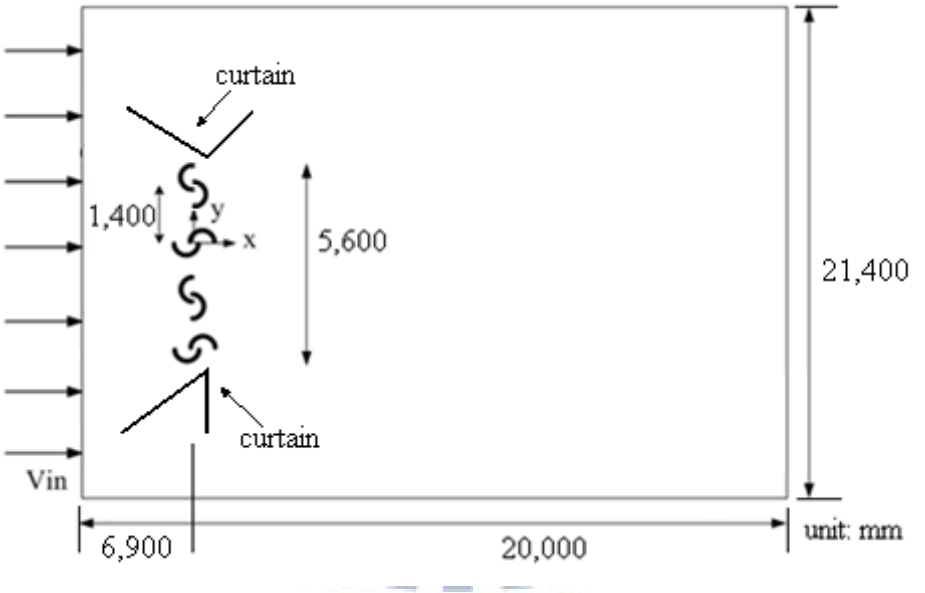

Fig. 3.4 The domain of four two-bladed Savonius wind rotors with curtain in parallel matrix system

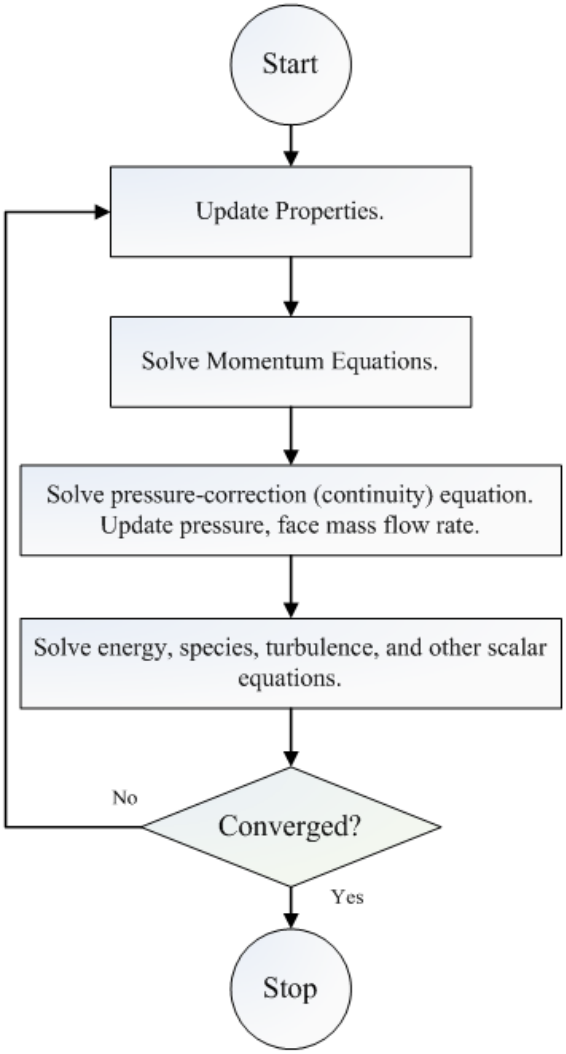

Fig. 3.5 Overview of the segregated solution method

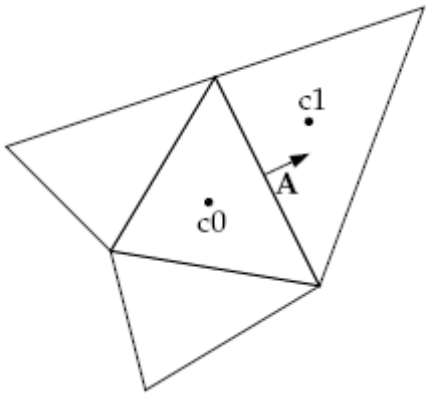

Fig. 3.6 Control volume used to illustrate discretization of a scalar transport equation

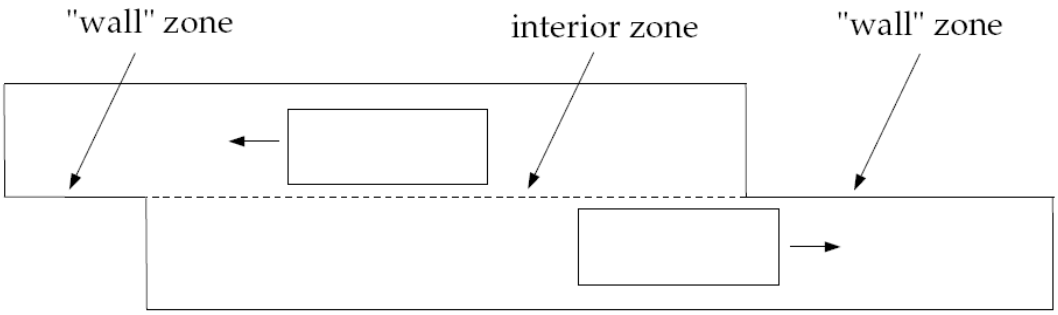

Fig. 3.7 Zones created by non-periodic interface intersection

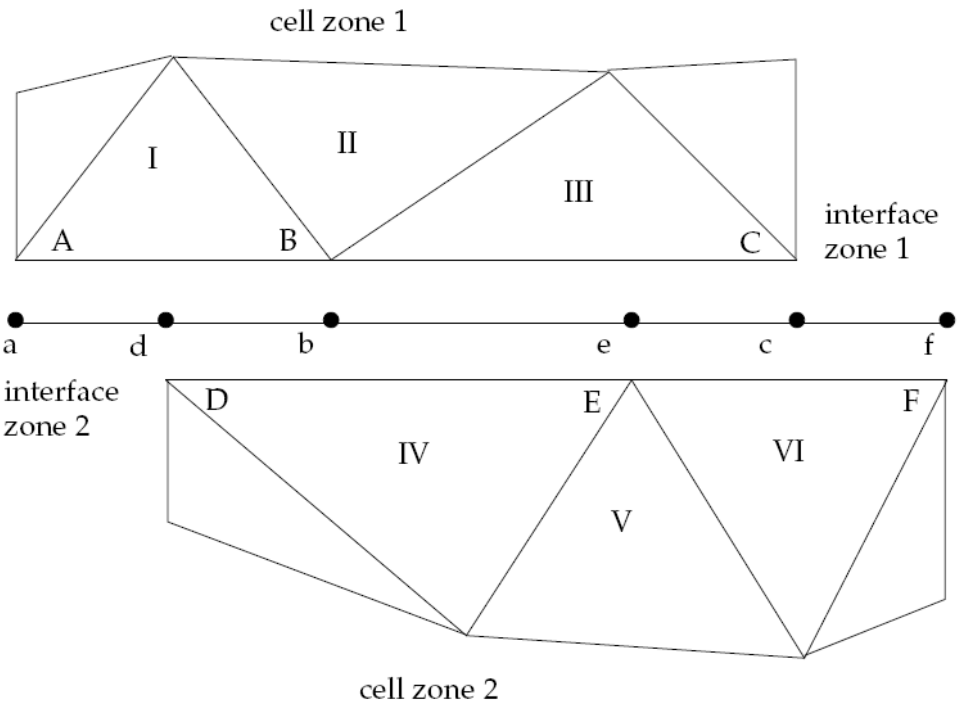

Fig. 3.8 Two-dimensional grid interface

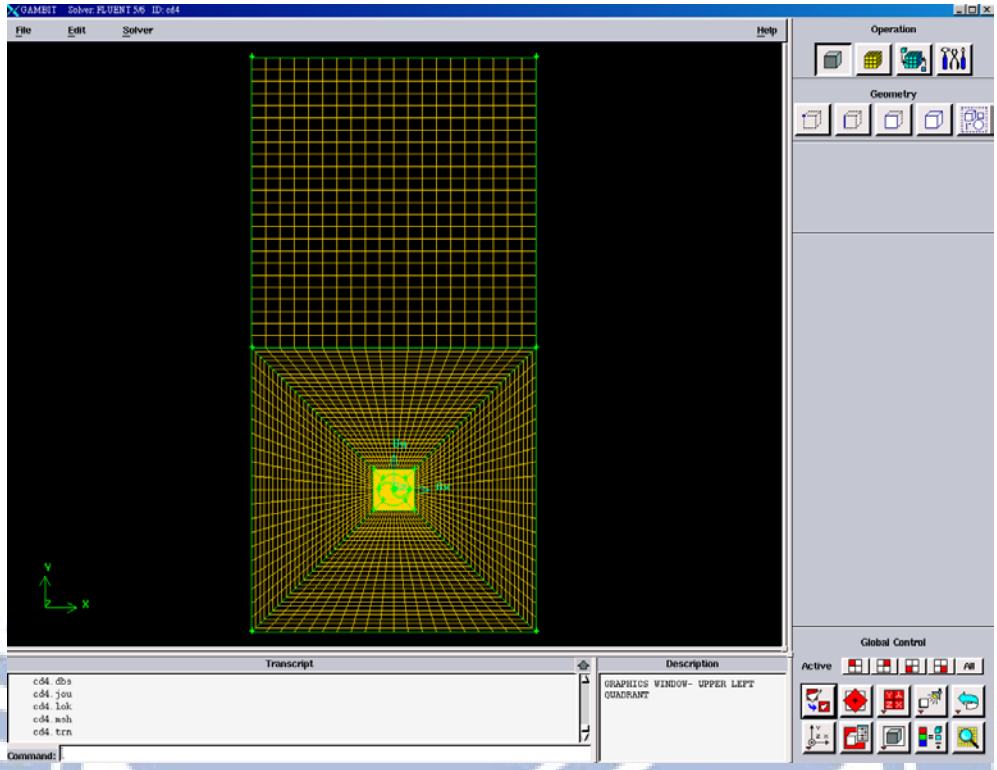

Fig. 3.9 User interface of Gambit

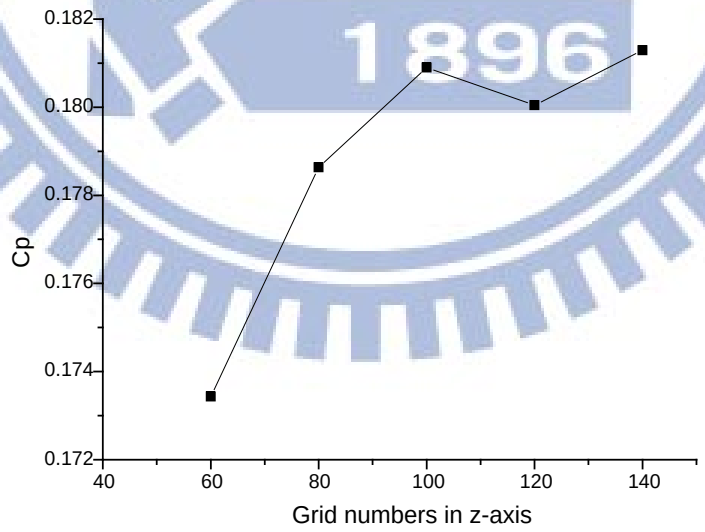

(a)

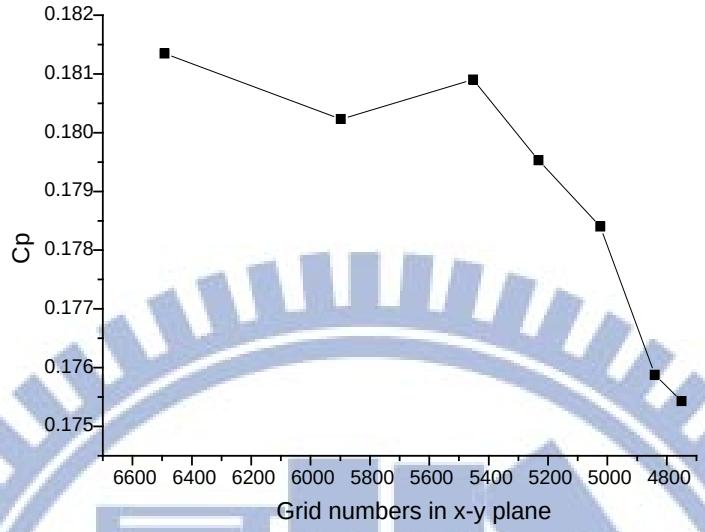

(b)

Fig. 3.10 Grid-independent test: (a) z-axis; (b) x-y plane

CHAPTER 4

EXPERIMENTAL APPARATUSES

4.1 Experiment Layout

The experimental layout is shown in **Fig. 4.1**. The system can be separated into mechanical part and electrical one. In the former part, wind rotors extract wind energy to transform into mechanical energy and then drive the train to transmit mechanical energy to generators, which converts mechanical energy to electric energy. The latter part utilizes sensors to detect the environment and generated power. PLC collects the sensors' data to control or charge batteries. After that, the processed electricity can be connected to the local grid for further use.

4.2 Mechanical Part

Four two-bladed Savonius wind rotors system in parallel matrix is established. The design diagram, shown in **Fig. 4.2,** is crucial to earlier manufacturing that is drawn by Auto-CAD. The manufacturer fabricates the facility according to the design diagram. This stand-along wind power system is located at Zhubei, a suburb of Hsinchu City.

4.2.1 Wind Rotor

In this study, two-bladed Savonius wind rotor is selected to be used in the area of low speed wind with large fluctuation. Arrange the rotors into parallel matrix with 90° phase angle deference for improving the power coefficient (C_p) according to the Feng's suggestion [3]. The geometric data of the wind rotor is

shown in **Fig. 3.1**, and **Table 3.1**. The distance between two wind rotors is 1,400 mm. Considering the monsoon, in which the south wind blows in summer and the north wind blows in winter, the parallel matrix system is oriented in south-north direction, coincident with the wind direction such that the rotors can always face wind.

4.2.2 Drive Train

The wind rotor is connected to the drive train for transmitting the mechanical energy to generator. According to the requirement, the drive train usually is arranged with cross-diverter to change the transmission direction and to change the torque and rotating speed with pulleys. The combination is shown in **Fig. 4.3**.

Cross-diverter

Cross-diverter is utilized to divert the transmission direction by bevel gears. In this study, HLC-6M/U-LR typed cross-diverter, produced by Huang Tih Gear Industry Co., Ltd, is selected. The geometry is shown at **Fig. 4.4** and its transmission ability is shown in **Table 4.1** as well. The transmission efficiency is reached approximately 95%.

Table 4.1 Transmission Ability [22]

Speed Ratio	Input Shaft	HLG-6M		
	Rotating Speed r/min	Input Force kW	Output Shaft Torque	
			N · m	{kgf · m}
1 : 1	3000	22.8	71.1	{7.25}
	2000	18.6	87.0	{8.87}
	1750	17.1	91.1	{9.30}
	1450	14.9	96.0	{9.80}
	1150	12.7	103	{10.5}
	870	10.5	113	{11.5}
	580	7.35	119	{12.1}
	300	3.93	123	{12.5}
	100	1.36	127	{13.0}

Belt Pulleys

The rotational speed of Savonius wind rotors is lower, so it utilizes a large diameter pulley to drive a small diameter pulley to make generator having enough operating speed. This system selects three groove wedge belt pulleys and their data are listed at **Table 4.2,** which is corresponding to **Fig. 4.5**.

Table 4.2 Data of Wedge Pulleys

Description	Dp.	Od.	Form	Bush No.	Max Bore	F	J	L	M	N
SPA 125x4	125	130.5	2	2012	50	65	91	32	33.0	-
SPA 400x3	400	405.5	4	3020	75	50	365	51	1.00	159

4.2.3 Generator

Generator is a device that converts mechanical energy to electrical energy. This work selects Rare-earth permanent magnet generator of 1 kW, 360 rpm and DC 56 V. This kind of generator has simple structure that reduces the breakdown time, because it has no slip ring and brush. Adding the rare-earth element can increase the density of magnetic lines that improves the performance of generator. The performance testing report is listed in **Table 4.3** and its exterior size is shown in **Fig. 4.6**.

Table 4.3 Performance Testing Report of 1kW Generator

Item	Design Index						
rpm / Performance Index	360	0	195	234	300	360	450
Idling Test							
Idling DC Volt	≧DC56	0	55.79	66.95	85.83	103	133.25
Loading Test							
Volt	DC56	0	41	56	56	56	56
Ampere	17.86	0	5.94	7.13	12.3	18.6	30.6
Watt	1000	0	243.54	399.28	688.8	1041.6	1713.6

4.2.4 Curtain

To put curtain can concentrate the wind energy to reach higher efficiency. The arrangement of curtains beside the wind rotors is shown in **Figs. 4.2** and **4.7**.

The sizes of the curtains are 2,000 mm×3,535 mm and 2,645 mm×3,535 mm and their arrangement is aligned with the wind direction.

4.3 Electrical Part

For the electrical part, electrical circuit rectifies the electric energy and charges it to batteries for stand-along system. It is simply divided into the main circuit and control circuit.

4.3.1 Main Circuit

The main circuit contains rectifier, batteries and several magnetic contactors with resistors. The function of this part is to deal with electric power, such as rectification, transmission and charging the batteries; see **Fig. 4.8**. It rectifies generated power with rectifier and battery. The processed electricity can then be connected to the local grid for further use.

Rectifier

The alternating current (AC) is rectified to direct current (DC) for battery charging. It selects 60MT100KB three-phase bridge rectifier, whose ampere resistance can reach 60 A, and voltage resistance can reach 800 V. The structure of rectifier and its circuit are shown in **Fig. 4.9**.

Magnetic Contactor

For controlling the electric energy being steady, it adds different loadings via giving signal to magnetic contactors. It selects SD-P21 magnetic contactor, produced by Shihlin Electric & Engineering Co., which is driven by DC 24 V.

The ampere resistance of SD-P21 can reach 40 A. **Fig. 4.10** shows the dimension of SD-P21 magnetic contactor.

Resistor

Resistors are the loadings which placed at secondary side of magnetic contactors. Select power-type wire wounding the resistor with 100 W and 200 W to deal with different loading requirements, see **Fig. 4.11**. This kind of resistor has higher power resistance, so it can be well used at power generating system. Input different numbers of resistor to adjust wind rotors' rotating speed that can receive steady electric energy. The resistor also can use as brake. In this study, 1500 W power-type wire wounding resistor is selected as wind rotors' brake. It can produces heavy loading immediately and makes the rotors stop.

Battery

For a stand-along system, battery is an essential component to supply power. In this experiment, REC22-12, made by Taiwan YUASA battery Co., Ltd., is chosen. Its dimension is 181 mm×76.2 mm×167 mm, as shown in **Fig. 4.12**. To deal with charging and discharging frequently conditions in wind power system, this kind of battery can be affordable in these situations. The battery discharge capacity is shown at **Table 4.4**.

Table 4.4 Discharge Capacity

Performance Data at 25℃ - Amperes and Watts										
F.V. \ Time		5m	10m	15m	30m	1h	3h	5h	10h	20h
10.8V	W	1002	702	526	316	181	70.0	45.7	23.9	12.9
	A	89.0	61.8	45.3	26.9	15.2	5.84	3.80	1.99	1.06
10.5V	W	1048	726	539	322	183	70.7	46.1	24.1	12.9
	A	94.4	64.3	46.6	27.4	15.4	5.9	3.83	2.00	1.07
10.2V	W	1093	744	549	326	185	71.2	46.4	24.2	13.0
	A	98.7	65.6	47.3	27.8	15.6	5.94	3.85	2.01	1.07
9.6V	W	1180	761	557	330	187	72.2	47.2	24.7	13.3
	A	109	68.5	49.2	28.8	16.1	6.11	3.95	2.05	1.10
All data are average value										

4.3.2 Control Circuit

For the control circuit, controller, PLC, receives the environmental signals through sensors. According to the signals, controller inputs different numbers of resistors to deal with rotational speed of wind rotors which affect generated voltage. Controller keeps the voltage around 52 V by inserting or releasing the loads (resistors). The measured values (voltage, current generated power, wind velocity, wind direction and rotating speed of wind rotor) will be shown on the monitor and recorded in a USB-driver.

4.3.2.1 Sensors

Sensors are important element to know the environment (wind velocity, wind direction) and generated power (voltage, current) for the controller may have corresponding control.

Wind Velocity and Wind Direction Sensor

For calculating the wind energy passing through the wind rotors, wind velocity and wind direction are important information to know.

JNC-WS02, made by JNC Technology Co., Ltd., contents three-cup anemometer and potentiometer type weather vane. The details are shown in **Table 4.5** and **Table 4.6**.

Table 4.5 Anemometer Scalar

Measuring Theory	Three-cup Type
Range	1 ~ 96 m/s
Min. Starting Speed	0.78 m/s
Scalar	190 (D)×51 (H) mm
Weight	140 g

Table 4.6 Potentiometer Type Weather Vane

Measuring Theory	Potentiometer
Range	0 ~ 359°
Min. Starting Speed	1 m/s
Scalar	210 (L)×120 (H) mm
Weight	100 g

Voltage Sensor

To know the voltage value of generated power, voltage sensor converts high generated voltage to 4 ~ 20 mA signal for PLC to receive. Select SG7000 that is made by Gigarise tech. Co., Ltd. in this experiment. The detail of voltage sensor is listed at **Table 4.7**.

Table 4.7 Specification Description of Voltage Converter

Accuracy	±0.1% FS. (at 23 °C)
Linearity	±0.1% FS.
Response Time	0.2 sec (0-90%)
Thermo Coefficient	±0.015% FS./°C
Environment Temp.	-5 ~ +55 °C
Environment Humidity	0~90% RH
2-Wire Input with Power Supply	DC 24 ~ 28 V
Zero Point and Range Modification	±15% FS.
Insulation Impedence	≧100 MΩ with 500 VDC
Resistance Intensity	AC 1500 V/1 min.
Consummation Power	4 VA
Scalar	50 (W)×80 (H)×120 (D) mm

Current Meter

Current meter, SE4910, made by Gigarise Technology Co. Ltd., detects the generated current and sends data to PLC. Its photo is shown in **Fig. 4.13**. The detail of current meter is listed at **Table 4.8**.

Table 4.8 Specification Description of Current Meter

Accuracy	±0.25% FS.
Response Time	1 sec
Environment Temp.	0 ~ 60 °C
Environment Humidity	0 ~ 80% RH
2-Wire Input with Power Supply	DC 24 V
Insulation Impedence	≧100 MΩ with 500 VDC
Consummation Power	4 VA
Scalar	96 (W)×48 (H)×150 (D) mm

Tachometer

Tachometer, made from photo sensor, perceives rotational speed of wind rotors in this research. By employing the photo sensor as a counter, reflection boards are installed on the pulley. When the light, emitted from photo sensor, is reflected, counter will count one by one for accumulation. After a minute, we divide the accumulation with time interval, and then the rotational speed of wind rotors is obtained. The detail of photo sensor is listed at **Table 4.9** and its photo is shown in **Fig. 4.14**.

Table 4.9 Specification Description of LS-5 Photo Sensor

Distance of detecting	0.1 ~ 2 m
Environment Illuminance	Sunlight 10,000 lux; Incandescent 3,000 lux
Environment Temp.	-25 ~ 55 °C
Environment Humidity	35 ~ 85% RH
2-Wire Input with Power Supply	DC 12 ~ 24 V
Noise Resistance	1,000 V pulse/1 μs width

4.3.2.2 Controller

Utilize programmable logic controller (PLC) receiving sensors' signal to control different loadings for keeping the voltage at certain level and determine when is the time to charge battery or not.

Select the FATEC PLC FBs series controller and expended models which is made by FATEC Automation Co.. The FBs-60MA is a main controller of small-economic type PLC with 36 digital input points and 24 digital output points for I/O controlling, see **Fig. 4.15**. Download the written program for auto-control and manual-control to controller. FBs-6AD and FBs-CB5 are PLC expended models. FBs-6AD can receive analog signal with 6 channels from sensors. FBs-CB5 is an expended model of communication board for RS-485 to communicate with manual panel.

4.3.2.3 Human-computer Interface

Human-computer interface with touch panel function is used as monitor and control panel. The function of monitor shows the received data (current, voltage,

wind velocity, wind direction, etc.) on the screen. It also recorded the data into USB drive. The function of control panel let user can set different parameters to have appropriate auto-control.

Select PanelMaster PT series human-computer interface, made by Cermate Technologies Inc., the specification is listed at **Table 4.10**.

Table 4.10 Specification of PanelMaster PT Series

	Item	PT057-1/2/4/6
Display	Dimensions	5.7” (4:3)
	DPI(pixel)	640×480
	Screen Type	TFT Touch Panel Screen
	Color	64k
	Back-lighted Type	LED
	Back-lighted Brightness	20,000 hr
	Brightness (cd/m2)	250
CPU		32 Bits RISC SOC
Program Flash Memory		8 MB
Battery Backup Memory		128 MB
System Operating Memory		64 MB
Power	Input Power	DC 20 ~ 28 V
	Consumption Power	15 W
Structure	Appearance Dimensions	188.0×143.3×40.0
	Weight	0.59 kg

4.4 Operation of Experimental Apparatus

The operation of experimental apparatus is illustrated in **Fig. 4.16**. Battery A supplies power to system for controlling and sensor detecting. When the wind passes through, the system will generate the electric power. A part of generated electric power will use to charge the battery B. While the battery A is exhausted, system alternates the battery B as power supply and charge the battery A. Thus, the stand-alone system will always keep on working. At the same time, sensors record environment and generated power data for research utilizing. The detected variables (wind velocity, wind direction and rotational speed of wind rotor) are collected to become a non-dimensional parameter TSR (λ) in Eq. (4-1).

$$\lambda = \frac{R\omega}{v\cos\theta} \tag{4-1}$$

In which

λ = tip-speed ration

R = radius of wind rotor

ω = rotational speed of wind rotor

v = wind velocity

θ = included angle between wind direction and normal vector of façade of system

The other non-dimensional parameter C_p which is function of λ gives in Eq. (4-2) in experiment.

$$C_p = \frac{Generated\ Power}{\frac{1}{2}\rho A(v\cos\theta)^3} \tag{4-2}$$

Otherwise, if the wind rotors rotate too fast, system inputs resistors to slow down the wind rotors for protecting system.

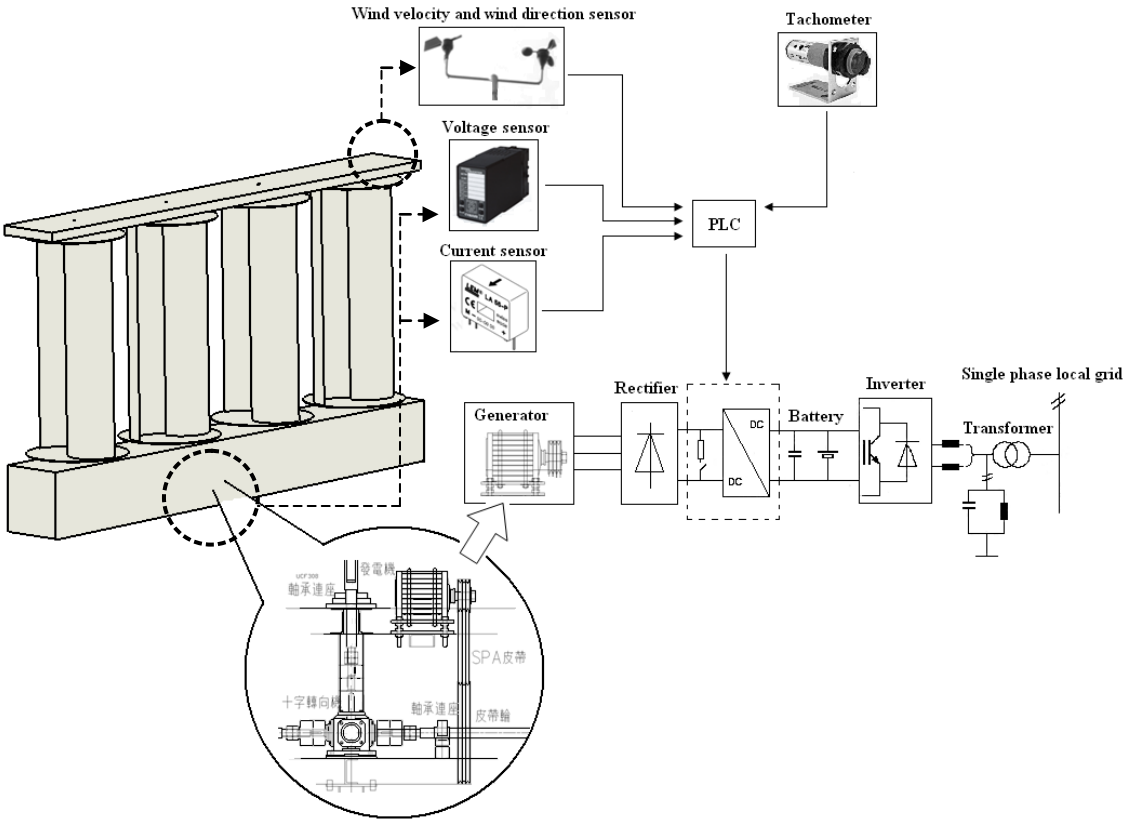

Fig. 4.1 Experiment layout

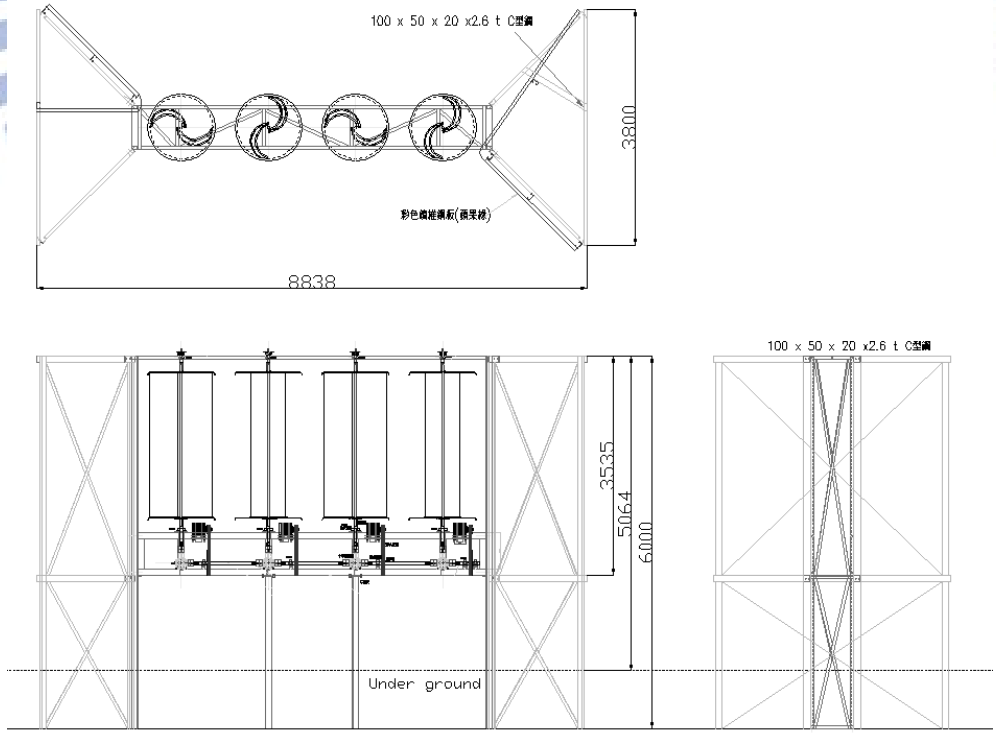

Fig. 4.2 Configuratione design diagram of parallel matrix system

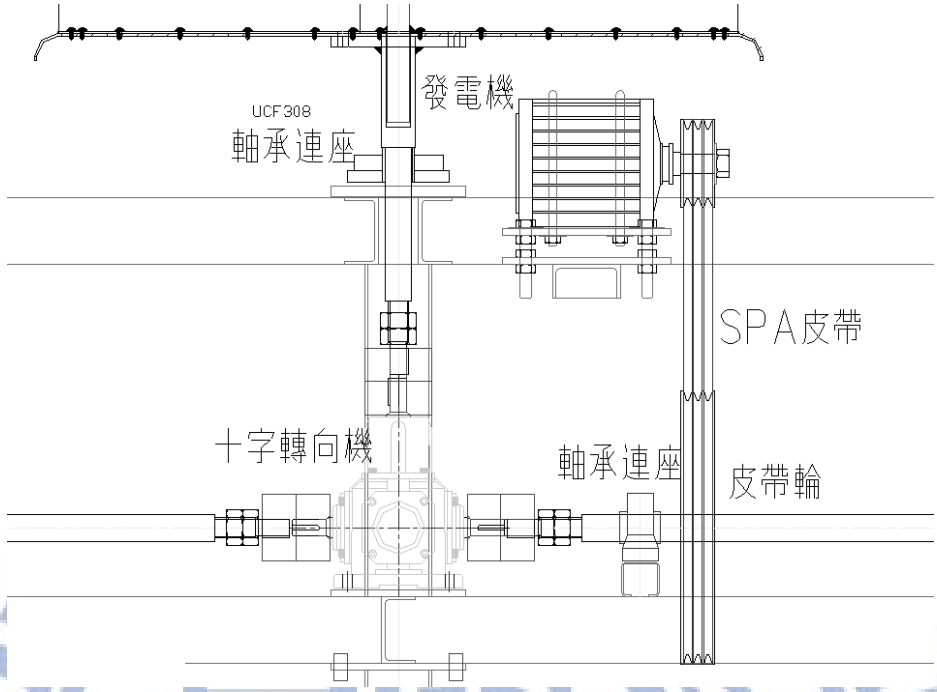

Fig. 4.3 Drive train

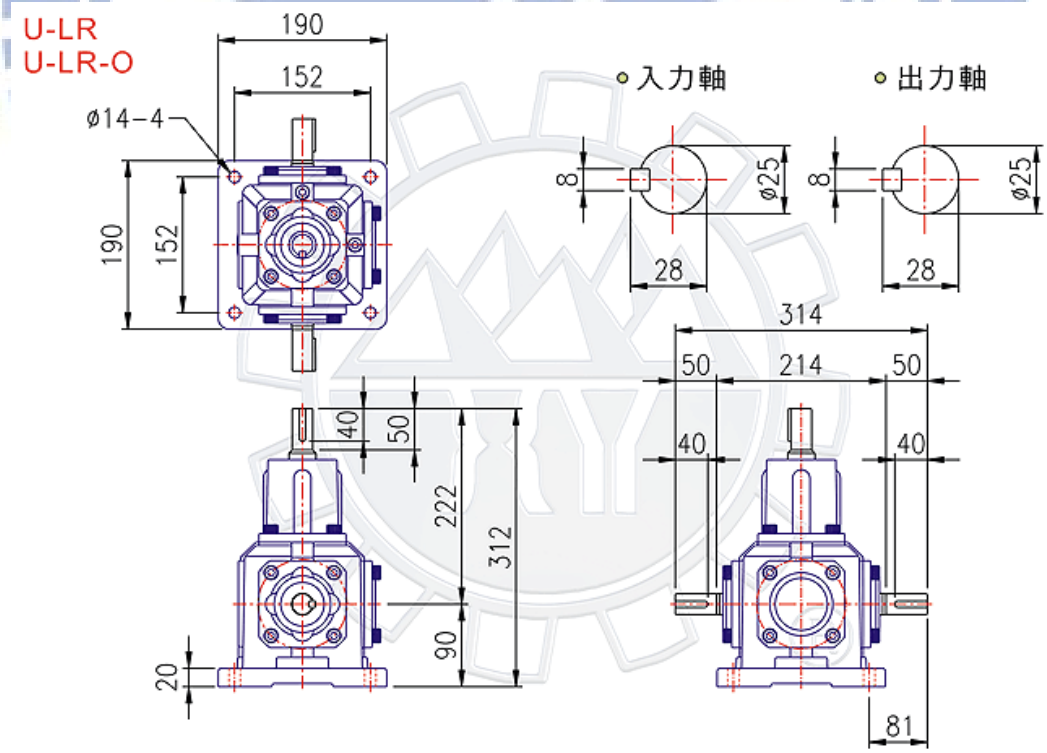

Fig. 4.4 Exterior scalar of cross-diverter [22]

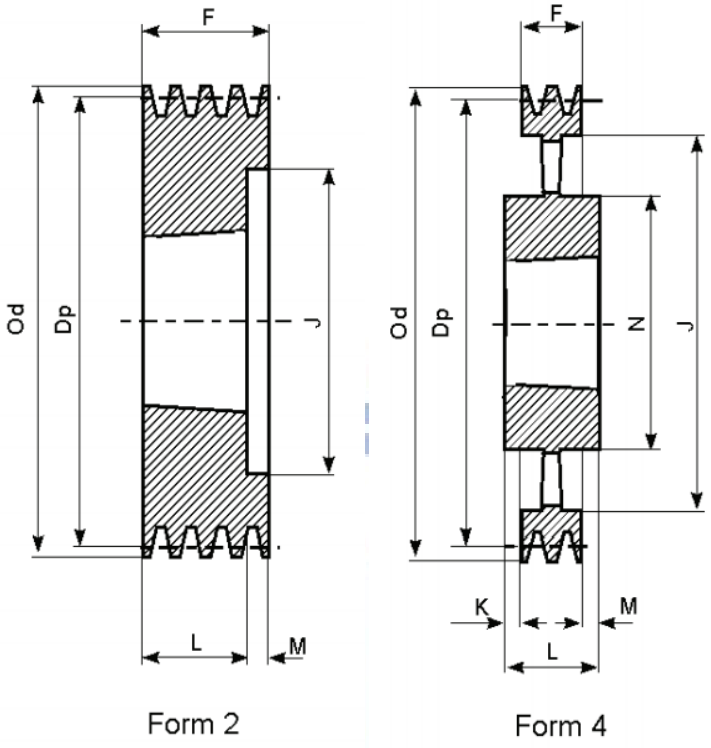

Fig. 4.5 Wedge belt pulley in form 2 and form 4

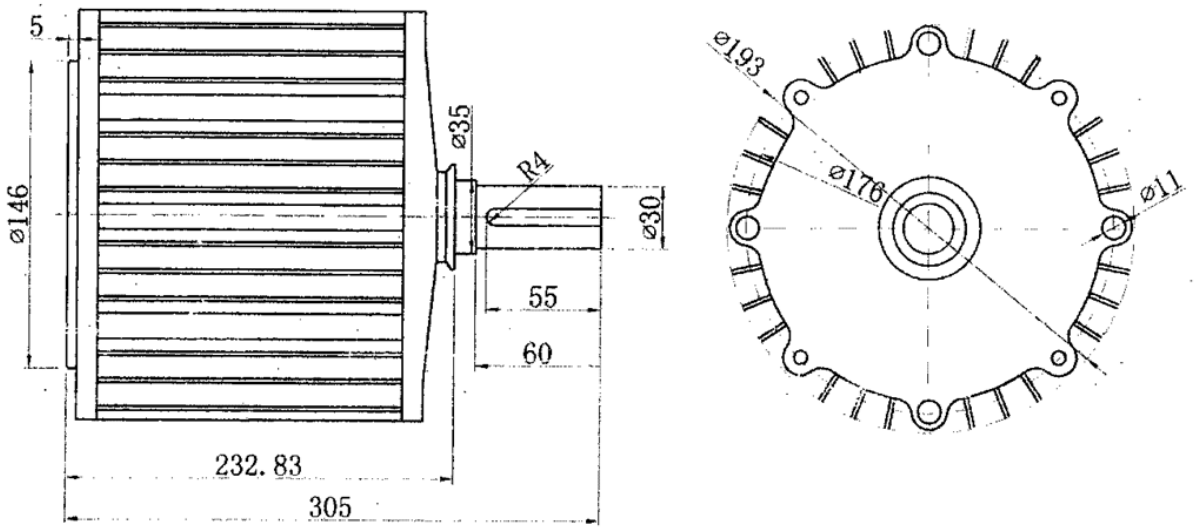

Fig. 4.6 Exterior scalar of generator

Fig. 4.7 The curtain photo

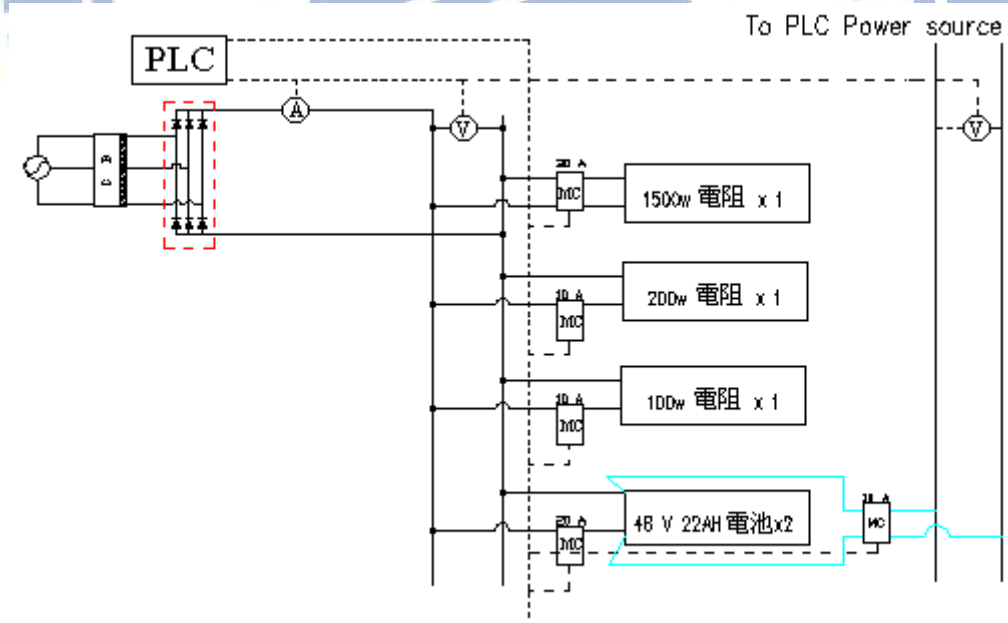

Fig. 4.8 Electrical circuit diagram

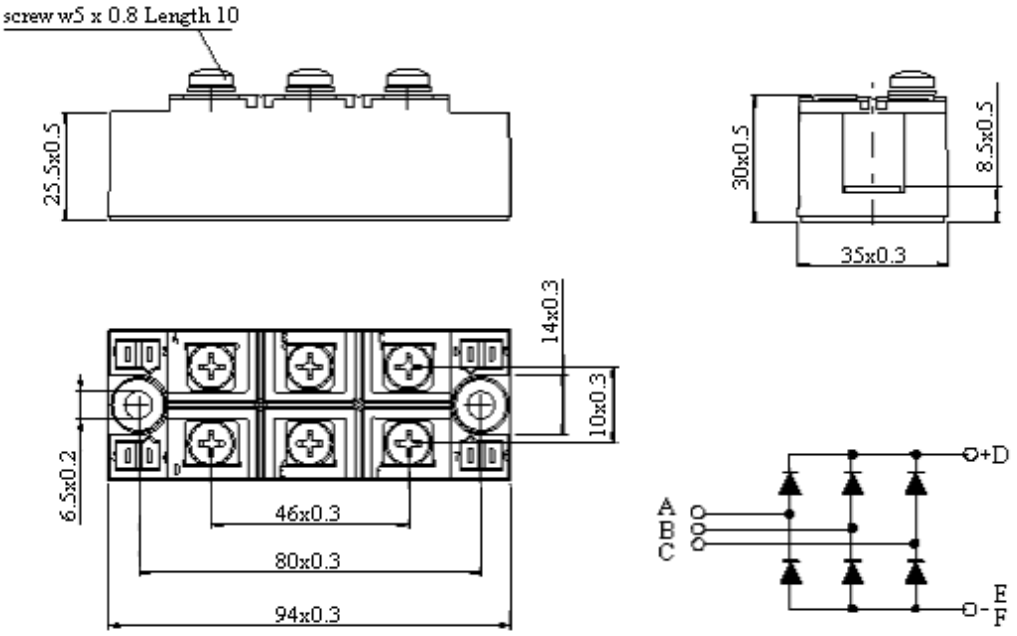

Fig. 4.9 Rectifier (all dimensions in mm)

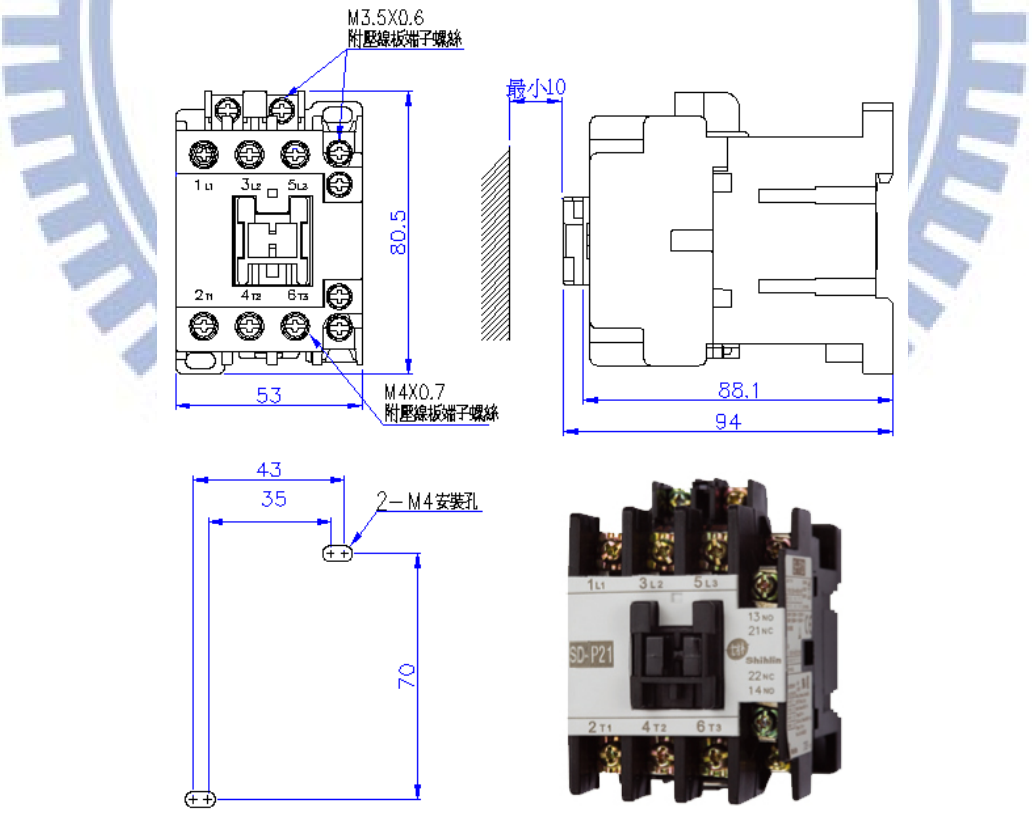

Fig. 4.10 Magnetic contactor [23]

Fig. 4.11 Power type wire wound resistor

Fig. 4.12 Battery

Fig. 4.13 Photo of SE4910

Fig. 4.14 Photo of LS-5 photo sensor

- 60 點數位 I / O 主機 （36 點 IN，24 點 OUT）

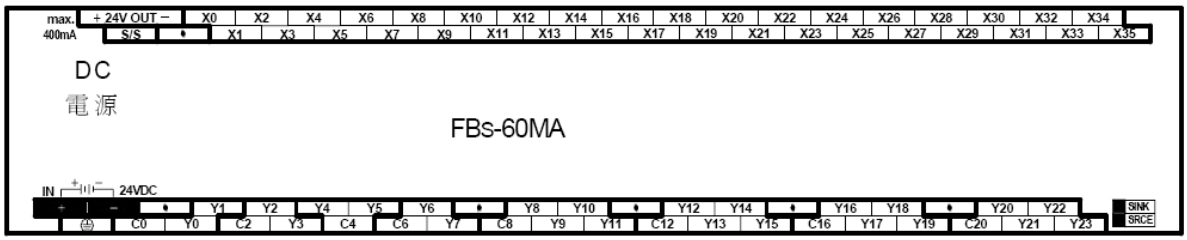

Fig. 4.15 FBs-60MA PLC diagram

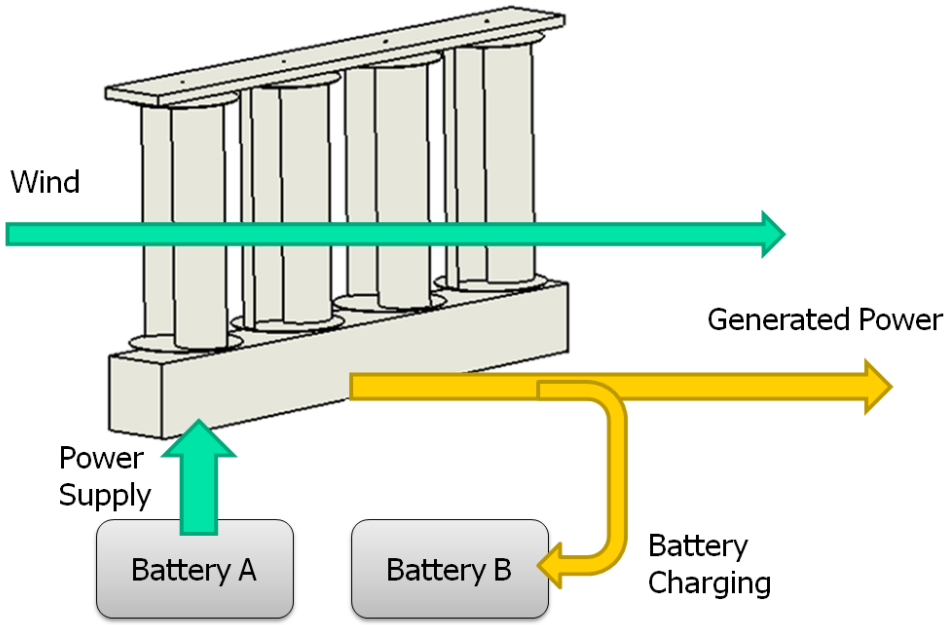

(a)

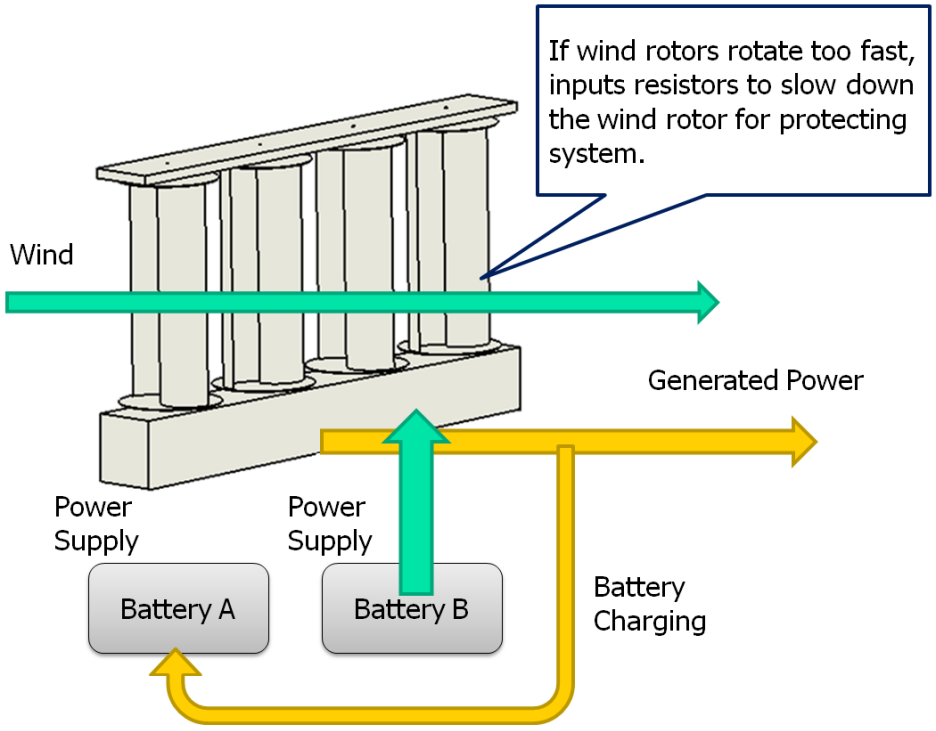

(b)

Fig. 4.16 Operation of experimental apparatus

CHAPTER 5

RESULTS AND DISCUSSION

As mentioned in the research flow chart shown in **Fig. 1.7**, this study is divided into two parts. The first part is the numerical investigations, which are demonstrated in **Section 5.1**. In this part, it can be further separated in three sections: a single wind rotor and the parallel matrix systems with and without curtain. The simulation results exhibit the performance wind rotor system and the resultant flow fields. The second part is a series of experiments, demonstrated in **Section 5.2**. In this part, the experiments can be separated in two cases that are with or without curtain. For these cases, wind speed, wind direction, rotational speed of wind rotor and generated power are measured to evaluate the performance of wind rotor. Finally, **Section 5.3** makes the comparisons with the differences between the simulation and experiment results.

5.1 Simulation Results

This topic consists of three segments, a single Savonius wind rotor, four Savonius wind rotors in parallel matrix systems with or without curtain. These models were sketched in **Figs. 3.2**, **3.3** and **3.4**, respectively. The corresponding geometry of wind rotor was illustrated in **Fig. 3.1**, whose information, such as the configuration data of the wind rotor and dimensions of simulation domain were summarized in **Tables 3.1** and **3.2**.

5.1.1 A single Savonius Wind Rotor

The simulation for present case is adopted as a reference for later comparisons. It simulates the experimental work by Blackwell et al. [6], who

investigated the performances of fifteen configurations of Savonius wind rotors tested in a low speed wind tunnel. The Savonius wind rotor, with a predetermined load provided by an air motor, was allowed to rotate in a steady wind speed 7 m/s. When a steady rotation was achieved, the measured data were taken. After that, the load was changed slightly, causing a new rotational speed to get another set of data. By repeating these steps, the relationships between C_p and tip-speed ratios (TSRs) in fixed wind speed were plotted. The experimental results in a wind speed of 7 m/s are shown in **Fig. 5.1**. However, in simulations, the turbine load is not considered, so the free spinning wind rotor cannot be fully simulated. The method used in simulations is to specify constant rotational speeds and change the parameters to reveal freely moving wind rotor blades in experiments. The comparison between the predicted results and experimental measurements is given later.

To compare with Feng's predictions [3] and experimental measurements by Howell et al. [14], the 3-D simulations are carried out with a specified wind speed of 7 m/s. This model in the present case uses a grid number of 657,400 (see **Table 3.5**) in the simulation domain of 26 (L)×12 (W)×6.34 (H) m. The parametric study is based on the variation of TSR ranged from 0.4 to 1.2, which are 0.4, 0.6, 0.8, 1.0 and 1.2, respectively. The simulated C_p results as a function of TSR for one single Savonius wind rotor are shown in **Fig. 5.2**, which Feng's predictions [3] and Howell et al.'s measurements [14] are also included. The maximum values of C_p are 0.189 at TSR 0.8 in present study, 0.222 at TSR 0.75 in Feng's simulation [3], and 0.241 at TSR 0.86 in experiment by Howell et al. [14], respectively. In general, **Figure 5.2** exhibits the maximum value of C_p occurring in the neighborhood of 0.8. Therefore, the case of TSR = 0.8 in this study is selected to analyze intensively.

To observe the flow field, α is firstly defined as the angle of rotating wind blade relative to the initial angle, illustrated graphically in **Fig. 5.3**. The resultant torque curves of one single Savonius wind rotor under different TSRs (0.4 ~ 1.2) in a rotation (360°) are shown in **Fig. 5.4**. Among them, **Figure 5.4 (c)** is the one for TSR = 0.8, which has the best performance (maximal C_p). As shown in this figure, the maximal torque happens at α = 110° and the minimal one at α = 20°. The corresponding static pressure fields and velocity vector distributions around the single Savonius wind rotor at these two positions are demonstrated in **Figs. 5.5** and **5.6**, respectively.

From these two figures, concerning on the pressure difference between the front and back sides of the returning blade, it reveals that the one at α = 20° is apparently higher than that at α = 110°. It also can be seen that a large vortex is generated around the tip at the low-pressure region behind the blade as shown in **Figure 5.5 (a)**. This effect would produce a negative torque and thus causes a lower net torque. On the other hand, at α = 110° in **Figure 5.5 (b)**, the pressure difference is smaller, and the resulted vortices are also smaller. Therefore, the negative torque is reduced, resulting in a higher net torque. Such phenomenon is typical characteristics of drag device, which has high starting torque but low C_p (see **Section 2.2.2.1**).

The simulation results of C_p in this study are lower than other two researches (Feng [3] and Howell et al. [14]). The crucial reason is due to geometry of wind rotor blade. The blade, whose shape can be referred to **Figure 3.1**, in this study, generates more vortices that let C_p become lower. However, this kind of blade geometry, framed by two slices of iron plate with vesicant material as stuff in between, is needed to withstand variable environment. On the other hand, the blade used by Feng [3] and Howell et al. [14] does not

consider the thickness effect.

5.1.2 Four Two-bladed Savonius Wind Rotors in Parallel Matrix System without Curtain

Last year, Feng [3] numerically studied a parallel matrix system, which includes three Savonius wind rotors with the same angular speed, the specified phase angle and the fixed distance. He found that such disposition can cause constructive interference that improves performance of wind rotor and the best performance occurs at the phase angle difference equal to 90° (**Table 5.1**). These conclusions can be supported by the numerical simulation of Shigetomi et al. [10], illustrated in **Fig. 5.7**. Therefore, the phase angle difference of 90° is adopted by the present simulation.

Table 5.1 Comparisons of the Maximums of C_p for Three-rotor in Different Phase Angle [3]

Wind Speed (m/s)	Phase Angle Difference (degree)	Maximum of C_p
7	0	0.435
	45	0.466
	90	0.479
	135	0.419

This model in the present case uses a grid number of 1,827,520 (see **Table 3.5**) in the simulation domain of 26 (L)×16.2 (W)×6.34 (H) m. The distance between two wind rotors is 1.4 m. Note that the parameters, which do not mention in the present case, are completely the same as the ones used in the last

section.

Comparing to the simulation results in last section, the resultant torque curve of four Savonius wind rotors in parallel matrix system without curtain at wind speed 7 m/s and TSR 0.8 (where the maximum C_p occurred in one single rotor simulation) in a rotation (360°) is shown in **Fig. 5.8**. For easy to demonstrate the effect of parallel matrix system, each wind rotor is assigned a number, as marked in **Fig. 5.9**.

In **Figure 5.8**, it can be seen that for rotors No.1 to 3, each has higher performance than one single rotor. On the other hand, rotor No.4 has lower performance than one single rotor. The four wind rotors rotate in the same direction (counterclockwise). The wind departed from rotor No.4 enhances the rotation of No. 3, and so on. When the wind passes through the wind rotor, it causes a low pressure that contributes extra rotation power to adjacent wind rotor. However, there is no wind rotor to enhance the rotation of No.4. The static pressure field and velocity vector distribution around parallel matrix system are demonstrated in **Figs. 5.9** and **5.10**, respectively. For the purpose to analyze flow field more clearly, **Fig. 5.11** shows the streamline distribution derived from 2-D simulation, which has same parameters with present case. The difference between each adjacent stream functions represents the volume flow rate. Therefore, the thinner streamlines has higher velocity and wider streamlines has lower velocity. The higher velocity indicates that wind passes through the wind rotor easily. On the other hand, the lower velocity indicates the wind rotor to be able to absorb more wind work that lets the velocity goes down. Thus, wind rotors produce an asymmetrical flow field that the dense streamlines take place around wind rotor with lower torque; wider streamlines around wind rotor with higher torque.

For this case, the maximum value of C_p is 0.262 at TSR 0.8, given in **Fig. 5.12**. It also reveals that parallel matrix system apparently has higher performance than one single rotor.

5.1.3 Parallel Matrix System with Curtain

The present case is completely the same as the one in the last section, except the addition of 4 curtains as shown in **Fig. 5.13**. This model in the present case uses a grid number of 2,980,600 (see **Table 3.5**) in the simulation domain of 26.9 (L)×21.4 (W)×6.34 (H) m.

In **Figure 5.12**, the maximum C_p value is 0.270 for system with curtain and 0.262 for system without curtain that the discrepancy is small and both of them happen at TSR 0.8. However, the C_p values are nearly the same as TSR greater than 0.8. On the other hand, the largest difference of C_p happens at TSR 0.6, and it is 1.159 times higher than the system without curtain. The resultant torque curves of four Savonius wind rotors at TSR 0.6 in parallel matrix system with and without curtain in a rotation (360°) are shown in **Fig. 5.14**. In **Figure 5.14**, all of the rotors in system with curtain have higher performance (torque value) than those in system without curtain. The existence of curtain makes wind velocity speed up for incompressible flow. The higher wind velocity causes system has higher performance. The corresponding velocity vector distribution is demonstrated in **Fig. 5.15**. However, the results at TSR 0.8 in **Fig. 5.16** reveal that rotor No.1 (see **Figure 5.16 (a)**) has no apparent difference. Moreover, torque of rotor No.4, given in **Figure 5.16 (d),** is lower than the one in the system without curtain. In this case, only rotor No. 2 and 3 in system with curtain perform higher torque value than those in system without curtain (see **Figures 5.16 (b)** and **(c)**). The reason is that the rotational speed of wind rotors

in high TSR is closed to the speed up wind velocity that wind work on rotors much less than the situation of wind rotor in low TSR.

5.2 Experimental Results

The experimental apparatus is built up based on the simulation results from **Sections 5.1.2** and **5.1.3**. Its entity, shown in **Fig. 5.17**, is set up at Ln. 756, Zhongzheng W. Rd., Zhubei City, Hsinchu County, Taiwan, and the system layout was shown in **Fig. 4.1**. It is an open-field experiment that exist lots of variables so we need many sensors to know the information of environment which is already demonstrated in **Chapter 4**. A series of experiments were conducted in two cases, the effect of curtain and effect of battery. According to those experiments, the quantity of generated electricity as function of time is exhibited to show its power generating condition.

5.2.1 Wind Speed and Wind Direction

The wind speed and direction in environment were measured during the experiments proceeding. As shown in **Fig. 5.18**, the wind velocity and wind direction change significantly in the open field. In this unstable situation, starting torque plays an important role in power generation; therefore, the Savonius wind rotors with great starting torque are used in this situation, as discussed in **Section 2.2.2.1**. Even though the significant variation, wind direction still has its own regulation, called monsoon, in which the south wind blows in summer and the north wind blows in winter. Because of the monsoon, the parallel matrix system is oriented in south-north direction agreed with the wind so that the wind rotors can always face it. Thus, the angle of wind direction will not vary too much.

Nevertheless, the wind direction has about 30° deviation to the facade of the parallel matrix system, which is shown in **Figure 5.18 (b)**.

5.2.2 Effect of Curtain

The same as the fore-mentioned, the flow in open field has significant variation. Among these variations, wind velocity and wind direction are variables that we cannot control. Besides, hysteresis happens in data recording, meaning that the information data not only depends on its current environment but also on its past one. When the wind speed goes up, the rotational speed of wind rotors are not kept the pace yet. On the other hand, inertia keeps the speed of wind rotors while wind speed descends. This phenomenon happens especially at TSR higher than 1.0. Therefore, we discuss the experimental results below TSR 1.0.

The results system with and without curtain are shown in **Figs. 5.19** and **5.20**. In figures each point is one measuring point and the red line inside is its trend line. For easy to analyze those data, round off the TSR of data points and calculate average value and standard deviation (see **Fig. 5.21**). The error bar in figure is one standard deviation. In **Figure 5.21** shows that performance of system with curtain is apparently higher than system without curtain during TSR 0.7 to 1.0. The maximum difference is 58% which happened at TSR 1.0 and the average difference from TSR 0.7 to 1.0 is 34%. However, the simulation results (see **Figure 5.12**) shows that the difference mostly occurred in low TSR but no difference in these experiment. The main reason is that the battery connects at second side of circuit generates about 50 V energy gap. While the generated power is lower than 50 V, no current will be generated. Only when the generated power is higher than 50 V, we can get current. On the other word, the generated

power was “eaten” by battery. Therefore, we withdraw the battery from second side of circuit to confirm this phenomenon. **Figs. 5.22** and **5.23** show the results of system with and without curtain which withdraws battery. We arranged **Figures 5.22** and **5.23** to receive **Fig. 5.24**. In figure, the effect of curtain appears in low TSR, and its average difference is 19% from TSR 0.2 to 0.9. Consequently, curtain indeed enhances the performance of system but the effect of battery needs to be conquered.

5.2.3 Effect of battery

According to fore-mentioned that the battery connects at second side of circuit generates about 50 V energy gap which cause no current while generated power is lower, we consider that whether performance of system can be improved by withdraw the battery from second side of circuit. **Fig. 5.25** and **Fig. 5.26** show the comparison between system with and without battery. In **Figure 5.25**, system with curtain reveals that the variation of system without battery is bigger than system with battery. System without battery from TSR 0.9 to 1.0 almost no change but 80% difference from TSR 1.0 to 1.1. On the other hand, **Figure 5.26**, system without curtain, also shows that variation of system without battery is bigger than system with battery. The C_p of system without battery suddenly rises up at TSR 1.0. Even though the performance is so unstable in system without battery, we did not observe that system without battery has higher performance. Consequently, withdrawing battery from second side of circuit not only cause fluctuation of performance but also no use in improving performance. In these experiment results, we can realize that battery has a function to stable electric energy.

5.2.4 Power Generating Efficiency

After series of experiment, we accumulate recording data for two hours in four kinds of cases to receive average power generating efficiency of system which is listed at **Table 5.2**.

Table 5.2 Power Generating Efficiency

	Electric Energy (kJ)	Wind Energy (kJ)	Power Generating Efficiency
Curtain and Battery	99.5	851.8	11.7%
Curtain and No Battery	96.1	890.2	10.8%
Battery and No Curtain	101.7	1009.0	10.1%
No Curtain and No Battery	65.6	653.7	10.0%

These calculations are according to Eq. (5-1).

$$Power\ Generating\ Efficiency = \frac{Electric\ Energy}{Wind\ Energy} = \frac{\int_{t_1}^{t_2}(Generated\ Power)dt}{\int_{t_1}^{t_2}\rho A(v\cos\theta)^3 dt} \approx \frac{P_g}{P_W} = C_p \qquad (5\text{-}1)$$

where t_2 - t_1 is 2 hr.

Table 5.2 shows that the power generating efficiency of system with curtain is slightly higher than system without curtain. As the experimental results that curtain can enhance performance of system. The two hours power generating record is illustrated in **Fig. 5.27**. In figure, generated power is not a

fix value but rise and fall with time. The orange part is generated electric energy.

If wind velocity is unstable 7 m/s, system can generate 5.3 kw·hr a day in power generating efficiency 10%. This electric energy can supply four refrigerators usage. Conversion of electric energy into money is 39 NT dollars for wind power capacity less than 10 kW is 7.3562 NT dollars per kw·hr.

5.3 Comparison between Simulation and Experimental Results

The results of parallel matrix system with curtain are shown in **Fig. 5.28**, which summarizes experiment and simulation results. In low TSR, simulation has large difference to experiment. The difference is due to the expression of C_p. The numerator of C_p in simulation is $T \cdot \omega$ but generated power in experiment. Between these two numerators are two significant losses, which are the mechanic loss and power generation loss. According to **Table 5.3** [24] and the datasheet in **Chapter 4**, mechanical efficiency will be 0.89 = 0.95 (Cross-diverter)×0.95 (V-belt)×0.99 (Ball bearings). Furthermore, Spooner and Williamson [25] studied the efficiency of permanent magnet generator that power generating efficiency is among 0.90 to 0.95. We select 0.90 as power generating efficiency for the strict conditions. As a consequence, the energy transform efficiency of parallel matrix system will be 0.80.

Table 5.3 Mechanical Efficiencies [24]

Machine Elements	Efficiency	
	High	Low
Ball Bearings	0.999	0.99
Silent Chain	0.99	0.97
Spur and Helical Gears (Include Bearings)	0.985	-
Roller Bearings	0.98	-
Synchronous Belt	0.98	-
Bevel Gears	0.98	0.97
V-blet	0.98	0.95
Roller Chain	0.97	0.95
Worm Gears	0.97	0.50
Ball Bearing Screws	0.93	0.90
Power-on Pin (Multiple Threads to Single Thread)	0.84	0.38
Roller Screw	0.80	-
Screw Connections	0.38	0

In **Figure 5.28**, the energy transform efficiency is different at diverse TSR which are list in **Table 5.4**. This table shows that energy transform efficiency is related to its rotational speed of wind rotor. Therefore, energy transform efficiency has large difference to theoretical value 0.8 at TSR 0.4 and 0.6, but it is 0.7 at TSR 0.8 which is more close to theoretical value.

Table 5.4 Energy Transform Efficiency

TSR	C_p of Simulation	C_p of Experiment	Energy Transform Efficiency
0.4	0.05	0.19	27%
0.6	0.10	0.26	37%
0.8	0.19	0.27	70%

In high TSR, the tendency of curve line between simulation and experiment is different. The reason is that rotational speed of wind rotor and inlet wind velocity is a fixed value which is given by user in simulation. Therefore, because of wind rotors rotate too fast that wind easily passes through wind rotors, C_p goes down for wind did not work on wind rotors fully. Contrary, wind rotors rely on wind working on rotor's blades. When wind velocity goes down, rotational speed of wind rotor also goes down for there is no energy to keep rotational speed staying in a certain value so long. Consequently, the situation of simulation in high TSR will not happen in experiment that cause tendency of curve line different.

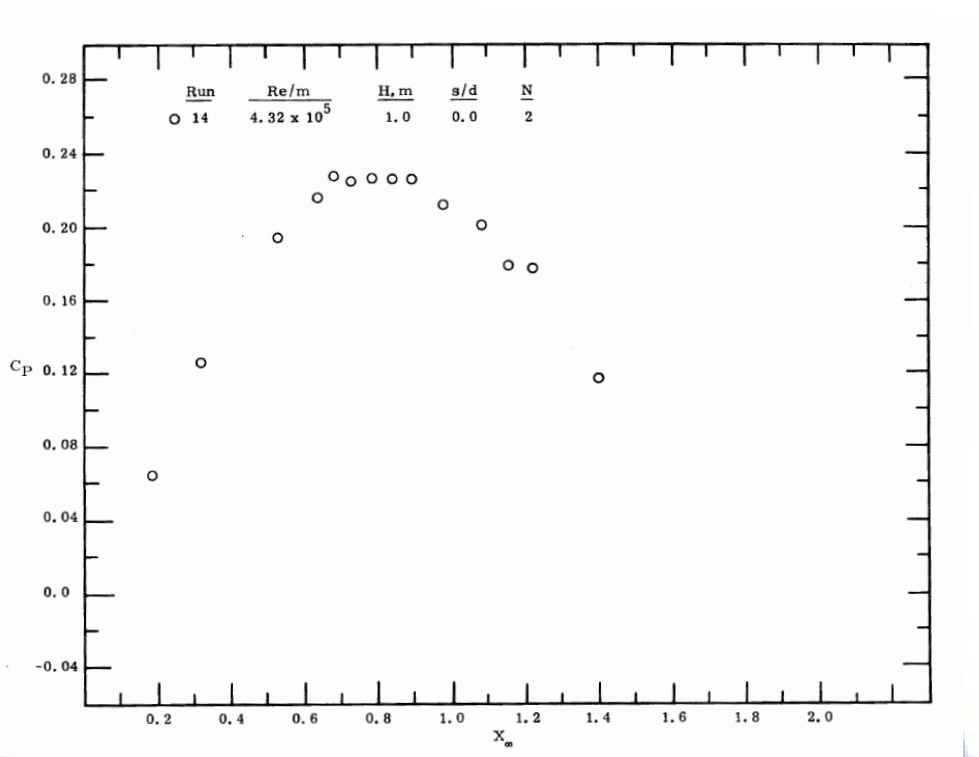

Fig. 5.1 The experimental results of a single Savonius wind rotor inside the wind tunnel [6]

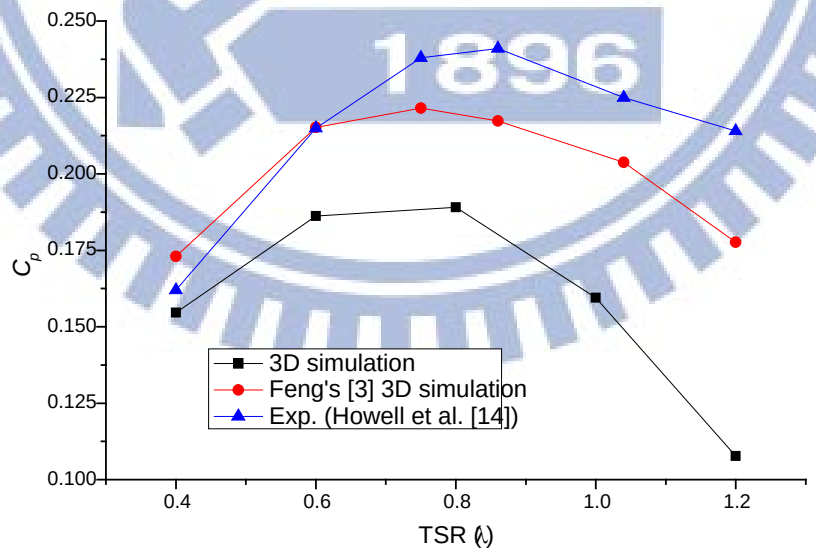

Fig. 5.2 The simulation of single Savonius wind rotor comparing with Feng's [3] simulation and experimental data [14]

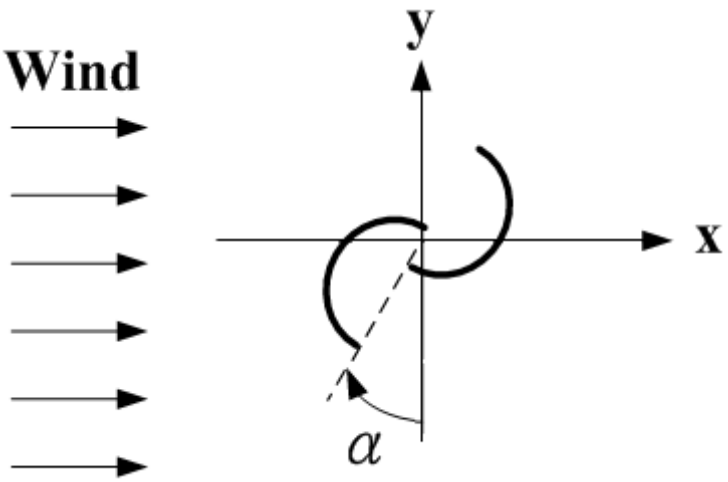

Fig. 5.3 The defined angle α of rotating wind blade relative to the initial angle

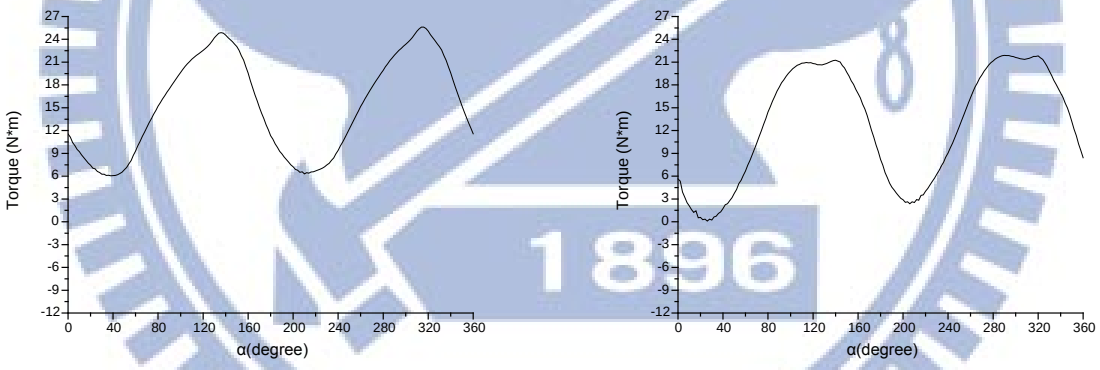

(a) **(b)**

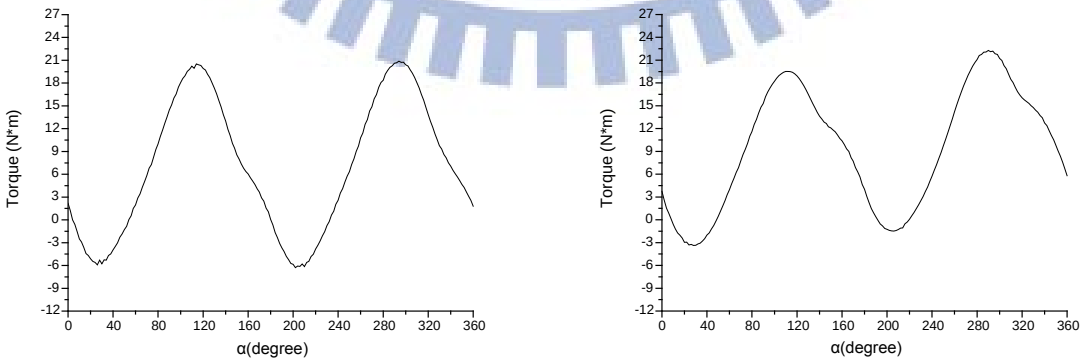

(c) **(d)**

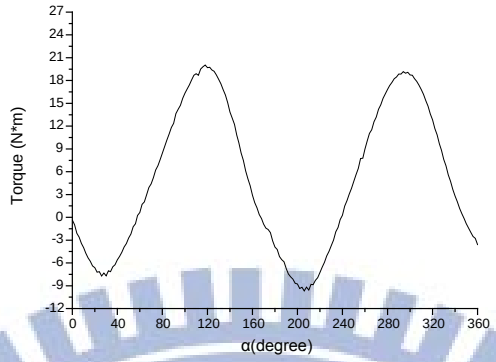

(e)

Fig. 5.4 Torque curves of one single Savonius wind rotor with wind speed 7 m/s under different TSR: (a) 0.4; (b) 0.6; (c) 0.8; (d) 1.0; (e) 1.2

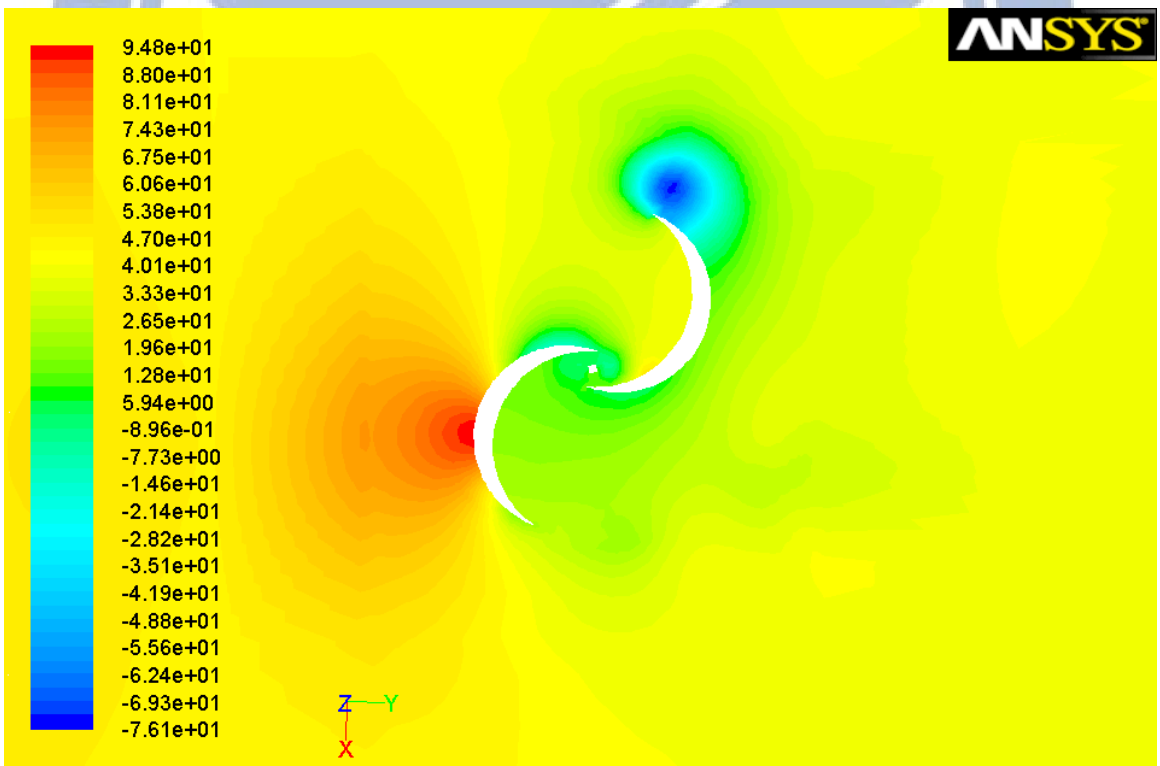

(a)

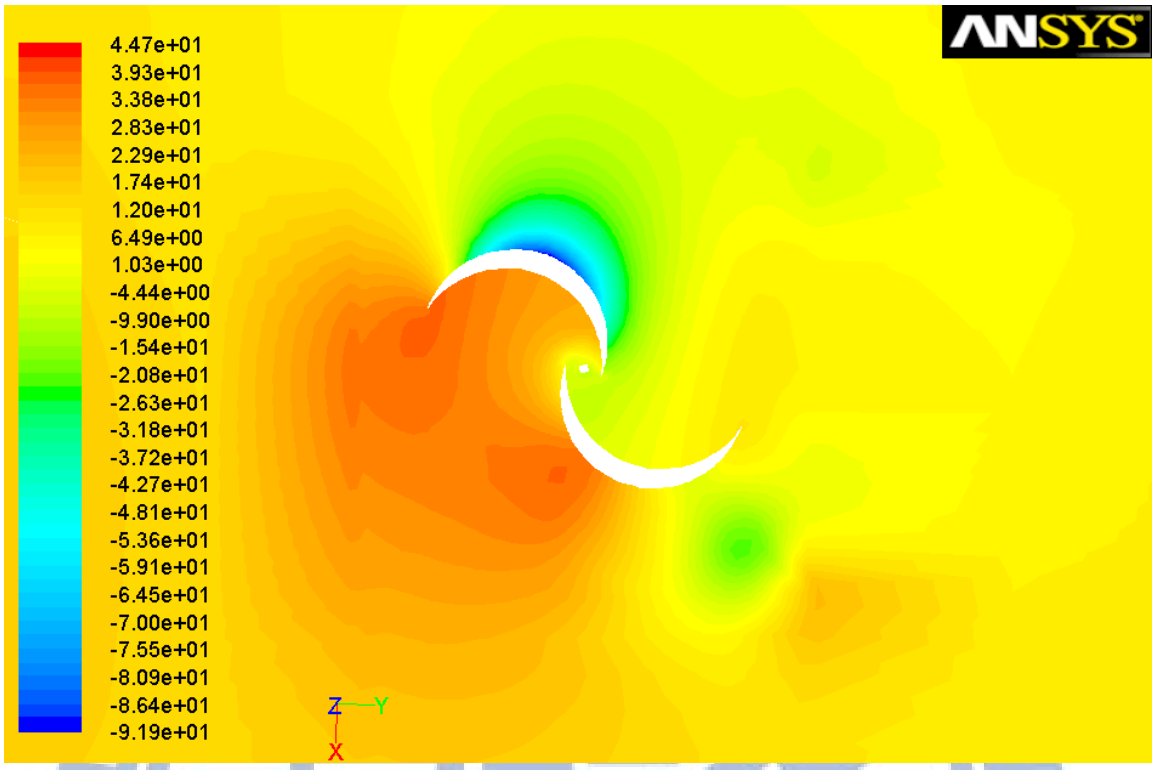

(b)

Fig. 5.5 Static pressure field around one single Savonius wind rotor: (a) α=20°; (b) α=110°

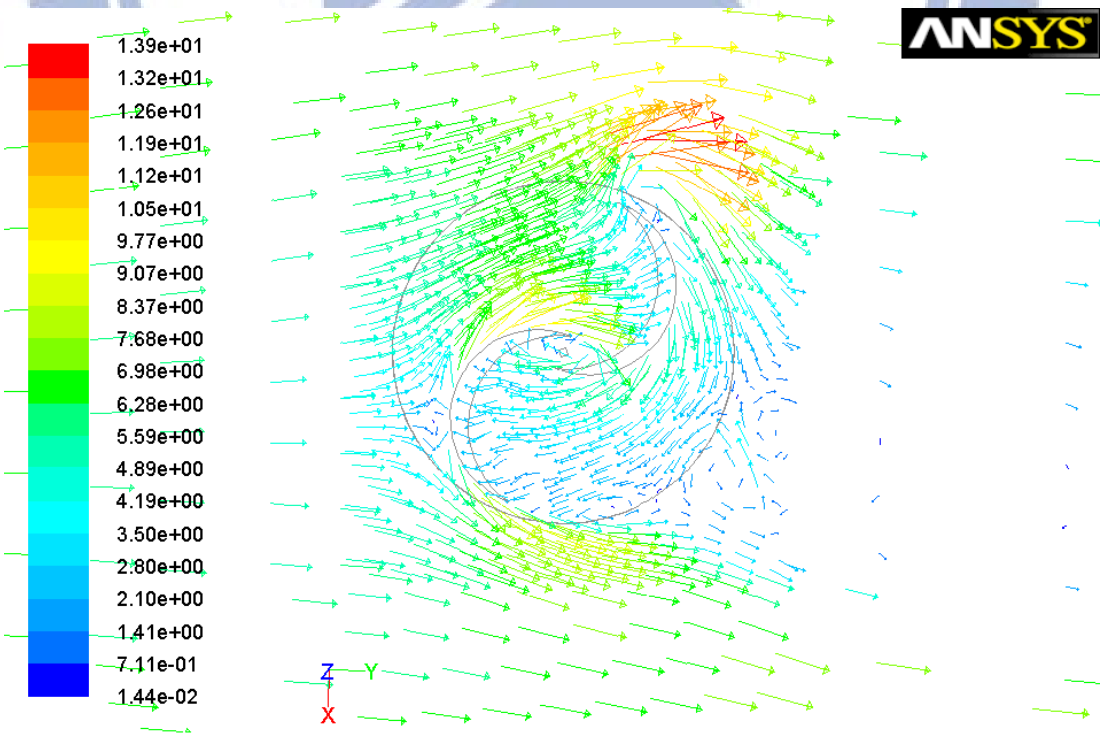

(a)

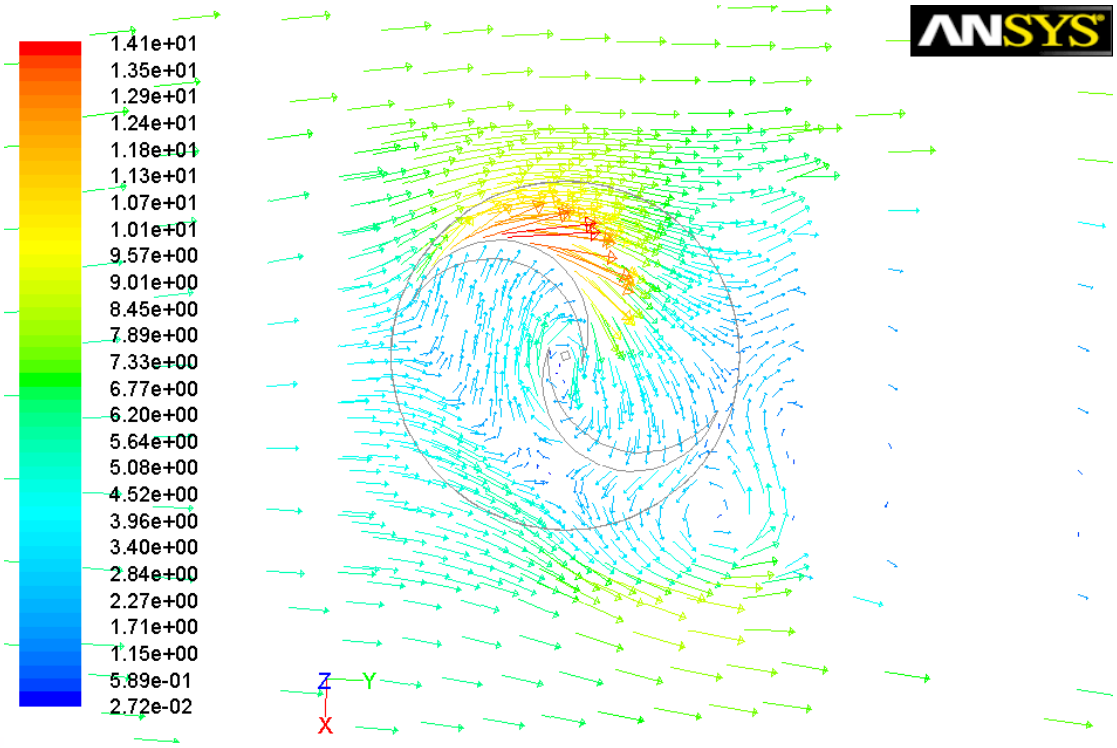

(b)

Fig. 5.6 Velocity vector distribution around one single Savonius wind rotor: (a) α=20°; (b) α=110°

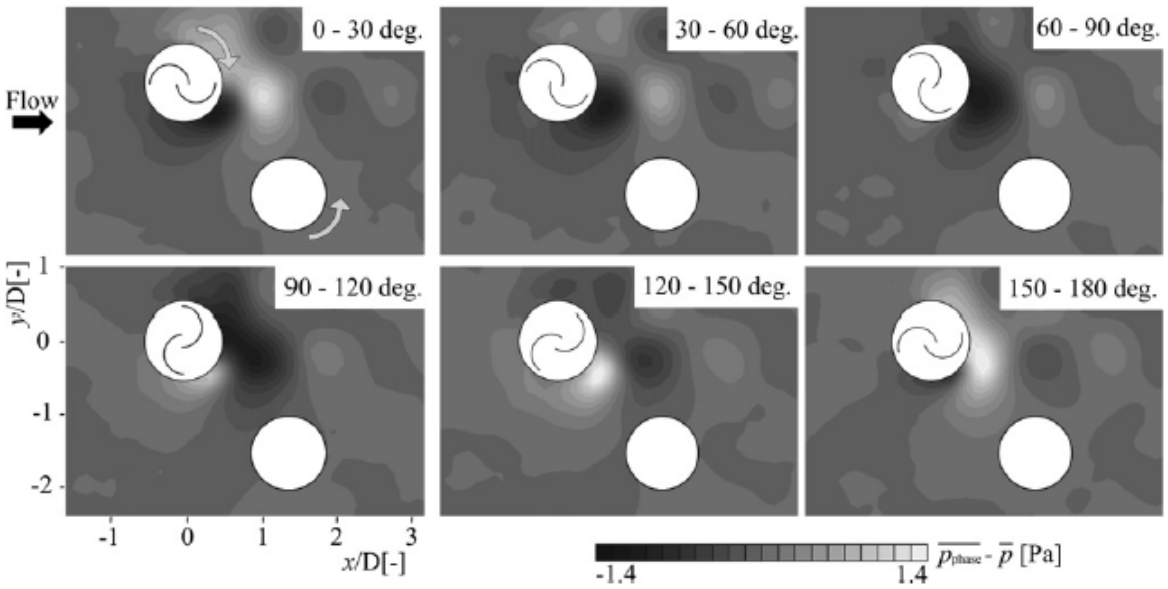

Fig. 5.7 Phase-averaged pressure difference from the average pressure field [10]

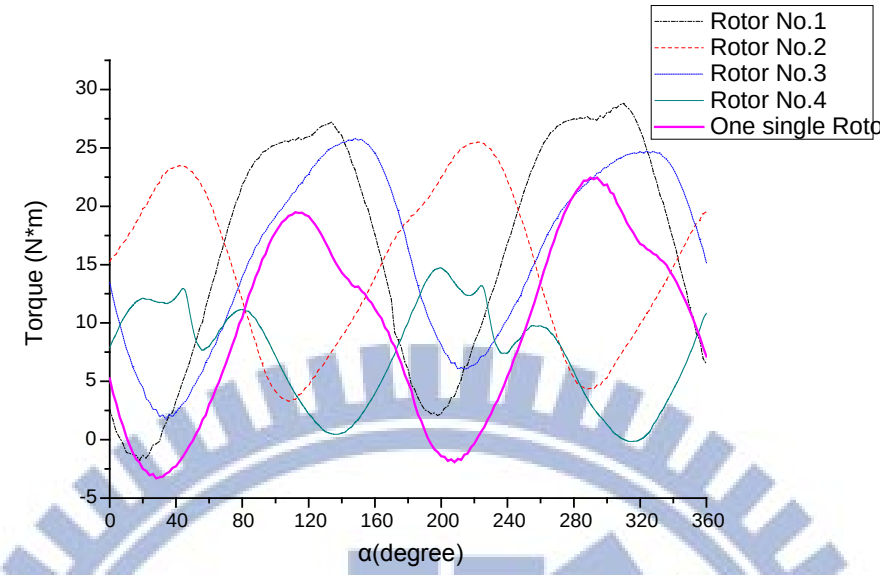

Fig. 5.8 Torque curves of system without curtain and one single rotor at TSR 0.8

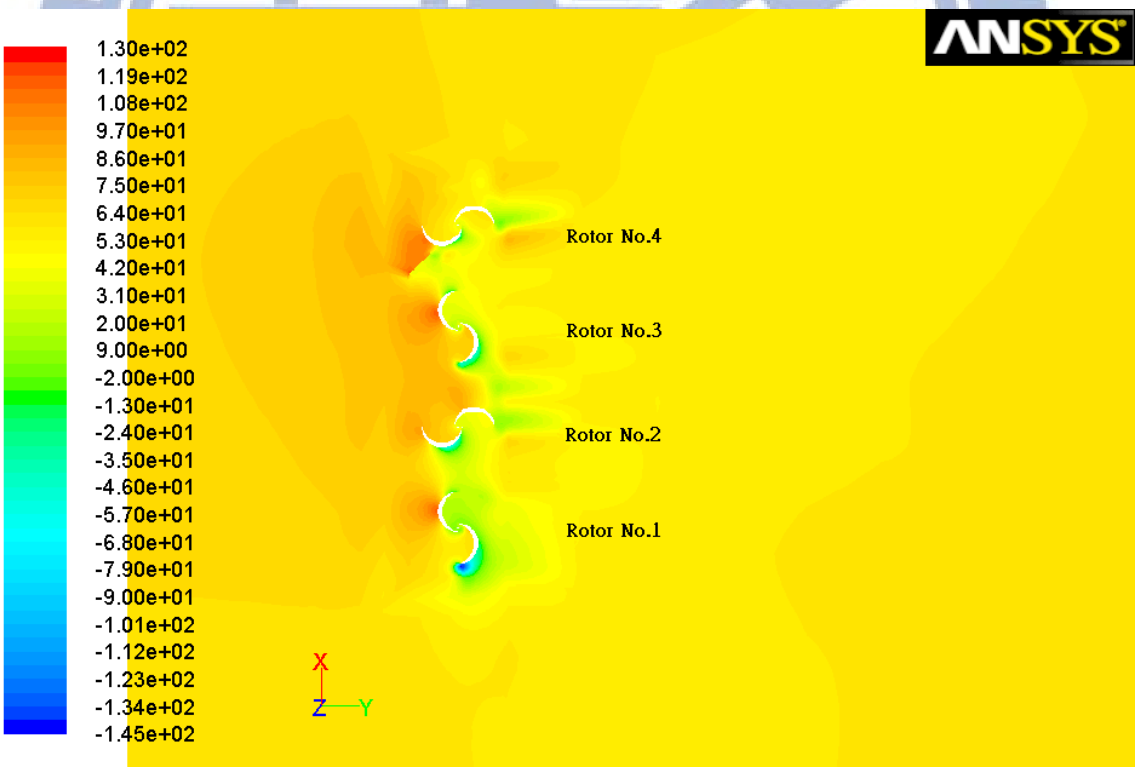

Fig. 5.9 Static pressure field around system without curtain

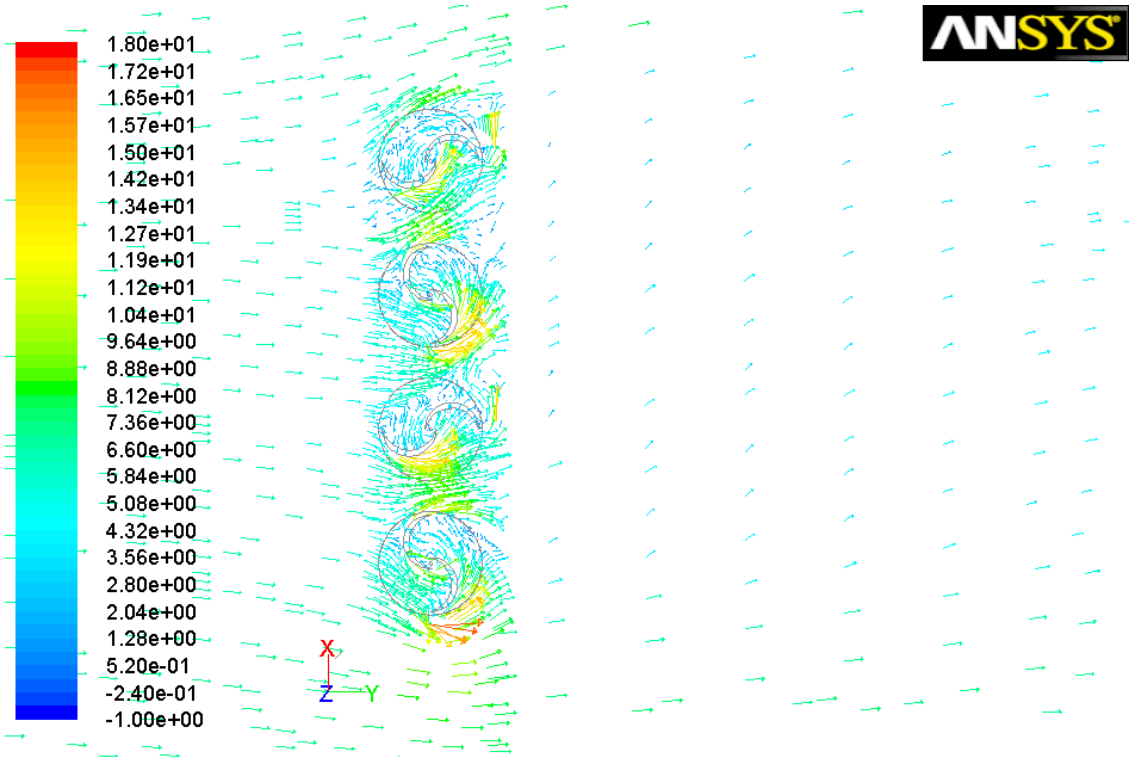

Fig. 5.10 Velocity vector distribution around system without curtain

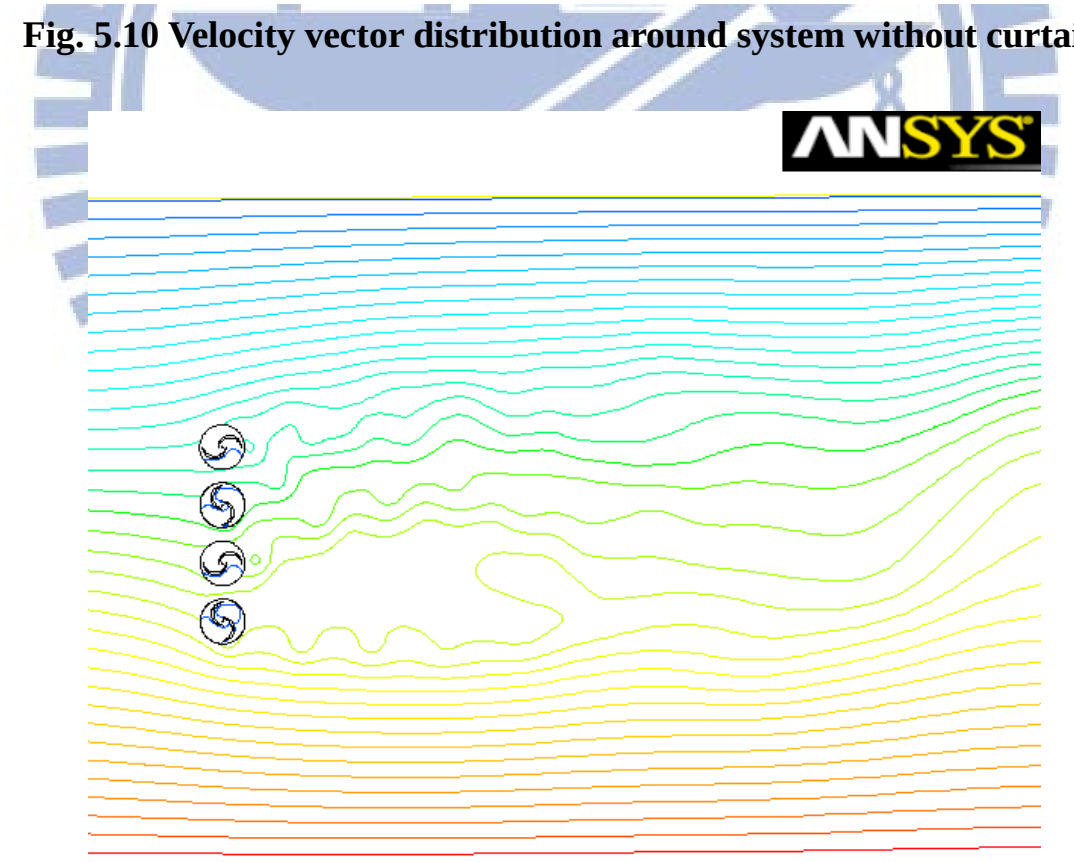

Fig. 5.11 Streamlines around system without curtain at wind speed 7 m/s and TSR 0.8

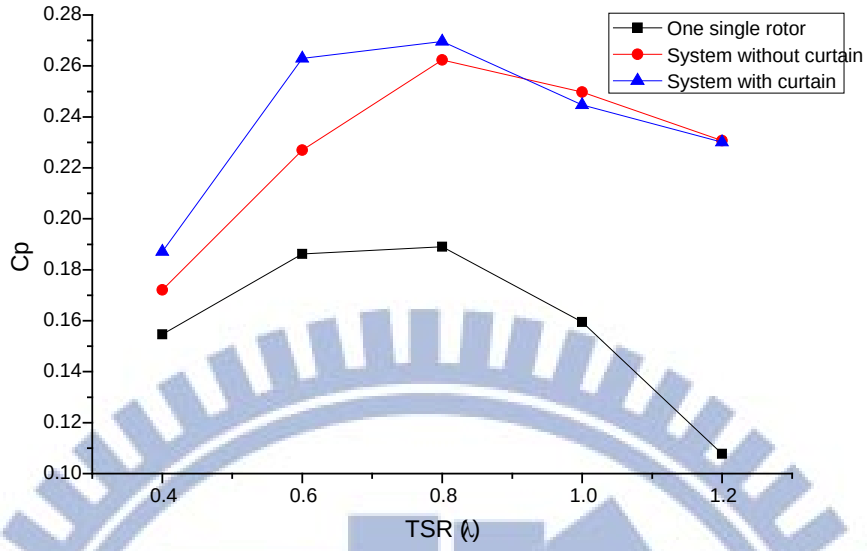

Fig. 5.12 Comparison of simulation results

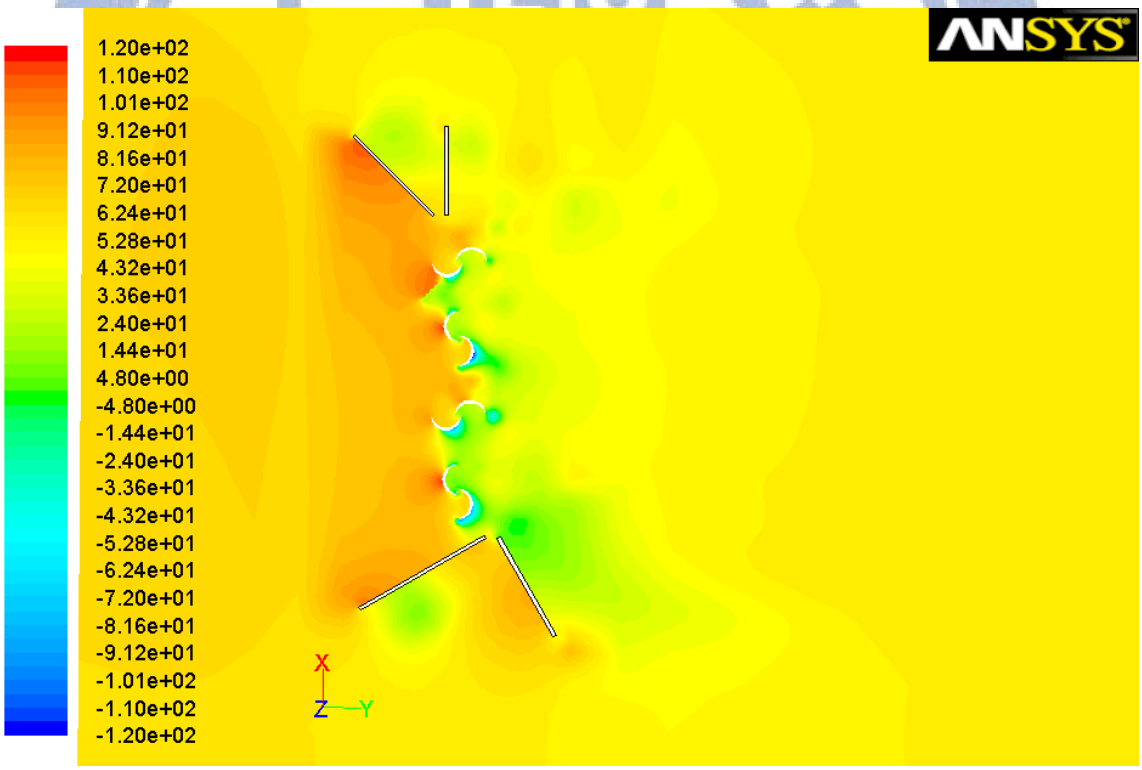

Fig. 5.13 Static pressure field around system with curtain

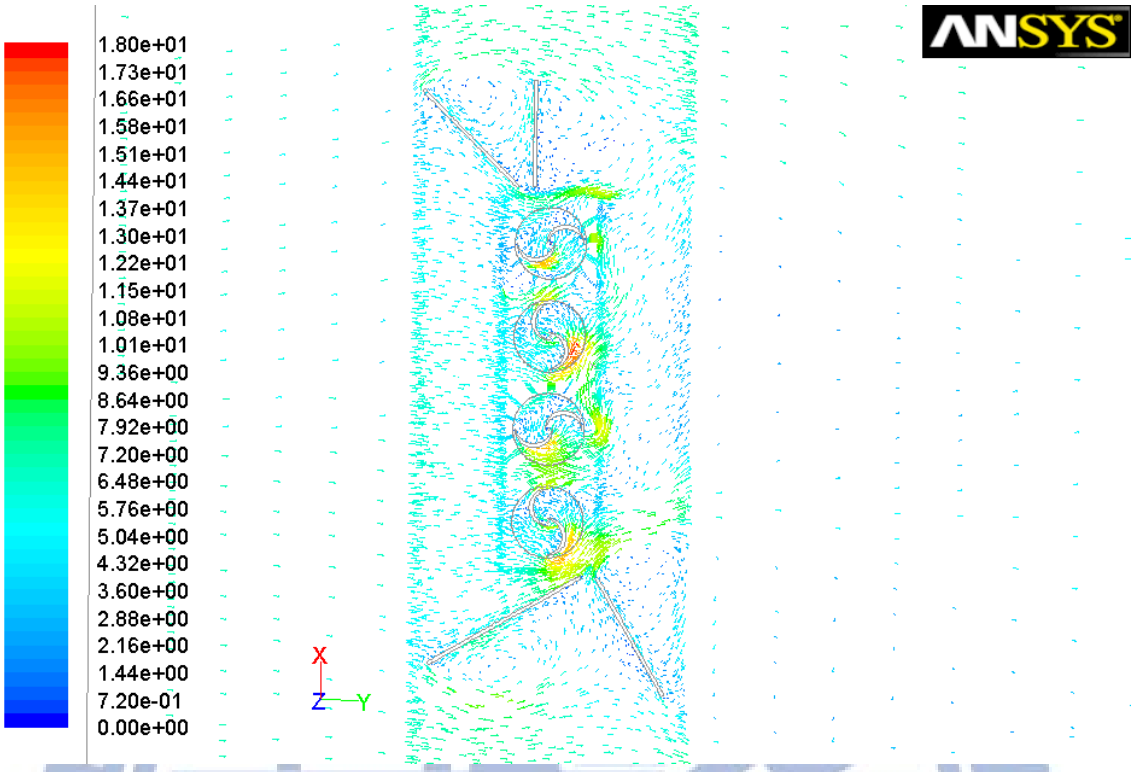

Fig. 5.14 Velocity vector distribution around system with curtain

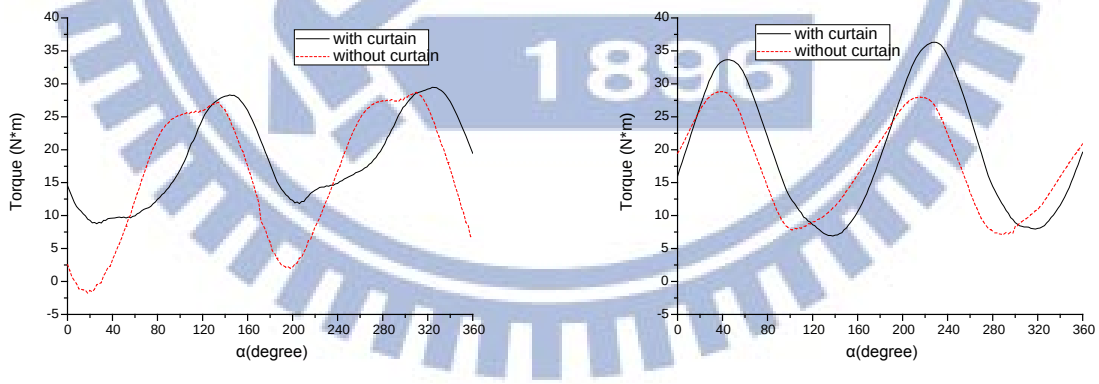

(a) **(b)**

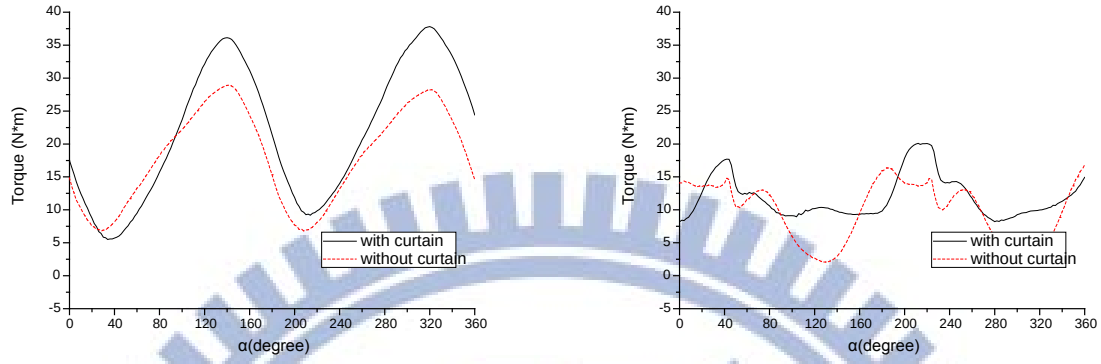

(c) **(d)**

Fig. 5.15 Comparison of torque curves between system with curtain and without curtain at TSR 0.6:
(a) Rotor No.1; (b) Rotor No.2; (c) Rotor No.3; (d) Rotor No.4

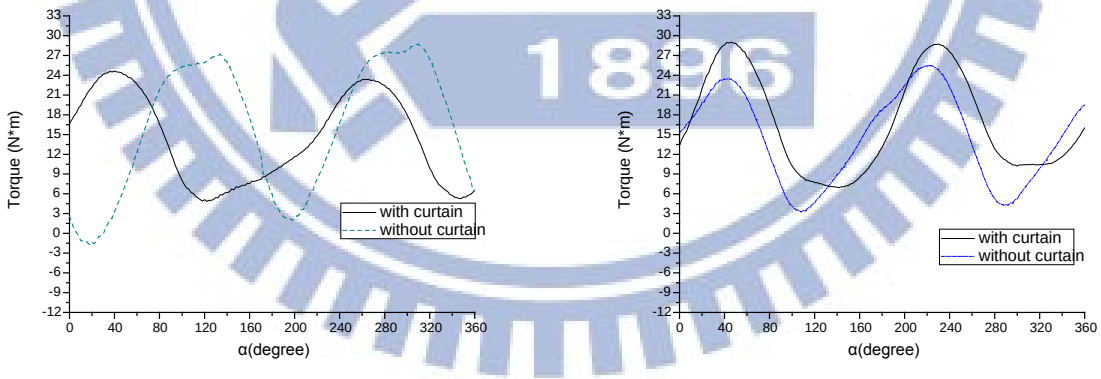

(a) **(b)**

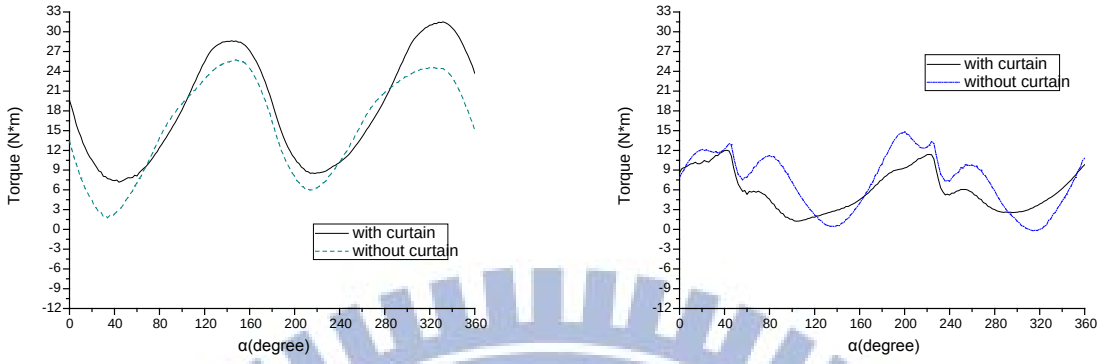

(c) **(d)**

Fig. 5.16 Comparison of torque curves between system with curtain and without curtain at TSR 0.8:
(a) Rotor No.1; (b) Rotor No.2; (c) Rotor No.3; (d) Rotor No.4

Fig. 5.17 Photo of parallel matrix system

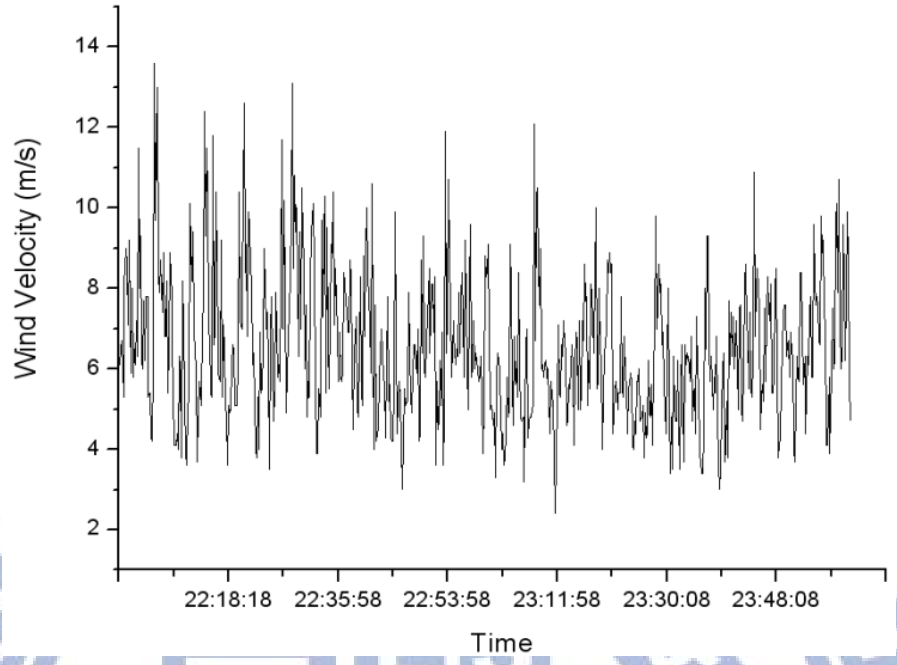

(a)

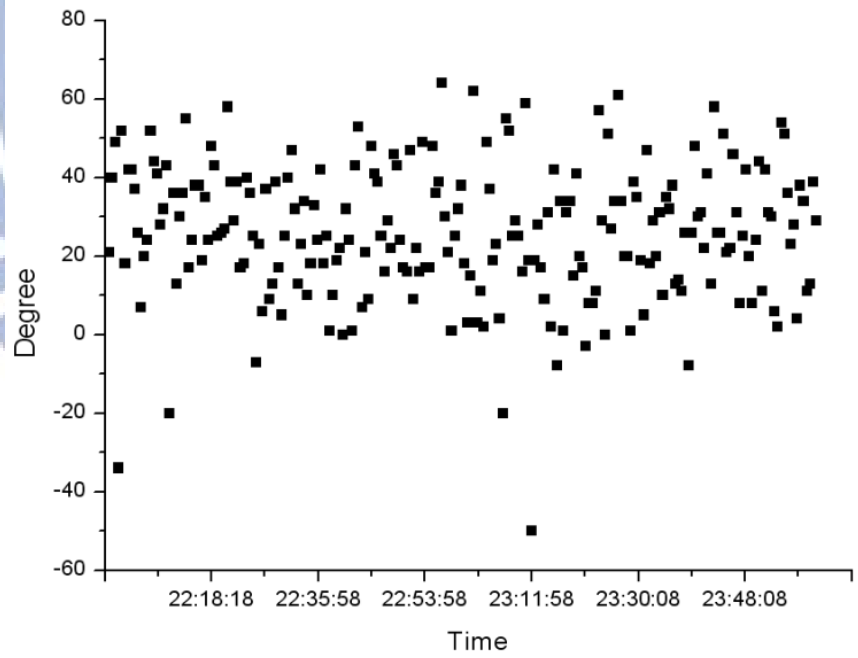

(b)

Fig. 5.18 Variation of wind: (a) wind velocity; (b) wind direction

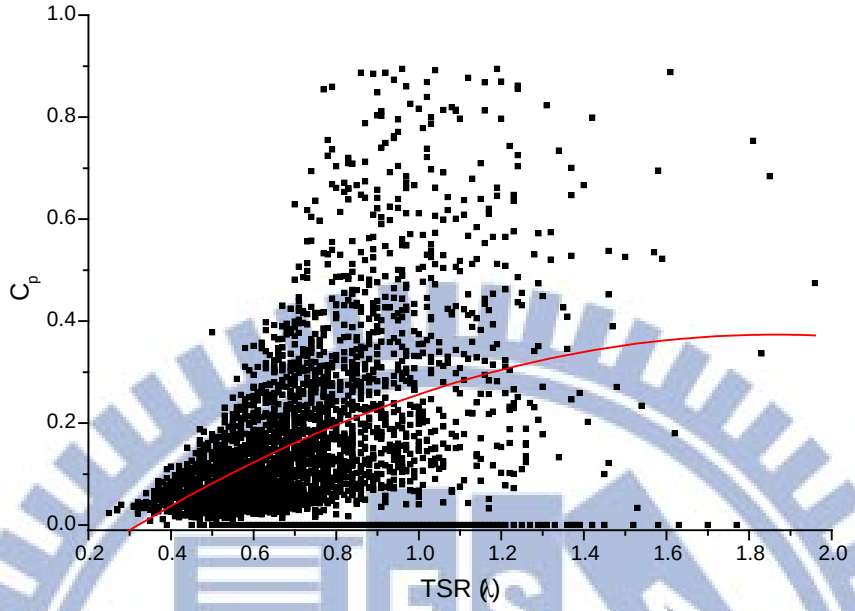

Fig. 5.19 $C_p(\lambda)$ with curtain (with battery)

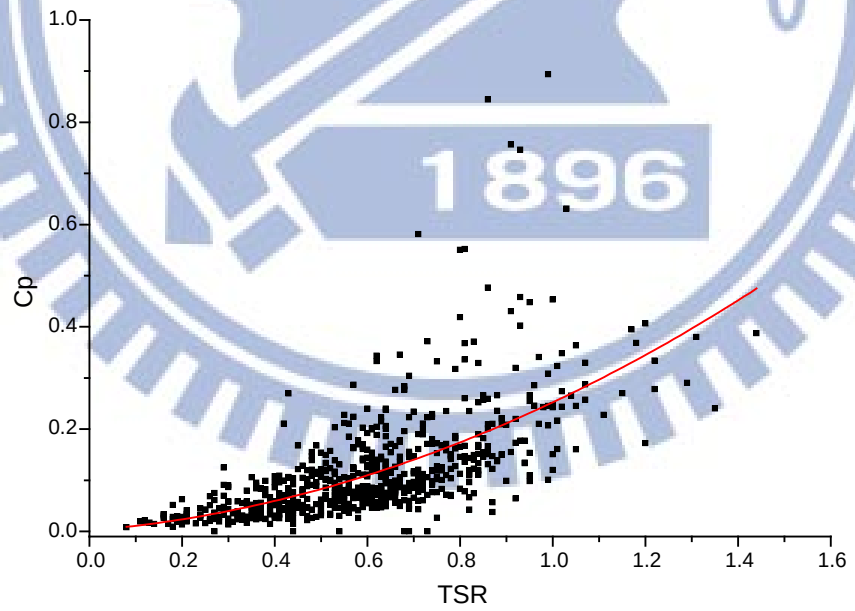

Fig. 5.20 $C_p(\lambda)$ without curtain (with battery)

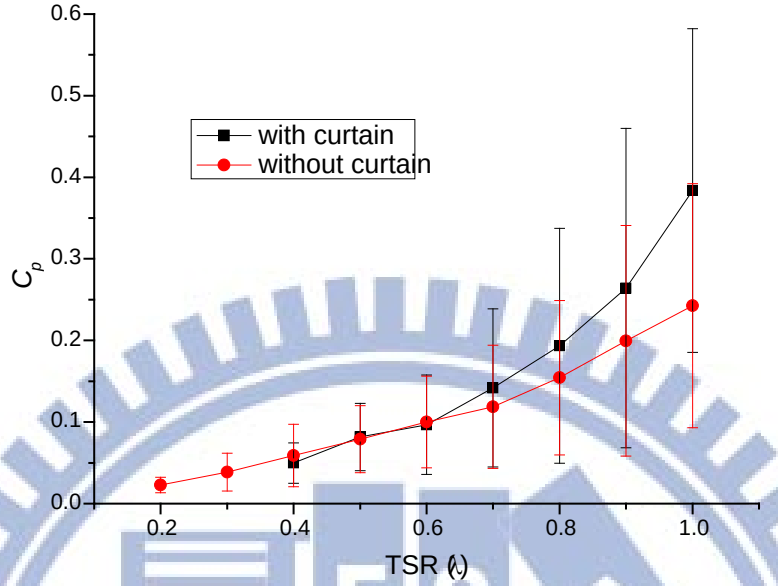

Fig. 5.21 $C_p(\lambda)$ with and without curtain (with battery)

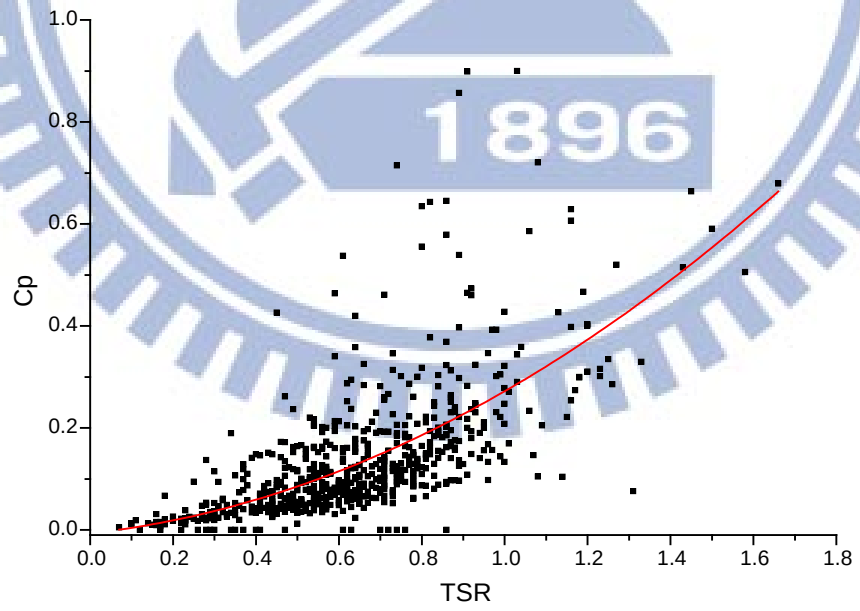

Fig. 5.22 $C_p(\lambda)$ with curtain (without battery)

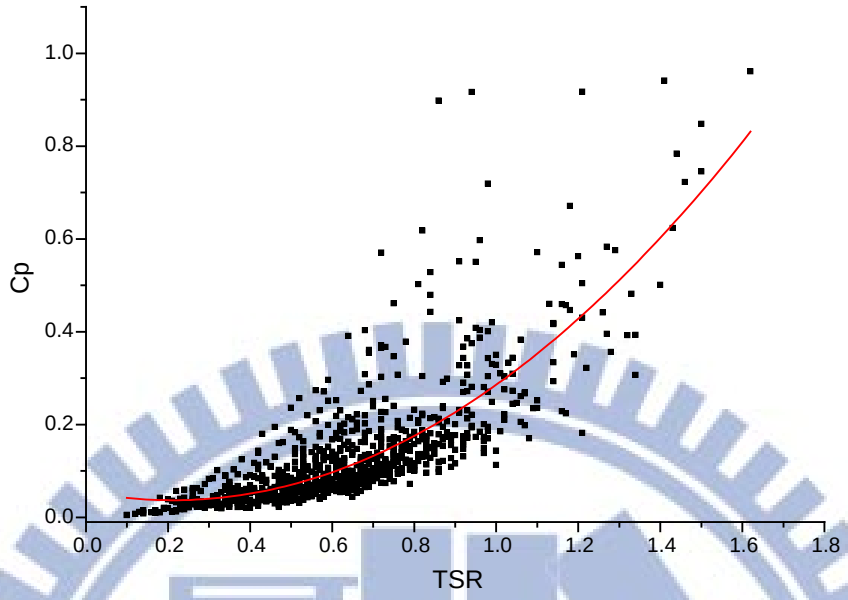

Fig. 5.23 $C_p(\lambda)$ without curtain (without battery)

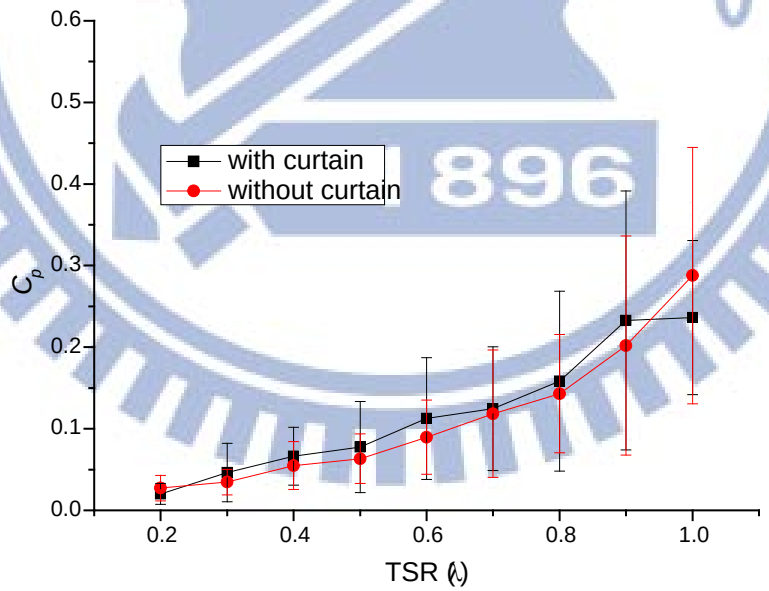

Fig. 5.24 $C_p(\lambda)$ with and without curtain (without battery)

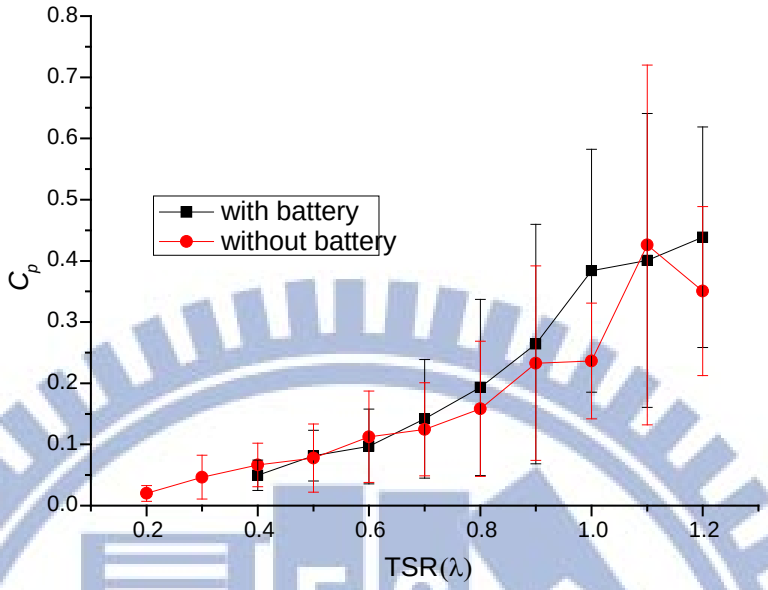

Fig. 5.25 $C_p(\lambda)$ with and without battery (with curtain)

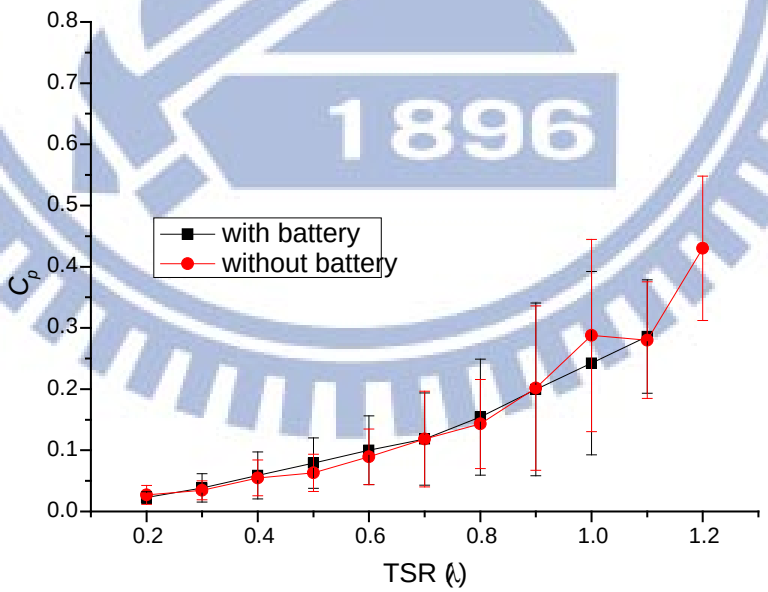

Fig. 5.26 $C_p(\lambda)$ with and without battery (without curtain)

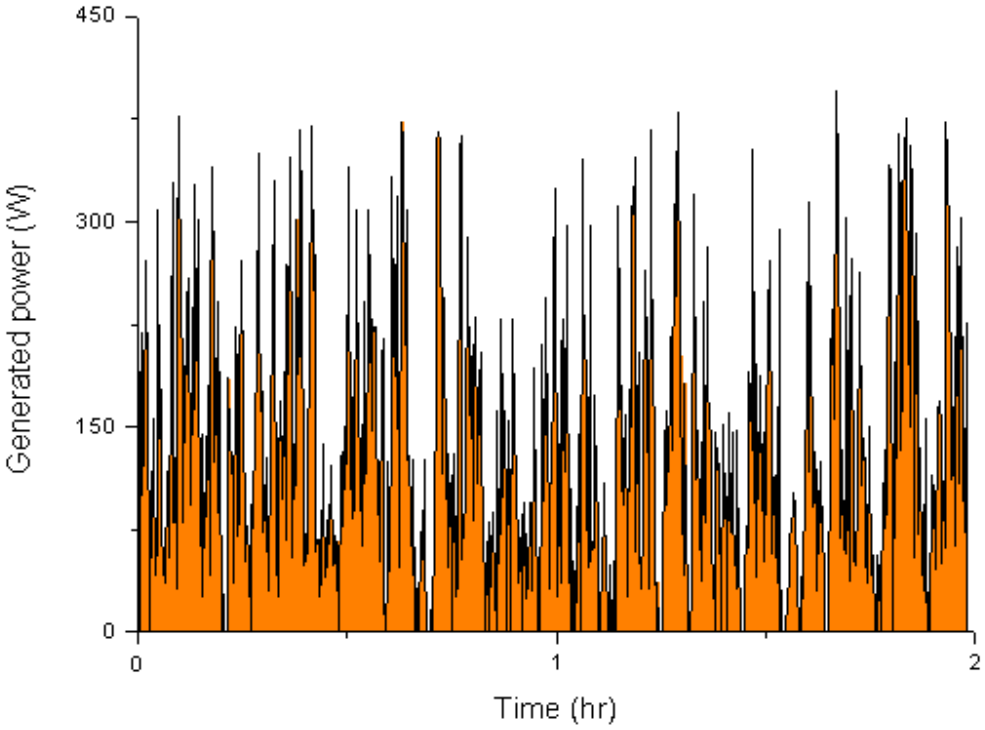

Fig. 5.27 Power generating in two hours

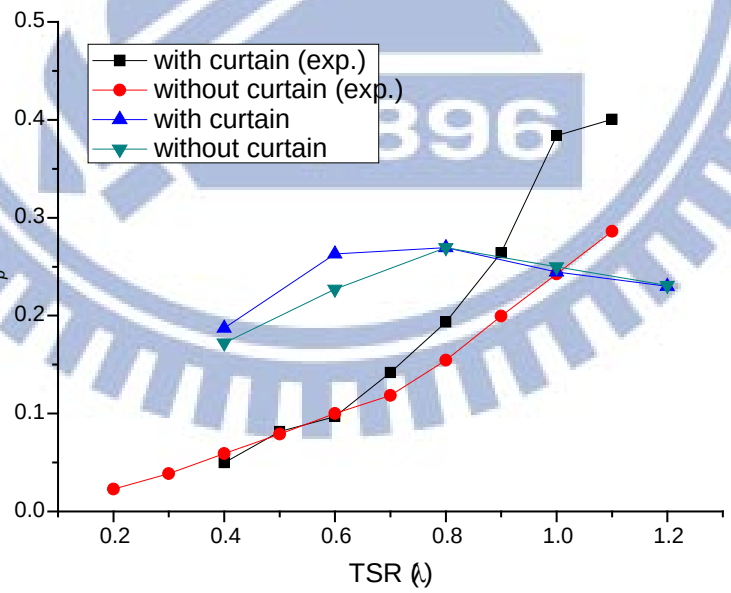

Fig. 5.28 Comparison between experiment and simulation

CHAPTER 6

CONCLUSIONS AND RECOMMENDATIONS

6.1 Conclusions

The conclusion in this study can divide into three parts. Firstly, the numerical investigations on performance of Savonius wind rotor and parallel matrix system. The simulation results show that C_p of parallel matrix system is higher than one single Savonius wind rotor. The maximum C_p value of simulation results for one single rotor is 0.181, for parallel matrix system without curtain is 0.262 and for system with curtain is 0.270. All of these maximum values are occurred at TSR 0.8. Otherwise, the curtain especially enhanced the performance of system at low TSR. The maximal improving of system by curtaining is happened at TSR 0.6 which progress 16% performance.

Secondly, a series of experiment are brought up. On account of the system which is built on an open field, wind velocity, wind direction and rotational speed of wind rotors have significant variation. Same as the simulation results, curtaining enhance the performance of system. System progresses 25% performance by curtaining. Even if system without battery, it still has 14% performance improving. Withdrawing battery from second side of battery is no use for improving performance but cause oscillation especially in high TSR.

Finally, the different between simulation and experiment are energy transform efficiency and investigative operation ways. For the expression of performance (C_p) between simulation and experiment is diverse, simulation results are higher than experiment results. The experiment results calculate C_p by generated power which needs to consider energy transform efficiency. However, the main reason of different in high TSR is due to the phenomenon in

simulation will not happen in reality. The rotational speed of wind rotor is fixed in simulation, but it needs wind to distribute energy in reality.

6.2 Recommendations

In the end of this study, some recommendations are given to progress this research which are listed as followed:

1. In simulation, rotational speed of wind rotors should be driven by wind passing.
2. Inlet velocity could consider giving a fluctuating sin function to simulate wind oscillation.
3. Other ways to improve performance of this system could consider experimental mechanism and electric circuit upgrade.
4. The parallel matrix system could be connected to local grid or family electric supply that we can get some benefit from wind energy.

REFERENCE

[1] Ottmar Edenhofer, et al., Special Report on Renewable Energy Sources and Climate Change Mitigation, IPCC, Abu Dhabi, May 2011.

[2] Hiroki Hondo, “Life Cycle GHG Emission Analysis of Power Generation Systems: Japanese Case”, Energy, 30, pp. 2042-2056, 2005.

[3] Jia-Shiuan Feng, “A Numerical Analysis of Power Efficiency of Wind Rotor System in Parallel Matrix”, National Chiao Tung University, Degree of Master of Science in Mechanical Engineering, June 2011.

[4] 關 和市 (Kazuichi Seki)，牛山 泉 (Izumi Ushiyama)著，垂直軸風車 (Suichokujiku Fusha)，蔡宜澂，林冠緯，林潔，曾雅秀編譯，初版，台北市，臺大出版中心，民國一百年。

[5] S. J. Savonius, “The S-Rotor and its Applications”, Mechanical Engineering, 8, No.5, pp. 333-338, 1931.

[6] Ben F. Blackwell, Robert E. Sheldahl, and Louis V. Feltz, “Wind Tunnel Performance Data for Two- and Three-bucket Savonius Rotors”, Journal of Energy, 2, pp. 160-164, 1978.

[7] Nobuyuki Fujisawa, “On the Torque Mechanism of Savonius Rotors”, Journal of Wind Engineering and Industrial Aerodynamics, 40, pp. 277-292, 1992.

[8] Kunio Irabu and Jitendro Nath Roy, “Characteristics of Wind Power on Savonius Rotor Using a Guide-box Tunnel”, Experimental Thermal and Fluid Science, 32, pp. 580-586, 2007.

[9] Burçin Deda Altan, Mehmet Atılgan, and Aydoğan Özdamar, “An Experimental Study on Improvement of a Savonius Rotor Performance with

Curtaining”, Experimental Thermal and Fluid Science, 32, pp. 1673-1678, 2008.

[10] Akinari Shigetomi, Yuichi Murai, Yuji Tasaka, and Yasushi Takeda, “Interactive flow field around two Savonius turbines”, Renewable Energy, 36, pp. 536-545, 2011.

[11] Zhenzhou Zhao, Yuan Zheng, Xiaoyun Xu, Wenming Liu, and Guoxiang Hu, “Research on the Improvement of the Performance of Savonius Rotor Based on Numerical Study”, Sustainable Power Generation and Supply, pp. 1-6, 2009.

[12] Sylvain Antheaume, Thierry Maître, and Jean-Luc Achard, “Hydraulic Darrieus turbines efficiency for free fluid flow conditions versus power farms conditions” Renewable Energy, 33, pp. 2186-2198, 2008.

[13] K. Pope, V. Rodrigues, R. Doyle, A. Tsopelas, R. Gravelsins, G.F. Naterer, and E. Tsang, “Effects of stator vanes on power coefficients of a zephyr vertical axis wind turbine”, Renewable Energy, 35, pp. 1043-1051, 2010.

[14] Robert Howell, Ning Qin, and Jonathan Edwards, Naveed Durrani, “Wind tunnel and numerical study of a small vertical axis wind turbine”, Renewable Energy, 35, pp. 412-422, 2010.

[15] Hu Yong-Hai and Tong Zheng-Ming, "The Influence of Windshield on Aerodynamic Performance of VAWT," 2009 International Conference on Energy and Environment Technology, iceet, 1, pp. 893-896, 2009.

[16] Manfred Stiebler, Wind Energy Systems for Electric Power Generation, Springer-Verlag, Berlin Heidelberg, 2008.

[17] Boden, T., and G. Marland, Oak Ridge National Laboratory, Carbon Dioxide Information Analysis Center, 2010.

[18] How do the wind turbines work. 2009. BiofuelsWatch.com. 2 Oct. 2011

http://www.biofuelswatch.com/how-do-wind-turbines-work/.

[19] Wake. Danish Wind Industry Association. 2 Oct. 2011 http://wiki.windpower.org/index.php?title=Wake&redirect=no.

[20] Erich Hau, Wind Turbines: Fundamentals, Technologies, Application, Economics, Springer-Verlag, Berlin Heidelberg, 2006.

[21] João Vicente Akwa, Gilmar Alves da Silva Júnior and Adriane Prisco Petry, "Discussion on the verification of the overlap ratio influence on performance coefficients of a Savonius wind rotor using computational fluid dynamics", Renewable Energy, 38, pp. 141-149, 2012.

[22] Cross-diverter. Huang Yih Gear Industry Co., Ltd.. 25 Oct. 2011, http://www.gearbox.com.tw/hy-c2.htm/.

[23] SD-P21(S). Shihlin Electric Co.. 25 Oct. 2011, http://www.seec.com.tw/index.asp/.

[24] Uffe Hindhede, John R. Zimmerman, R. Bruce Hopkins, Ralph J. Erisman, Wendell C. Hull and John D. Lang, Machine Design Fundamentals, A Practical Approach, John Wiley & Sons, CA USA, 1983.

[25] E. Spooner and A. C. Williamson, "Direct coupled, permanent magnet generators for wind turbine applications", Electric Power Application, IEE Proceedings, 143, No.1, pp. 1-8, 1996.